Nanostructured metals for enhanced light-matter interaction with nanoscale materials: design, sensing and single photon emitters

by

Zohreh Sharifi
B.Sc., Shiraz University, 2011
M.Sc., Tarbiat Modares University, 2016

A Dissertation Submitted in Partial Fulfillment of the
Requirements for the Degree of

DOCTOR OF PHILOSOPHY

in the Department of Electrical and Computer Engineering

Nanostructured metals for enhanced light-matter interaction with nanoscale materials: design, sensing and single photon emitters

by

Zohreh Sharifi
B.Sc., Shiraz University, 2011
M.Sc., Tarbiat Modares University, 2016

Supervisory Committee

Dr. Reuven Gordon, Supervisor
(Department of Electrical and Computer Engineering)

Dr. Jens Bornemann, Departmental Member
(Department of Electrical and Computer Engineering)

Dr. Irina Paci, Outside Member
(Department of Chemistry)

ABSTRACT

Plasmonics have been used to enhance the interaction of light with metallic nanostructures and lanthanide-doped upconversion nanocrystals. This enhancement can be achieved by using specific structures, materials, and plasmonic resonators at the emission and absorption wavelengths of the particles. This dissertation is based on four projects, which are mainly about the interaction of light and matter in metallic nanostructures and the up-conversion of nanocrystals using plasmonic resonators.

In metal-insulator-metal systems, the cavity's resonant length is determined by the plasmon wavevector and the phase of reflection from the end faces. In general, the resonance length is not a simple multiple of the half-wavelength due to the significant reflection phase. As a result, in order to have a better understanding of MIM cavity resonances, the reflection phase must be calculated correctly. In the first project, the reflection phase obtained by SPPs upon reflection off the slit end-faces is calculated analytically using a simple mode matching model for real metals showing both dispersion and loss. The technique is similar to previous works, with the exception that we use the unconjugated version of the orthogonality relation. The results show good agreement with the experimental data. By having a strong grasp of the SPP dispersion, this technique aids in the design of plasmonic devices for operation at a specific wavelength.

Single-photon sources are optical sources capable of emitting a single photon. A single lanthanide ion within a plasmonic nano structure with a large emission enhancement is one technique to generate a single-photon source at 1550 nm, which is a low-loss band used in fibre optics. In the second project, plasmonic double nanohole resonators are fabricated using colloidal lithography. These structures have been used to enhance the emission from low-concentration erbium emitters. The results indicate that different levels of emissions exist based on the amount of Er contained inside the nanocrystals. These findings would be an excellent starting point for developing a single-photon source operating at a 1550 nm wavelength employing erbium. Because not only can it increase the emission rate from erbium emitters, but it also helps to find and isolate a single emitter, which gives a stable single photon source.

Because the surface plasmon resonance is exponentially coupled to the surface, it exhibits excellent sensitivity to changes in the refractive index near the surface. This is the underlying principle of commercially available surface plasmon resonance biosensors. Due to the wide range of applications in water quality testing and biosensing, it

is critical to develop highly sensitive sensors that are compatible with commercial sensors. In the third project, we develop a design for SRSP sensing using a rectangular stripe grating and a 10 nm thick gold film. The 10 nm gold layer is sufficiently thick to enable continuous films to be formed using standard deposition procedures. We demonstrate that by employing rigorous coupled wave analysis, the surface sensitivity of these films to an adlayer is increased by 3.3 times in angle units and the resolution is increased by fourfold while working at the commercial SPR system wavelength of 760 nm.

Before trapping a particle in double nanohole apertures, we must first locate the double nanohole on the sample (gold on glass with apertures) and compare the scanning electron microscopy images with the image on the camera in the optical setup using certain markers. In the fourth project, to make DNH aperture trapping easier, we provide a polarization and transmission dependency approach for localizing and orienting DNHs on a substrate. This method provides a time and cost effective way to ease the experimental process. This technique may also be used to localize different aperture clusters and single holes.

Contents

List of Figures

Glossary

APD	avalanche photodiode
ATR	attenuated total reflection
CCD	charge-coupled device
CW	continuous wave
DM	dichroic mirror
DNH	double nano hole
EM	electromagnetic
FDTD	Finite-difference time-domain
FIB	focused ion beam
HWP	half-wave plate
IR	infrared
LP	linear polarizer
LSP	localized surface plasmon
NA	numerical aperture
LPF	long pass filter
PBC	periodic boundary condition
PEC	perfect electric conductor
PMC	perfect magnetic conductor
PML	perfectly matched layer
SEM	scanning electron microscope
SERS	surface enhanced raman scattering
SIBA	Self-induced back action
SNH	single nano hole
SPF	short pass filter
SPP	surface plasmon polariton
RCWA	rigorous coupled wave analysis

SRSP	short range surface plasmon
LRSP	long range surface plasmon
TE	transverse electric field
TFSF	total-field scattered-field
TM	transverse magnetic field
UCNC	upconversion nanocrystal

ACKNOWLEDGEMENTS

First and foremost, I am extremely grateful to **my supervisor, Professor Reuven Gordon** for his invaluable advice, continuous support, and patience during my PhD study. His immense knowledge and plentiful experience have encouraged me throughout my academic research. I would also like to thank **Professor Jens Bornemann**, **Professor Irina Paci**, and **Professor Chitra Rangan**for their help in shaping my dissertation path.

I gratefully acknowledge the critical contributions by my collaborators throughout my study: **Professor C. J. M. van Veggel, Adriaan L. Frencken, Ghazal Hajisalem, and Michael Dobinson**.

My gratitude extends to **the CAMTEC faculty and staff** for their support and the members of the Nanoplasmonics Research Lab specially **Dr. Amirhossein Alizadeh Khaledi, Adarsh Lalitha Ravindranath, Dr. Ryan Peck and Dr. Ali Khademi**.

Finally, and most importantly, I would like to thank **my family** for their unconditional love, support, and encouragement to continue my studies.

DEDICATION

To my supportive parents,

My empathetic sisters,

My friendly brother,

and my beloved husband

Chapter 1

Introduction

In this dissertation, nanostructured metals have been used to enhance light-matter interaction. The enhanced interaction is then used to design sensors and single photon emitters. This chapter discusses the motivations for the works presented, why researchers are interested in plasmonics, and why UCNCs are useful. The organization of this dissertation is detailed here in section 1.2. This dissertation can be divided into four projects. The contributions of all the authors are listed in the last section of this chapter.

1.1 Motivation

In physics, an oscillating charge generates electromagnetic waves. When these charges are accelerated, they emit electromagnetic waves with the same frequency as the oscillation. Radio waves, microwaves, infrared, visible light, ultraviolet, X-rays, and gamma rays are all types of electromagnetic waves. Each regime of this spectrum has a variety of applications, including biomedical devices, military weaponry, energy conversion, communications, detection, and sensing. More attention has been focused on the visible light (400 to 750 nm) and the near-infrared range (750 nm to 2.5 μm) than the other ranges. Because the sun, the earth's primary source of energy, has the highest spectrum of power in the visible range, the way each cell on the planet interacts with this light is noteworthy. The near-infrared is also a particularly appealing wavelength, because of its numerous applications in modern technologies, especially telecommunication systems. As a result, in order to create a wide range of devices, including cameras, light sources, detectors, and sensors, we need to have a firm grasp

of how light and matter interact at these wavelengths.

Scientists are interested in how nobel metals like gold and silver work with light at the interface with a dielectric to make plasmonic phenomenon. In fact, light interacts with the conducting electrons of a metal with a negative permittivity at its interface with a dielectric with a positive permittivity. The metal's free electrons couple to incident electromagnetic fields and propagate as surface plasmon polaritons. These waves are evanescently confined in the normal direction of the interface. Furthermore, the coupling of the incident electromagnetic fields to the conductive electrons of a subwavelength metallic nanostructure results in localized surface plasmons, which are the non propagating type of plasmon waves. As a result, light can be confined to the order of the light wavelength or smaller using a metal-dielectric structure. The materials' permittivities, geometry, and plasmonic oscillation wavelengths all play a role in confinement. That means particles and structures of various sizes and shapes will exhibit different plasmonic resonances. Developments in the design, fabrication processes, and analysis methods help researchers to design and fabricate nonstructured metals to obtain desired plasmonic wavelengths for different applications.

In this dissertation, we first propose a modified method to analyze a metal-insulator-metal (MIM) structure and investigate the impact of metal loss on the plasmonic resonances. We show that the correct calculation of the reflection phase, which is a key factor in the calculation of the plasmon wavelength, is important.

Secondly, to take advantage of one of the most attractive applications of light-matter interaction, an optical tweezer is used to trap and manipulate erbium-doped nanoparticles. Plasmonics is very helpful here to confine the electromagnetic (EM) waves in a plasmonic double nano hole (DNH) aperture and increase the optical trapping probability. This happens by creating an enhanced field at the cusp separation of the DNH and pulling the particle toward the enhanced field. Lanthanides, which are non-blinking stable emitters, can upconvert the NIR wavelengths to visible light and also emit at NIR wavelengths. They outperform other upconversion mechanisms such as harmonic generation, but their efficiency is still insufficient for practical applications. Here, to improve the upconversion efficiency, plasmonic nanostructures were used to boost the interaction of light with lanthanide electrons. One of its main applications is in designing single photon sources. We are able to create single-photon sources by isolating a single emitter capable of emitting a single stable photon.

Another application of surface plasmons is in designing surface plasmon resonance sensors. In one of the designs, a prism is used to couple the light into surface plas-

mon waves. Thanks to the high index of the prism, the wave vector of the prism matches the wave vector of the surface plasmon. Because of the metal loss, light is absorbed in the coupling condition, and this leads to a dip in the reflection [2]. Due to their surface-bound nature, surface plasmon polaritons are extremely sensitive to changes in refractive index at the surface. This is the idea behind the commercialized surface plasmon resonance (SPR) biosensors. Insulator-metal-insulator (IMI) structures, in particular, allow for short-range surface plasmon (SRSP) modes that are more strongly confined to the surface by decreasing the thickness of the metal. This increases surface sensitivity even further. Here, we present a SRSP sensing design based on a rectangular gold stripe grating on a glass prism with a 10 nm thickness. The gold's top layer is water. To simplify the fabrication process, a thick 10 nm gold layer is utilized. This enables the use of continuous films using conventional deposition techniques. According to rigorous coupled-wave analysis (RCWA), this structure is 3.3 times more sensitive to an adlayer in angle units. Additionally, the resolution is quadrupled while working within the same range as commercial SPR systems. As a result, we think that these chips will soon be employed for more sensitive SPR sensing.

Finally, in our last work, we established a much more approachable method for determining the position and orientation of DNHs that does not require SEM or other complex techniques.

In this dissertation, the goal is to investigate the interaction of light and matter in nanoplasmonic structures and take the advantage of the field enhancement for the abovementioned applications.

1.2 Organization of the Dissertation

The dissertation is based on four manuscripts that have been published in peer-reviewed journals. The contributions of all the authors are listed below. In chapter 2, the theory of plasmonics, nanostructures, UCNCs, optical tweezers, and all the theory behind our work are presented. In chapter 3, a summary of each manuscript is given. The complete manuscripts are added to the appendix section (A-D). Chapter 4 includes a summary, conclusion, and possible future works.

1.3 Major Contributions

1.3.1 Large Plasmonic Resonance Shifts from Metal Loss in Slits

Z.S. performed the mathematical and numerical calculations, and also the FDTD simulations. R.G. conceived the method. All authors assisted in writing the manuscript.

1.3.2 Isolating and Enhancing Single-Photon Emitters for 1550 nm Quantum Light Sources Using Double Nanohole Optical Tweezers

Z.S., M.D., and G.H. performed the trapping experiments. Z.S. analyzed the data. A.L.F. and F.C.J.M.v.V. were responsible for nanocrystal synthesis and characterization. M.S.S. performed the FDTD simulations. R.G. conceived the experiment. All authors assisted in writing the manuscript.

1.4 Minor Contributions

1.4.1 Improving Sensitivity of Existing Surface Plasmon Resonance Systems with Grating-Coupled Short-Range Surface Plasmons

E. B, and Z.S. performed the mathematical and numerical calculations, and also the FDTD simulations. R.G. conceived the method. All authors assisted in writing the manuscript.

1.4.2 Accessible High-Performance Double Nanohole Tweezers

G.H. , E.B., and M.D. performed the trapping experiments, fabricated the samples, and analyzed the data. Z.S. performed the FDTD simulations, fabricated the samples, and conceived the idea. M. D. fabricated the samples. R.G. supervised the project, providing ideas and facilities. All the authors assisted in writing the manuscript.

Chapter 2

Methods and Review

The primary focus of this dissertation is to analyze plasmonic nanostructures and develop novel designs for various applications. To do so, a grasp of several fields of science is essential. In this chapter, we first give an introduction to plasmonic phenomena, localized surface plasmons, long range surface plasmons, and short-range surface plasmons. Following that, we discuss several techniques for analyzing the structures that support surface plasmons. This chapter also discusses lanthanide-doped nanocrystals and their upconversion mechanism. optical tweezers are explored as a technique for trapping and manipulating sub-wavelength particles. Plasmonic nanoapertures as a good candidate to enhance light-matter interactions at metal-dielectric interfaces have been studied. Finally, The colloidal lithography method to prepare the samples for the proposed experiment is described.

2.1 Plasmonics

Light may couple with electrons in noble metals to generate a wave that is bound to the metal's surface. The surface plasmon is the name given to this wave. When the structure's dimensions are much smaller than the excitation wavelength, visible light can be concentrated to the nano-meter scale. This phenomenon is caused by the interaction of light and matter and occurs at dielectric-metal interfaces. The local electric field is enhanced when light is confined to a nanoscale size. This has a wide range of applications, ranging from solar energy conversion to sensing and detecting techniques, as well as optical trapping [15, 16]. A plasmonic structure with resonant frequencies at desired wavelengths can enhance the local electric field

intensity which results in the enhancement of the absorption and emission processes. Raman scattering is one of the main applications of surface plasmons. In plasmonic Raman scattering, a photon at a specific wavelength is absorbed by a target molecule and makes the molecule emit a photon at another wavelength, which is usually close to the excitation wavelength. The difference in the wavelength of the incident and re-emitted photon is the parameter that can be used to detect that molecule. It has been shown that the strength of the local electric field affects both photon absorption and emission [17]. As a result, using plasmonic structures can help to improve molecule sensitivity in Raman scattering systems [18, 19]. In general, not all multi-photon processes have an emission wavelength close to the excitation wavelength. Therefore, designing plasmonic structures that can support a wide range of plasmonic frequencies is required [20].

2.1.1 Surface Plasmon Polaritons (SPPs)

In the previous section, we mentioned that plasmonic phenomena happen at the interface of dielectric and metal. Let's consider the structure in Figure 2.1 to understand the behaviour of the electromagnetic wave in such structures.

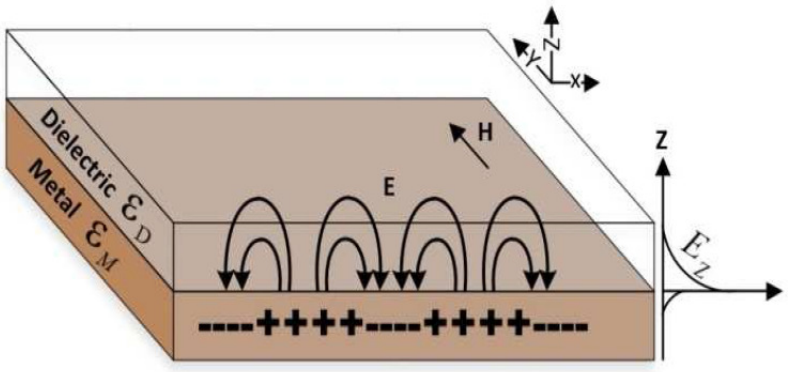

Figure 2.1: Surface plasmon polaritons propagation. Reprinted with permission from [1].

To get the electric and magnetic fields inside the structure, we need to solve Eq. 2.1 which is known as the Helmholtz equation,

$$\nabla^2 E + k_0^2 \epsilon E = 0 \tag{2.1}$$

where $k_0 = 2\pi/\lambda$ is the wave vector in vacuum. Applying boundary conditions and solving the equations for these conditions shows wave propagation at the interface (X axis) for TM (transverse magnetic) mode and no propagation for TE (transverse electric) mode. The solution for the TM mode shows a propagation wave at the interface (X axis) and an evanescent decay electric field in the propagation direction (Z axis).

By substituting the dielectric constant relation in Maxwell's equation, the dispersion relation of light in a metal is obtained and is given as

$$\omega^2 = (Kc)^2 + \omega_P^2 \tag{2.2}$$

where K denotes the wave vector in the dielectric region. c is the speed of light, ω is the angular frequency of the incident electromagnetic field, and ω_P is plasma

frequency. The full set of equations is available elsewhere [2]. The wavevector K_x, or momentum of SPPs, is a function of angular frequency and metal and dielectric permitivities [1, 21]

$$K_x = K_0 \sqrt{\frac{\varepsilon_I \varepsilon_M}{(\varepsilon_I + \varepsilon_M)}} \tag{2.3}$$

ε_I and ε_M are the frequency dependent complex dielectric functions (relative permittivity) of the dielectric and metal medium, respectively. It is clear if ε_M is real and negative and approaches $-\varepsilon_I$, the wavelength gets extremely short because the propagation constant becomes too large. That leads to confinement of light to the surface (X axis) and the creation of a decaying electric field in the propagation direction (Z axis). This excitation is called surface plasmon polaritons, where the electric fields are confined and propagate along with the interface of two materials with negative and positive relative permittivities.

Figure 2.1 depicts SPPs propagating in a parallel direction to the metal-dielectric interface, as well as the electric field's exponentially decaying in the Z direction. The wavevector of the incident light depends on the permittivity of the medium in which it propagates ($\sqrt{\varepsilon_I} K_0$), and it is clearly less than that of SPPs. SPPs can be excited if the wave vector of the SPPs and the incident light are equal (this happens at a resonant frequency), or in other words, if the momentums of both sides are matched. The use of high index prisms, evanescent field coupling, and grating coupling have all been proposed as methods for momentum matching [22, 23, 24]. In one of our works that will be presented here, we employed prism and grating coupling to design a sensor that uses short-range surface plasmons [25].

2.1.2 Localized Surface Plasmon

There are two main types of surface plasmons: propagating surface plasmons (PSPs) and localized surface plasmons (LSPs), both of which are oscillations of free electrons at the metal-dielectric interface (LSPs) [26]. In the preceding section, we mentioned that SPPs are propagating types of surface plasmons that are generated by the coupling of the electromagnetic wave with the electron plasma of the metal at a metal-dielectric interface. Localized surface plasmons are non-propagating types of surface plasmons that happen due to the interaction of the incident electromagnetic wave with the conduction electrons of metallic nanostructures. When a conducting particle is excited by an oscillating electromagnetic field, it starts to oscillate locally around itself. This oscillation creates an enhanced localized plasmon wave which oscillates at a frequency known as localized surface plasmon resonance. This phenomenon leads to an enhanced field both inside and outside the particle. For SPPs, a phase matching technique needs to be used to excite the plasmon resonance of the structure. In contrast, the curved surface of a nanoparticle helps to excite the plasmon resonance by direct light illumination. The conventional system to analyze LSPs mathematically is shown in Figure 2.2. A spherical particle with radius a is located at a uniform static electric field. With a dielectric constant of ϵ_m, the background medium is non-absorbing and isotropic. The dielectric response of the particle is denoted by $\epsilon(\omega)$.

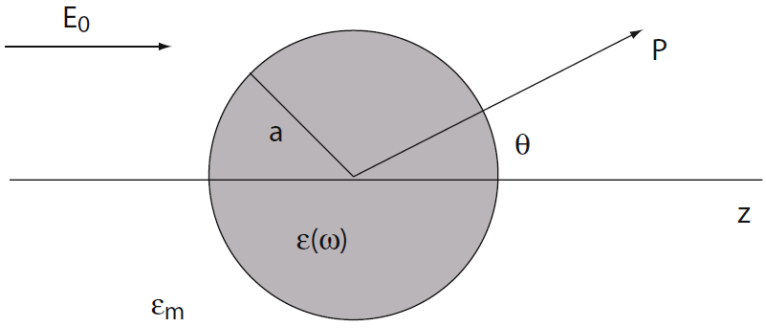

Figure 2.2: Sketch of a homogeneous sphere placed into an electrostatic field reprinted with permission from [2].

The particle is small enough so that $a << \lambda$. In this situation, The phase of the oscillating electromagnetic field does not change across the particle's volume. To find

the electromagnetic fields of this system, a quasi-static approximation of the Laplace equation ($\phi = 0$) solution is needed. By solving $E = -\nabla\phi$, the electric field inside and outside the particle can then be calculated as below [2]

$$\mathbf{E_{in}} = \frac{3\varepsilon_m}{\varepsilon + 2\varepsilon_m}\mathbf{E}_0 \tag{2.4}$$

$$\mathbf{E_{out}} = \mathbf{E}_0 + \frac{3\mathbf{n}(\mathbf{n}\cdot\mathbf{p}) - \mathbf{p}}{4\pi\varepsilon_0\varepsilon_m}\frac{1}{r^3} \tag{2.5}$$

$$\mathbf{p} = 4\pi\varepsilon_0\varepsilon_m a^3\frac{\varepsilon - \varepsilon_m}{\varepsilon + 2\varepsilon_m}\mathbf{E}_0 \tag{2.6}$$

where $\mathbf{p}$ is the electric dipole moment under the illumination of $\mathbf{E}_0$. It is apparent that the electric field becomes maximum when the denominator ,$|\varepsilon + 2\varepsilon_m|$, is minimum. Under this condition, the particle experiences a field enhancement. This enhancement of the electric field inside a nanoparticle is called a localized surface plasmon. In practice, this term cannot be zero because the real part of the metals in the visible and IR ranges is much greater than the dielectric permittivity used in plasmonic systems (such as water or hexane, which is used in this dissertation), but it still gives enough enhancement to excite the localized surface plasmon. The given circumstances demonstrate that the resonance frequency is strongly influenced by the background media and the particle permittivity. For the abovementioned reason, metal nanoparticles are good candidates for optical sensing when the refractive index inside the structure changes. They have also extensive application in surface-enhanced Raman scattering (SERS) [27], fluorescence enhancement [28], biomolecular interaction detection [29], and so on.

2.1.3 Surface Plasmons in Thin Films

The light confinement and consequently field enhancement generated by surface plasmon has opened new doors in designing new optical devices [30, 31, 32, 33]. Localized surface plasmons have been widely used in sensing applications [34, 35]. While SPPs have been mostly utilized for the manipulation of light in optical waveguides [36, 37]. Therefore, the surface plasmon applications can be categorized into two different types: waveguiding and sensing.

Metal nanostructures have been proven to concentrate electromagnetic energy into subwavelength structures at plasmon resonances. This energy concentration generates highly enhanced local and scattered fields in the designed structure. As it was seen in Eq. 2.4 and 2.5 in the previous section, the size and shape of the designed structure as well as the permittivity of metal and dielectric play an important role in the coupling and enhancement of the field. These degrees of freedom gave rise to a variety of different configurations and creative designs of metal nanostructures, including spheres, triangles, cubes, and nanoshells [38, 39, 40, 41]

A small change in the geometry of the structure or particles results in significant changes in the resonant behavior. Design and development of nanostructure-based technologies are similarly restricted because of the difficulty of assembling these particles. The two main types of proposed structures are nanorods and nanostrips. Most of the proposed designs in this field are based on these two geometries. Imurra et al. used single gold nanorods for near-field optical imaging using surface plasmons [42]. A variety of other applications of nanowires have also been proposed [43, 44, 45, 46].

Nanorods, which are finite-length thin metal wires, benefit from both field confinement and waveguiding. In nanowires, waves propagate throughout the length of the wire and are reflected at the end, causing a form of constructive interference to occur. The resonances arising from this phenomenon are called retardation-based resonances.

Small structures can support both retardation-based resonances and electrostatic resonances with specific designs [47]. The other type of the proposed structures using surface plasmon phenomena, nano strips, also takes advantage of retardation based resonances. Thin metal nano strips are in fact a two-dimensional type of nano wire. In such a structure, the coupling of the incident light can create highly confined fields inside the strip. The resonant wavelength, field enhancement, and resonant scattering can then be controlled by changing the size and shape of the nano strip, for instance,

by creating tapering and decreasing the thickness of the strip. The resonant behaviour and different designs of nano strips have been shown using numerical simulation and optical experiment [48, 49, 50]. Fabrication and assembling of nano strips is also simple. Different layers of strips can be put together or made on the same substrate. Nowadays, the challenges for researchers are to achieve the highest possible field enhancement with specific designs and to increase the bandwidth of the nano strip structures.

2.1.4 Characteristics of Short Range and Long Range SPP Modes

Surface plasmon polaritons at the long wavelength part of visible region and IR range have low speed similar to the free space electromagnetic wave and cannot be bound enough to the surface to create the expected enhanced field. The well-know solution to overcome this issue is to use multilayer structures with multiple metal-dielectric interfaces. Surface plasmon polariton super modes are produced as a result of the multilayer structures. The different designs of multilayer structures, which can be made by changing the size, shape, and permitivities of the metal and dielectric layers, lead to different super modes at desired wavelengths. They help in the creation of a highly enhanced field through the interaction of SPPs of individual interfaces [51].

The simplest multilayer structures are metal-insulator-metal (MIM) and insulator-metal-insulator (IMI) nanostructures. These nano strip structures, can support short range surface plasmon (SRSP) and long-range surface plasmon (LRSP). For symmetric IMI and MIM configurations, only two symmetric and antisymmetric modes exist. These two modes have even and odd electric field functions, respectively. If the configuration is not symmetric, the modes are no longer necessarily symmetric or anti-symmetric, but we can still continue to use the same nomenclature.

The symmetric mode of the electric field component, or even mode, is less confined to the surface. They have a larger SPP wavelength in the range of mm and so are called long range surface plasmons (LRSPs). LRSPs, in IMI structures, transform into the TEM mode of the adjacent dielectric as the thickness of the metallic layer decreases.

The antisymmetric mode of the electric field component, or odd mode, is more confined within the metal as the metal layer thickness decreases. They have a shorter SPP wavelength in the range of μm and a shorter decay length into the surrounding dielectric and so are called short-range surface plasmons (SRSPs). These modes have a higher effective mode index and, consequently, a larger propagation constant than the usual SPPs. SRSPs have large propagation losses as well as significant slow speeds. For this reason, they are also called slow-SPPs [3]. The propagation constant of the SRSP mode is strongly affected by the changes in the refractive index of the adjacent dielectric, which is the main reason that these modes are employed in surface plasmon resonance (SPR) sensors. SPR sensors are antisymmetric three-layer IMI structures whose fields are highly confined at the interface of metal and the top

insulator (analyte), which supports both SRSP and LRSP modes.

2.2 SPR Sensors

SPR sensors are one of the main applications of plasmonic multilayer structures. An IMI structure is employed to detect the changes in the refractive index of the top layer through excitation of the surface plasmon waves at the top metal-dielectric interface. The coupling of the incident light to the oscillations of metal free electrons occurs at resonance conditions using a prism. The wavelength and incident angle of the excitation light determine the energy and momentum, respectively. Because of the metal loss, the incident light couples to the surface plasmon under coupling conditions, resulting in a minimum in the reflection. The dielectric characteristics at the top metal-dielectric interface determine where the dip will be located on the reflection spectrum. For this reason, the changes in the reflection dip location may be tracked to diagnose the molecules at the top layer.

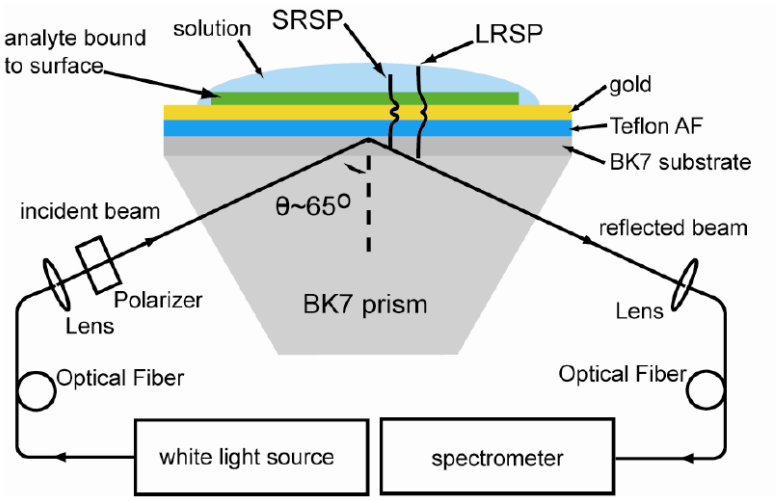

Figure 2.3: Schematic diagram of a self-referencing surface-plasmon resonance sensor. The sensor consists of a gold thin film on a buffer layer (Teflon-AF) that closely matches the refractive index of the solution of interest. The structure supports two surface plasmon modes excited at different wavelengths: a symmetric LRSP mode whose fields extend deeper into the solution and an anti-symmetric mode SRSP whose fields are concentrated near the surface of the metal. Reprinted with permission from [3].

Figure 2.3 depicts the well-known Kretschmann-Raether configuration of SPR

sensors [52]. This configuration is also known as the attenuated total reflection (ATR) configuration. For a metal-dielectric interface, direct incident light cannot create a phase matching condition because $\beta > k$, where β is the propagation constant of the surface plasmon and k is the wave vector in the dielectric side of the interface. Under certain circumstances, phase matching can be obtained using an asymmetric IMI structure. When an incident light excites the structure through a prism with a refractive index higher than the other dielectric, the wave vector in the metal will be $kn \sin\theta$ and this is enough to excite the surface plasmon at the metal-lower index dielectric. In fact, in this case the propagation constant of the existing surface plasmon is between the light line in the prism and the light line in the other dielectric. In this case, the calculated propagation constant for the prism-dielectric interface is less than the light line in the prism. That means there is no SPPs at the interface of the metal and prism[2].

The next important consideration in this configuration is the incident angle. An incident light with an angle greater than the critical angle must excite the structure to see the total reflection on the other side of the prism as shown in Figure 2.4(a).

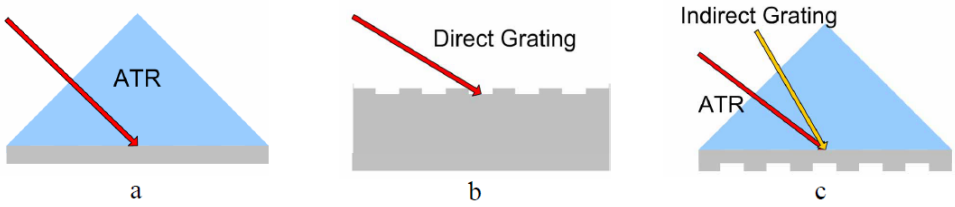

Figure 2.4: Three configurations to couple light to surface plasmons: a) Conventional ATR coupled SPR with a prism and a thin flat metal layer, b) Conventional grating coupled SPR where light is directly incident on the corrugated interface, c) Combined ATR and indirect grating coupled SPR. Due to the additional momentum from the grating, the indirect grating coupling requires a shallower incidence angle (yellow arrow). Reprinted with permission from[4].

Another method to excite surface plasmons in an IMI structure is using grating of grooves or holes as shown in Figure 2.4(b) [53, 54]. In this case the momentum matching can be achieved because of the increase in the wave vector of the incident light.

Figure 2.4 shows three configurations used for grating coupling: prism configuration, where the light is incident through a prism, direct grating configuration, where the light excites the grating array directly [55, 56], and the combined ATR and in-

direct grating coupled SPR [57]. Below formula shows how grating structures affect the coupling [58].

$$\begin{aligned} k_{\text{prism}} + K_G &= \beta \\ K_G &= \frac{2\pi}{\Lambda} \end{aligned} \tag{2.7}$$

with Λ being the grating period and β being the propagation constant of the surface plasmons.

The third configuration has attracted more attention due to the fact that it enables both grating-coupled and ATR-coupled surface plasmons. This configuration provides more coupling of the incident light to the surface plasmons. A grating has been used in some works to couple incident light to a surface plasmon [59, 60]. In other works, the light coupling to a surface plasmon has been done with the ATR method, and then a grating is used to perturb the surface plasmon [4, 21, 61, 62, 63]. The indirect configuration in subwavelength structures can also give rise to short-range surface plasmons and localized surface plasmons, which results in more enhancement of the field for a specific geometry. This can also increase the sensitivity of the sensor.

Sensitivity and resolution are two of the most important performance features of SPR sensors. The sensitivity of an SPR sensor is the ratio of the change in sensor output (which can be a change in the incident angle or wavelength where there is a dip for the reflection) to the change in the refractive index of the analyte (top dielectric) layer. When an SPR sensor is used, the resolution is defined as the smallest change in the refractive index of the analyte that causes a visible change in the location of the reflection dip. This characteristic of the SPR sensor is affected by noise that causes uncertainty in the results. The noise in the sensor comes from the fluctuations of the incident light, readout electronics, and shot noise [64].

2.3 Upconversion

In the context of energy transmission, upconversion refers to the process that is triggered by photon absorption. Upconversion results in a population in an excited state, where the energy of the population is greater than the energy of the pump photon. Because the excited state has higher energy than the optical pump, optical emission from it happens at a shorter wavelength than the optical pump. Conversion of NIR radiation to the visible has attracted research interest in upconversion [65]. Upconversion materials have numerous applications in bioimaging [66], solar absorption [67] spectrum increase and single-molecule microscopy [68]. An ideal medical imaging tool would be NIR light, which has a high penetration depth into the human body. This ability makes them easily detectable by existing sensors, as they emit light in the visible spectrum [69, 70, 71]. Multiple photon absorption is a nonlinear optical process. An electron gets excited to a virtual state and, after a relaxation period, during a non-radiative process, moves back to the ground level and produces a radiative emission with higher energy. Lanthanide upconversion techniques take advantage of the fact that real intermediate states have multiple long lifetimes.

Rare earth ions, or lanthanides, are a set of seventeen heavy metals. They are called rare earth ions because, although they are abundant in the Earth's crust, it is difficult and expensive to separate them from the primary ore. Rare-earth ions, particularly erbium, have been identified as potential single emitters in the visible and IR spectrum. $NaYF_4$ is one of the most popular lanthanide-doped nanoparticles made up of rare-earth ions. Erbium and ytterbium (Er^{3+} and Yb^{3+}) are the most common lanthanide ions utilized in photon upconversion, and they are also the most abundant. A combination of Er^{3+} and Yb^{3+} is used because Er^{3+} cannot absorb the NIR pump photon. In both bulk crystals and fibers, the absorption cross sections are small, and pump absorption rarely happens. On the other hand, the requirement to avoid excessive quenching processes places a limit on the doping concentration. Ytterbium (Yb^{3+}) sensitizer ions are a frequent solution to this problem. Pump radiation can be absorbed by ytterbium ions, which subsequently transmit the energy to ground-state erbium ions, bringing them to higher energy levels. The ions are then quickly transferred into the upper levels by absorbing more photons. Based on the number of absorbed photons by erbium ions, red, green, and blue emission can be seen. Figure 2.5 shows the electron energy levels in erbium (Er) doped nanoparticles. Since Er^{3+} cannot absorb 980nm photons, Yb^{3+} is used to ease the process.

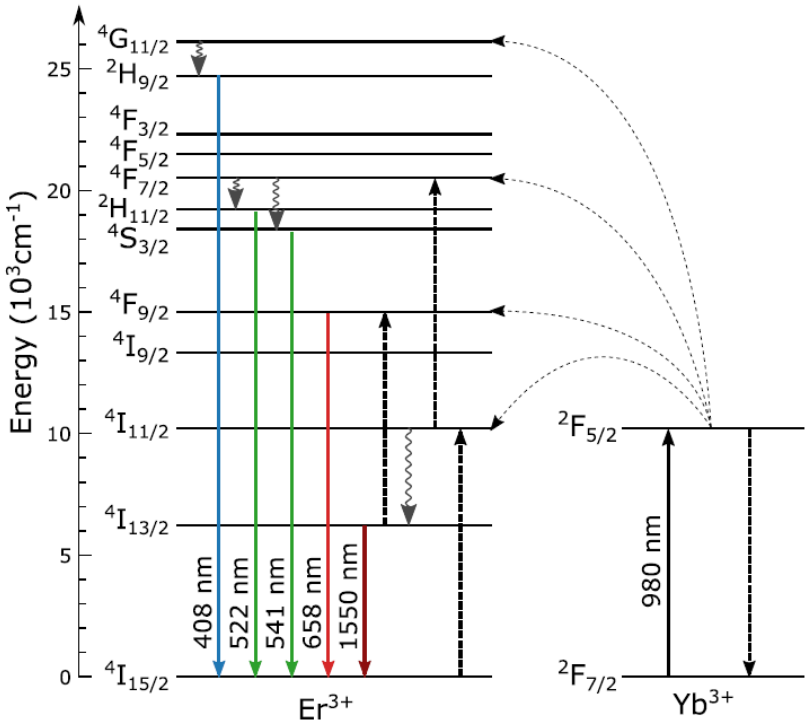

Figure 2.5: Schematic energy level diagram of the Yb^{3+} sensitizer and Er^{3+} activator in nanocrystals. Radiative energy transfer (solid lines), non-radiative energy transfer (dotted lines), cross-relaxation (dashed lines), and multiphonon relaxation (curly lines). Reprinted with permission from [5].

Upconversion from the mentioned $NaYF_4$ nanocrystals contains two or three photon absorptions. Er^{3+} ions , by energy transfer (ET) from the Yb^{3+}, first absorb a photon and gets excited from ground $^4I_{15/2}$ level to excited $^4I_{11/2}$ level. Another photon will be absorbed and take the excited ions from $^4I_{11/2}$ level to $^4F_{7/2}$. The ion then can experience a non radiative relaxation process and move to excited $^4H_{11/2}$, $^4S_{3/2}$, $^4F_{9/2}$ levels from $^4F_{7/2}$ level. Finally, through a radiative transition from each of these levels back to the ground $^4I_{15/2}$ level, emissions at 522, 541, and 658 nm can be observed, respectively. The excited ion at $^4F_{7/2}$ level absorbs one more photon and transfers to $^4G_{11/2}$ level. After a non-radiative relaxation, the ion can move to $^4H_{9/2}$. The excited ion at $^4H_{9/2}$ level can radiatively transit to the ground $^4I_{15/2}$ level and emits at 408 nm [72].

Another possible process here is when the optical emission from the excited state occurs at a wavelength longer than that of the optical pump. The process of using such $NaYF_4$ nanocrystals has attracted researchers because they can emit in the

infrared region as well [73, 74, 75, 76]. According to Figure 2.5, an excited ion at the $^4I_{11/2}$ level can emit at 1550 nm if it non-radiatively relaxes to the $^4I_{13/2}$ level and then moves back to the ground $^4I_{15/2}$ level [77, 78, 79].

Fibers doped with erbium–ytterbium are employed in erbium-doped amplifiers and short fibre lasers, used in the 1550 nm wavelength optical communication window [80]. These amplifiers at 2700 nm are also feasible to be used in medicine, sensing and military countermeasures [81, 82, 83]. The lanthanide ions are stable materials because their 4f orbital energies are the intermediate states that are isolated by the 6s and 6p orbitals and do not play a substantial role in bonding. Radiative decay is also more likely because of the host's ability to inhibit nonradiative decay [84]. However, they have a low conversion efficiency, which restricts their applications in developing single photon sources [85, 86].

2.4 Plasmon Enhanced Emission

Surface plasmon polaritons are electromagnetic waves that propagate along a metal-dielectric interface and are perpendicular to the interface [17]. Plasmonic nanostructures can increase the intensity of the received and transmitted electromagnetic waves due to the field enhancement that happens by increasing the light-matter interactions at subwavelength volumes [87]. Plasmon resonances in a nano aperture go beyond the diffraction limit. They can increase both radiative and non-radiative decay rates when used to enhance the emissions of nanoparticles [88]. The radiative decay rate of a nano particle is the sum of the intrinsic radiative decay rate and the enhanced radiative decay rate. The same definition can be used for the non-radiative decay rate. Therefore, emission enhancement happens when the total radiative decay rate is greater than that of the non-radiative decay rate [84]. In addition, increasing the incident photon absorption through the enhanced local field around the plasmonic structure has the additional effect of speeding up the conversion procedure [89]. In order to increase photon absorption, it is necessary to match the structure's plasmonic resonance to the absorption wavelength of the nanoparticles being studied. For Er-doped nanoparticles, the plasmonic nanostructure should be designed for resonances at 980 nm, which is the absorption wavelength of these nanoparticles.

2.5 Single Photon Sources

It's possible for light to be emitted in the form of a single photon from a single-photon source. Unlike lasers and light bulbs, single photon sources do not produce coherent or thermal light. When it comes to developing single-photon sources, researchers have focused on single atoms that operate as discrete emitters. nanocrystals of Praseodymium [90, 91, 92] cerium [93, 94, 95] and erbium [85, 96] are examples of single lanthanide emitters that have been studied to produce a single photon source. As mentioned before, lanthanide ions are stable materials due to isolation of their 4f orbital energies by the 6s and 6p orbitals. Their quantum state can also be controlled [95, 97, 98]. The key problem is determining how to reliably isolate a single lanthanide emitter [99, 100]. Previous research has suggested looking for nanocrystals at random [90] or using low emitter concentrations [101]. The other challenge is to enhance emission from lanthanides. This is important specially when using erbium to emit at 1550 nm which is low loss band used in fiber optics. Usually, the emission at this wavelength has lower intensity than visible wavelength. Therefore, the emission needs to be enhanced enough to make the emission at this wavelength detectable and stable. One suggested option to overcome this issue was to use optical cavities around the emitters [85, 86]. However, this method is not reliable, because random distributions of emitters bring more than one emitter in a single aperture. It was discovered that researchers could implant as little as four ions in one location in a crystal with accuracy of 50 nanometers. This new method resulted in single spots that displayed the characteristic of discrete emission levels; however, the yield of emission was only 50% [102].

An additional method for isolating and measuring emission of single erbium ion emitters in NaYF4 nanocrystals using plasmonic rectangular aperture optical tweezer was recently developed by our group [103]. Single erbium nanocrystals may be consistently detected because of the plasmonic aperture's enhanced radiative rate. This work was a step forward in achieving the single-photon sources but the enhancement is still low to see the emission at 1550 nm. Other works have also seen enhanced single-photon emission from nanoapertures in metals at visible spectrum [104]. In section 3.2 and Appendix B, we describe our work where double nanohole optical tweezers have been used to achieve a much higher emission of single erbium at 1550 nm.

2.6 Optical Tweezers

Photons have the ability to impose force and torque on the particles with which they interact. Maxwell proposed the concept of radiation pressure for light and electromagnetic waves first [105, 106]. The original force of light is small and cannot overcome the friction and gravitation force. So it's hard to find a practical application for them. For the first time, Arthur Ashkin discovered that although these forces are small, they are strong enough to move subwavelength particles [107]. Ashkin used this concept to move and direct tiny particles experimentally [108, 109]. Experiments carried out by Ashkin revealed that the beam's intensity gradient produces a longitudinal component known as scattering force and a transverse component known as gradient force. Figure 2.6 shows the gradient and scattering force acting on a dielectric particle. In 1986, he discovered the characteristics of these forces, which led to the development of a three-dimensional trap [110]. A laser beam was utilized to trap dielectric particles using optical gradient force. This technique is known as optical tweezers. When a single particle is of interest, optical tweezers may be used to trap and study the particle [111].

While in the Mie regime, the interaction of light with a particle can be studied using Ray optics, the interaction of light with subwavelength particles is a bit more complicated. The scattering and gradient forces may be calculated by treating the particle as a point dipole that interacts with the incident beam [112].

$$F_{\text{scat}} = \frac{I_0}{c}\frac{128\pi^2\left(\frac{d}{2}\right)^6}{3\lambda^4}\left(\frac{n_p^2-n_m^2}{n_p^2+2n_m^2}\right)^2 n_m \tag{2.8}$$

$$F_{\text{grad}} = \frac{1}{2}n_m\alpha\nabla|E|^2 = \frac{n_m^3\left(\frac{d}{2}\right)^3}{2}\left(\frac{n_p^2-n_m^2}{n_p^2+2n_m^2}\right)^2\nabla|E|^2 \tag{2.9}$$

where c and d are the speed of light and diameter of the particle. I_0 is beam intensity and λ is the wavelength. n_m and n_p are the refractive indexes of the background medium and particle. α is the polarizability of the particle and E shows the electric field.

From Eq. 2.8 and Eq. 2.9, we find that

$$F_{\text{scat}} \propto \frac{r^6}{\lambda^4} \tag{2.10}$$

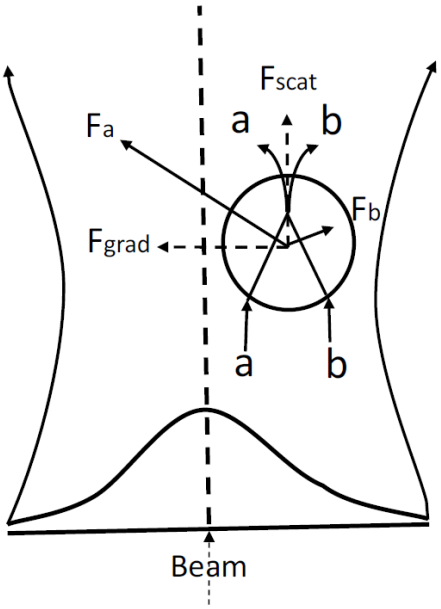

Figure 2.6: The gradient and scattering force acting on a dielectric particle displaced from the axis of a Gaussian laser beam. The curved lines at the left and right represent the shape of the laser beam and the Gaussian curve represents the intensity profile of the beam. Two rays of light from the laser beam are shown as a and b. The refraction of light by the particle changes the momentum of the photons, which results in the forces F_a and F_b. Reprinted with permission from [6].

and

$$F_{\text{grad}} \propto r^3 \tag{2.11}$$

Where r is the radius of the particle. Equation 2.10 and 2.10 proves that the gradient force shows more changes with the change in the particle size. That means, for small particles, the gradient force becomes small and makes the trapping more challenging. Stable trapping of Rayleigh sized particles, requires a higher beam power to provide an adequate gradient force [113] which can have damaging effects on the particles, especially on bio-nanoparticles. To address this issue, the Self-Induced Back Action (SIBA) approach is employed. Instead of using an external monitoring or correction system, this technology makes use of particle-nanostructure interaction to enable automatic feedback control. It is important to well design a nanostructure containing the nanoparticle to have enough field enhancement for a stable trap. The momentum of the photons interacting with the trapped particle fluctuates significantly as they jump around the trapping area. Because of momentum conservation, the object's dynamics are automatically synced with these changes. During

high-energy events, the force adjusts the potential well depth to keep the particle in equilibrium [6]. This method differs from prior systems that rely on an external feedback mechanism [114, 115, 116]. SIBA is a phenomenon that may be used in conjunction with various nanoaperture designs [110, 117, 118, 118, 119] and photonic crystals [120] to trap nanometre-sized particles with extremely low laser power.

2.7 Plasmonic Subwavelength Nanoapertures

We mentioned in the previous section that increasing the laser power to increase the optical gradient force for subwavelength particles can be harmful to the particles. The best-known solution to this issue is to use subwavelength apertures in metal films that produce localized surface plasmon and, thereby, a highly enhanced field [16]. This enhanced field helps with both improving optical trapping efficiency and emission enhancement. Optical trapping of sub-100 nm particles can be achieved using these structures. Different structures, such as circular [7, 114], bow-tie [8, 121, 122], double nanohole (DNH) [8], rectangular [10, 104], co-axial [123, 124] nanoapertures and nanoantenna designs [125, 126, 127] have been proposed and used in trapping. These types of apertures have been shown in Figure 2.7.

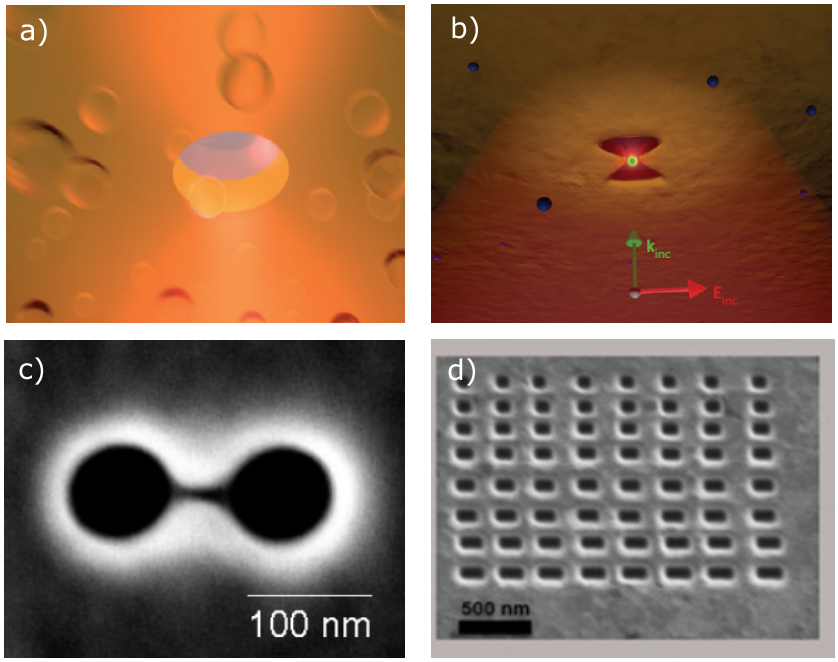

Figure 2.7: Nanoaperture designs (a) Circular aperture. reprinted with permission from [7] (b) Bowtie nanoaperture (BNA) at the fiber tip. reprinted with permission from [8] (c) Double nanohole aperture. Reprinted with permission from [9] (d) Rectangular plasmonic nanocavity.Reprinted (adapted) with permission from [10].Copyright © 2019, American Chemical Society.

One of the first attempts at plasmonic nanoaperture optical trapping used a 500 *nm* circular aperture made using nanosphere lithography to trap 200 *nm* fluorescent latex beads in water [114]. Afterward, Gordon et al. proved SIBA in optical trapping, which was crucial in understanding the efficiency of nanoapertures in optical trap-

ping [7]. In another work, a 310 circular aperture was fabricated using focused ion beam milling and used to trap a single 50 polystyrene in water. As a result of these findings, optical trapping with double-nanohole (DNH) apertures became an attractive case for studying nanoparticles [113, 128]. They also showed higher transmission than the other apertures [129]. DNHs generate an enhanced field and consequently create a potential well surrounding its cusp [130]. DNHs take advantage of self induced back action (SIBA). In these apertures, as the trapped particle is pulled out of the equilibrium point in trapping potential well, an optical trap provides a restoring force to get the particle back into trapping and creates a stable trapping. Figure 2.8 shows the field distribution at the cusp of a double-nanohole aperture using FDTD simulation.

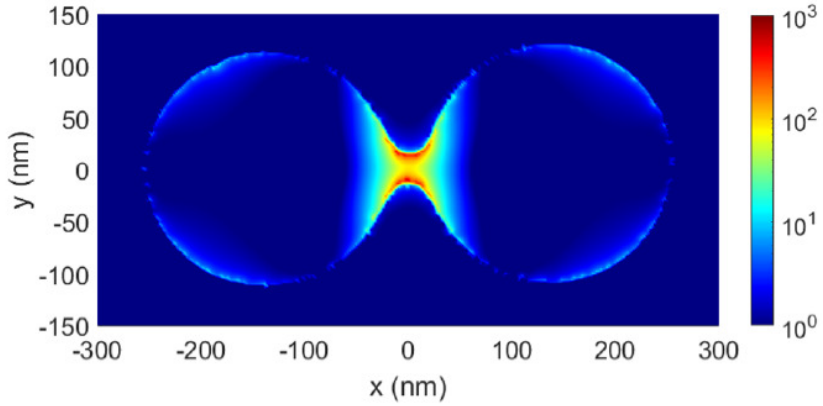

Figure 2.8: Visualization of the electric field intensity inside of a DNH with 32 nm cusp separation. Reprinted with permission from [11].

Another benefit of using double nanoholes for optical trapping is its feasibility.

A simple and cost-effective fabrication method using colloidal lithography has been proposed by Lalitha Ravindranath et al [14]. His method was used to create the DNH structures in this dissertation.

2.8 Colloidal Lithography Method to Fabricate DNH Apertures

Different methods have been exploited by the researchers such as electron beam lithography [12], focused ion beam milling [13] and colloidal lithography [131] to fabricate nano apertures. Figure 2.9(a) shows a nanohole in an aluminium film on silica coverslip as the substrate, made using electron beam lithography. The fabricated nanohole is far less than 100 nm diameter [12]. Figure 2.9(b) shows a bull's eye structure of Ag films with the thickness of 300-nm fabricated by focused ion beam (FIB) milling..

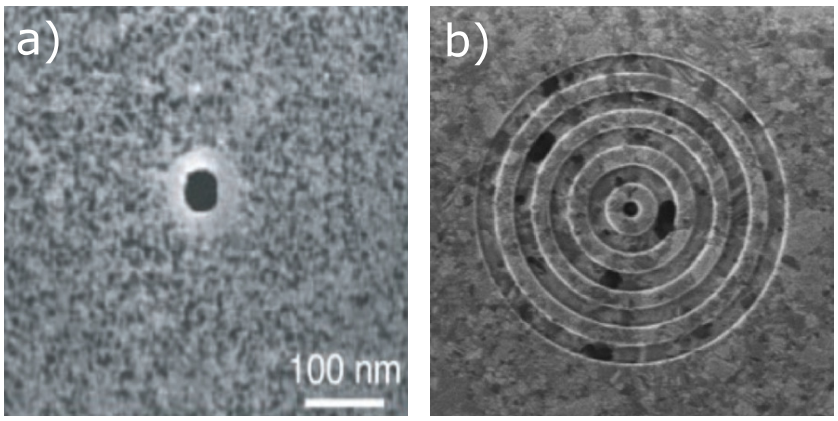

Figure 2.9: a) A nano hole fabricated using electron beam lithography. Reprinted with permission from [12] b) FIB micrograph image of a bull's eye structure surrounding a cylindrical hole in Ag film. Reprinted with permission from [13].

The Colloidal lithography which is used in this dissertation is more feasible and economical than the abovementioned methods. Lithography, a technique for imprinting using a template that was pioneered by Alois Senefelder, has found application in micro and nanofabrication. The first reported lithography efforts used dispersed colloidal spheres generated by standard emulsion polymerization or sol-gel synthesis methods [132, 133, 134, 135]. This method is based on the production of random or array crystals of colloidal particles on substrate surfaces. The particles are then employed as a mask for etching or deposition. Colloidal lithography is the name given to this process. With the use of techniques like angle-resolved colloidal lithography, the creation of complex patterns may be achieved [136]. Tuning of aperture dimensions using an organic solvent or deformation can also be obtained by plasma etching [137]. The optical properties [138, 139, 140] and trapping ability [114] of single nanoholes fabricated using colloidal lithography have been extensively studied. Fab-

rication of doublenanohole apertures using colloidal lithography and their non-linear optical properties has also been investigated [141]. However, it was challenging to create apertures smaller than 100 nm using colloidal lithography for the fabrication of DNHs. A customized colloidal lithography technique with dimension tuning was recently proposed by our group [14]. They were able to produce apertures with cusp separations of less than 10 nm. By choosing a suitable etching time, tuning of the cusp and diameter of the apertures can be achieved.

Figure 2.10 shows the process of fabricating DNHs using colloidal lithography [14]. As the first step, the glass cover slides are cut to appropriate dimensions, sonicated in an ethanol Bath, and blow-dried with compressed nitrogen to have clean and transparent glass slides.

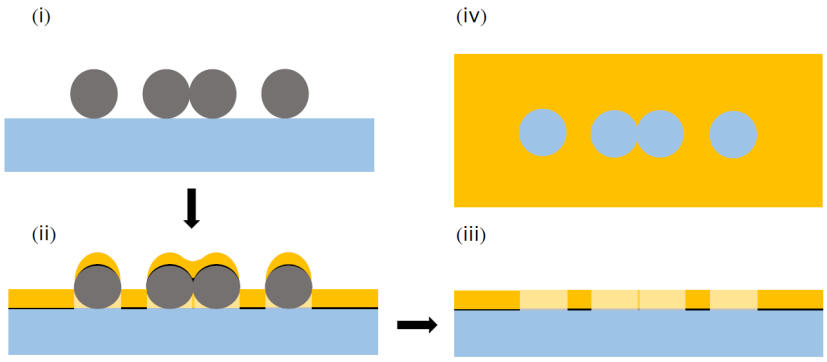

Figure 2.10: The process of fabrication DNH using colloidal lithography. (i) polystyrene spheres drop coated on a glass substrate. (ii) Au-Ti layers Sputtered on the glass substrate with spheres. (iii) the structure is sonicated in ethanol after sputtering. (iv) Top-view of the nano apertures in gold film. Reprinted with permission from [14].

The glass slides are used as the substrate for the fabricated samples. Before starting the fabrication process, the appropriate diameter of the polystyrene spheres, based on the final nano aperture sizes, is decided. Next, a 0.01% w/v colloidal suspension in ethanol (this is the optimal concentration to create DNH on such samples) is prepared. The prepared suspension is then drop-coated on the clean cover slides uniformly. The polystyrene spheres will adhere to the surface of the substrate as the solution dries out during 24 hours of rest. During ethanol evaporation, polystyrene spheres join together into clusters and stick to the surface of the substrate. Using the plasma etching procedure, the prepared samples are then fine-tuned to get DNHs with the desired diameters and cusp separations. After a specific calculated etch time, each

sample will be removed from the machine. Then an AMF's Mantis QUBE system is used to deposit a thin layer of 5nm titanium and then 70 nm gold film. After the sputtering is complete, the samples are subsequently sonicated in a Toluene bath for at least 2 minutes to remove the polystyrene beads. After removing the beads, the appropriate apertures are produced in the sample.

Figure 2.11 shows a scanning electron microscope (SEM) image of one of the samples used in this dissertation and made using colloidal lithography. Figure 2.11(a) shows a wider area on the surface that shows the existence of single, double, and triple holes on the gold film. Figure 2.11(b) shows a close up of a DNH with diameter of 246 nm and cusp separation of 44 nm. This size has been achieved using 300 nm polystyrene beads and after etching for 80 seconds.

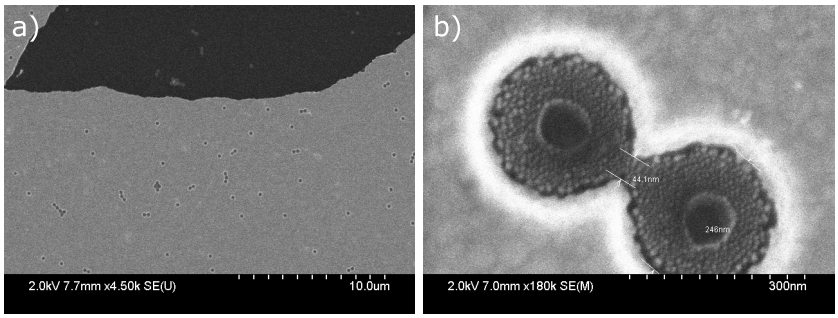

Figure 2.11: Colloidal lithography double-nanohole aperture collocation using images from scanning electron microscope (SEM) a) a wide area on the surface. b) Close up of a double-nanohole with 44.1 nm gap size.

Chapter 3

Contributions

In this chapter, the contributions of the author through four published papers are presented. Sections 3.1 to 3.4 provide an overview of each paper separately. The full manuscripts, in detail, are attached to the dissertation as Appendices A to D. In the first section, a modified analyzing method using single-mode matching theory and the orthogonality principle is used to calculate the reflection and then the plasmonic resonances in a MIM structure. In the next section, using the fabricated DNH structure, the trapping, upconversion, and emission at 1550nm of Er-doped nanoparticles are studied. In section 3.3, a new design has been proposed to achieve high sensitivity sensors using the existing commercial prism-based structure. In the last section, a method is demonstrated to identify the location and orientation of DNHs in-situ without the need for SEM or other complicated processes.

3.1 Large Plasmonic Resonance Shifts from Metal Loss in Slits (Appendix A)

The efficiency of optical processes for a plasmonic nanostructure is typically scaled with the optical quality factor to the mode volume. Although metallic cavities do not have high quality factors, their low mode volume helps to increase the efficiency of the optical processes. The mode volume is the number of bound modes that an optical cavity can support.

In nano scale cavities or particularly MIM structures, resonances can be excited to concentrate light to nanoscale dimensions. MIM structures also increase the optical absorption of materials at the MIM end faces. Because of these great features, they

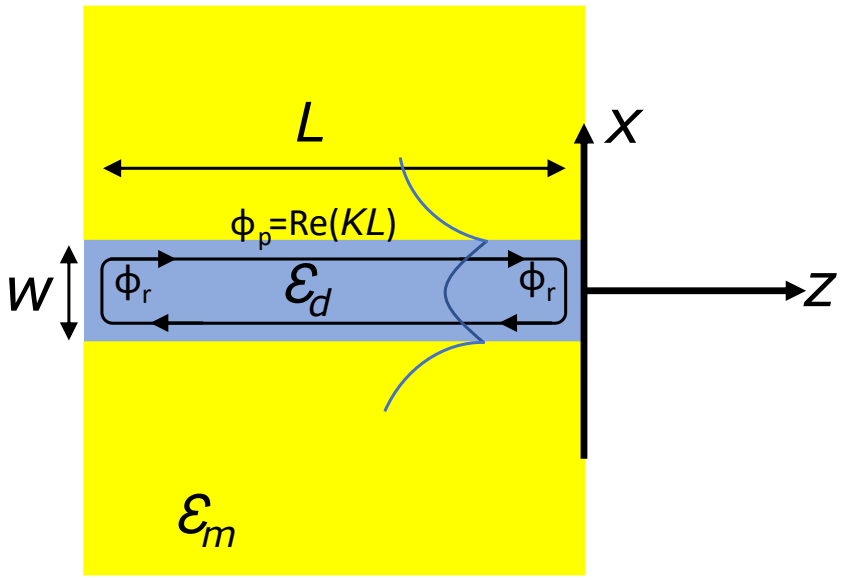

Figure 3.1: Schematic representation of the slit with complex permittivity ϵ_d in a real metal with complex permittivity ϵ_m. The electric field profile of the symmetric SPP mode is shown.

can be used for single molecule sensing, optical trapping, surface plasmon-polariton (SPP) modulators, and SPP sources. The easy and cost-effective fabrication of these structures is another significant feature of them. For these reasons, it is critical to have a thorough understanding of the resonant behaviour of MIM cavities. These cavities experience multiple reflections from the end faces. These reflections are constructive and give rise to Fabry-Pérot resonances. The reflection phase has a significant effect on the plasmonic wavelength. The SPP dispersion must be taken into account when designing a plasmonic device for a certain wavelength. Figure 3.1 shows the schematic representation of the slit. The dispersion relation that shows the relation between plasmonic wavelengths and reflection phase is given as

$$\Phi_r = m\pi - k_z L \tag{3.1}$$

where L is the length of the slit and $m = 1, 2, 3, ...$ is the order of the resonance. This formula comes from the condition that maximizes the transmission at the termination of the cavity. Therefore, a correct calculation of the reflection phase is important. One of the main parameters that affects reflection is the loss of the metal. Metal loss can be considered in the phase calculation by considering the imaginary part of the relative permittivity of the metal. The correct calculation of the reflec-

tion phase has been done for ideal metals (metals without loss) [142]. Another group at Stanford University developed the analysis of the impact of loss on the reflection phase by considering metal loss [143]. However, the calculation of the reflection phase in this work is inaccurate. They used a single mode matching theory to match the fundamental TM mode of the cavity with the plane wave modes of the adjacent medium at the cavity end faces. They used the continuity of the electric and magnetic fields at the interface and then the conjugated form of the orthogonality relation to calculate the reflection coefficient. This method is fully described in Ref. [143]. The reason the conjugated form is inaccurate is that it gives non-zero values to different modes. Here we use the unconjugated form of the orthogonality relation for the reflection calculation because it isolates each mode given a value of zero for different modes. In the case of a single-mode matching approximation, the unconjugated form is therefore more accurate. We also consider metal loss in our calculations. The full set of calculations is presented in Appendix A. After calculation of the reflection phase, we compare the results for the lossy and lossless cases for different slit widths. Figure 3.2 shows the results for an Au-air-Au structure. The difference between the lossy and lossless cases is clear. At short wavelengths, the mode index in the lossy case does not increase as much as it does in the lossless case. As the SPP mode is driven out of the metal at longer wavelengths, the reflection properties are identical to the lossless case.

Figure 3.3 compares the results of the unconjugated and conjugated forms of the orthogonality relation. The results show the difference between the two methods, especially at shorter wavelengths. The changes in the refractive index of the metal at shorter wavelengths are greater. This results in faster changes in the mismatch between the modes inside and outside the cavity. As mentioned before, the conjugated form gives non-zero values to different modes, and that affects the mismatch even more.

An FDTD simulation has been done to verify our results. Figure 3.4 shows the electric and magnetic fields inside the cavity. The largest amplitudes in the electric field are towards both end faces, whereas the magnetic field has a peak at the center, which represents the standing wave of order m=1. This proves the existence of constructive interference and field enhancement in the cavity.

We finally plotted the dispersion curve for the Au–silica–Au structure. The FDTD results, past experimental results [144], the results using our method and the dispersion calculation without considering the reflection phase are compared. The results

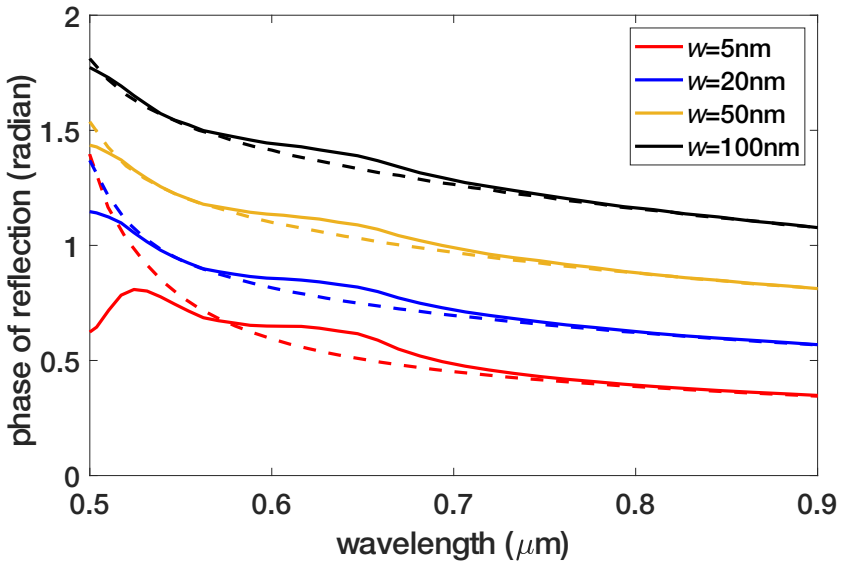

Figure 3.2: Reflection phase for an Au-air-Au structure as a function of wavelength for different slit width. Solid lines show the results for the lossy cases and dashed lines show the results for the lossless cases.

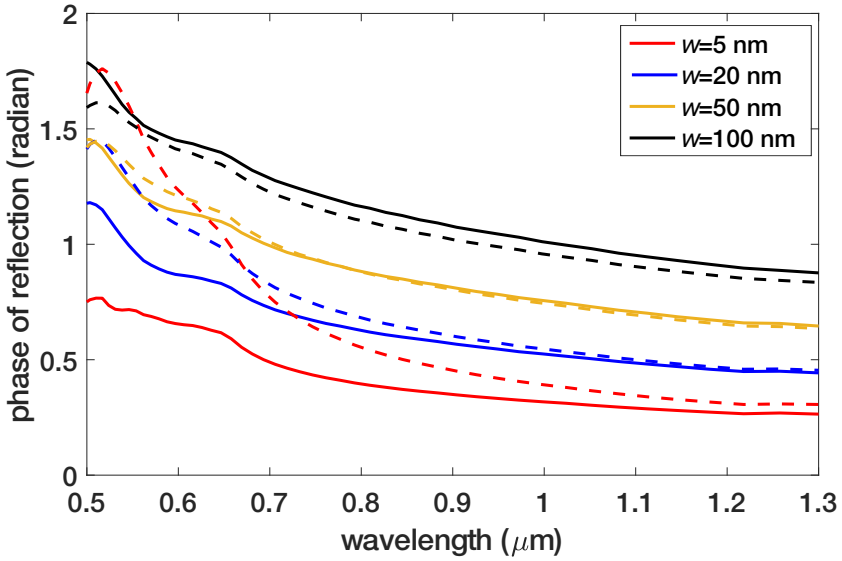

Figure 3.3: Reflection phase for an Au-air-Au structure as a function of wavelength for different slit width. Solid lines show the results using unconjugated form of the orthogonality and dashed lines show the results using the conjugated form of the orthogonality.

in Figure 3.5 show good agreement between our results and the experimental data. The slight difference between our results and the experimental data comes from the simplification of ignoring the evanescent modes inside the cavity. Since these modes

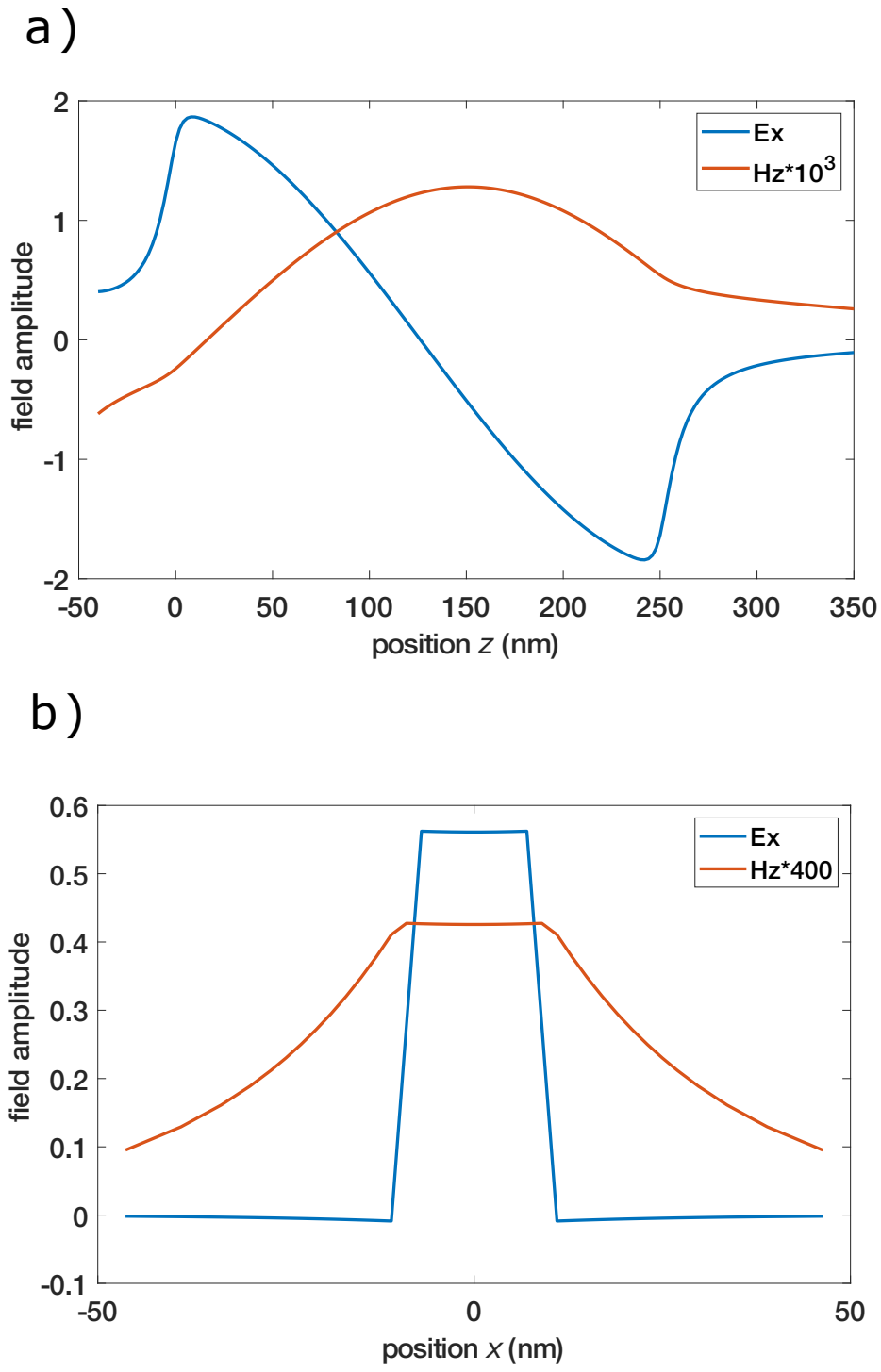

Figure 3.4: Electric and magnetic fields inside the structure a) in the z direction (for $x = 0$. b) in the x direction (for $z = 150$ nm.

are not expected to transmit energy in the direction of propagation for sufficiently long cavities, we ignored the contribution of these modes in our calculation. To consider the slight effect of the evanescent modes, the term $exp(-k_z z)$ can be added to the equations for continuity of the electric and magnetic fields.

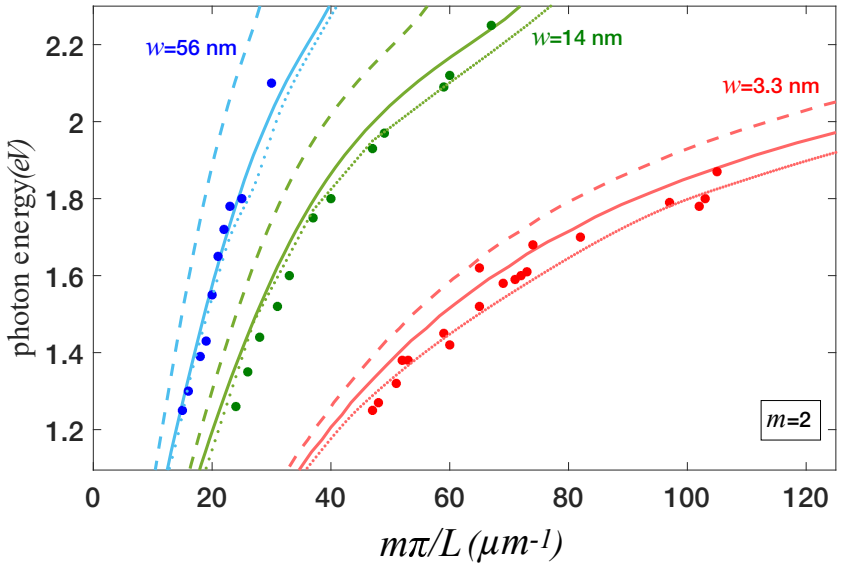

Figure 3.5: Dispersion relation for an Au-Silica-Au structure. Solid lines: calculation of dispersion considering the effect of the reflection phase calculated using unconjugated form of the orthogonality relation. Dashed lines: calculation of dispersion ignoring the effect of the reflection phase as was done in the past analysis. Dotted lines: FDTD simulation. Discrete points: experimental results using the experimentally measured plasmonic resonances [144]. The theory presented above shows good agreement with both FDTD and experiment.

To summarize, in this work, we modified the single mode matching theory for the calculation of the reflection phase by considering the unconjugated form of the orthogonality relation in MIM cavities. Then, the effect of metal loss on plasmonic wavelengths has been investigated using the correct calculation of the reflection phase.

3.2 Isolating and Enhancing Single-Photon Emitters for 1550 nm Quantum Light Sources Using Double Nanohole Optical Tweezers (Appendix B)

Optical tweezers use optical gradient force to trap nanoparticles. The gradient force is proportional to the size of the particle. Consequently, trapping particles smaller than 100 nm is challenging because of the lower gradient force [110]. Metallic nanostructures are good candidates to enhance the electric field at optical resonances [2]. Using metallic nanostructures in optical tweezers compensates for the low gradient force of the sub-wavelength particles and creates enough field enhancement to trap the particle without the need to increase the laser power. Plasmonic nanostructures also take advantage of the self-induced back action (SIBA) technique to keep the particle in trapping and isolate the particle. A wide range of nanoapertures have been proposed for the optical trapping of sub-Rayleigh particles, such as bow-tie [8, 122, 127], rectangular [10, 145], and DNH [146, 147] apertures [10, 148]. Multiple plasmonic resonances have also been demonstrated in nanohole arrays and other plasmonic structures. Using optical tweezers with plasmon-enhanced metallic apertures to trap lanthanide-doped particles has an additional benefit as it both isolates the particles and can enhance their emission rate [84, 148]. The field enhancement from the plasmonic effects allows nanoparticles under 100 nm to be isolated in the aperture [149] and can also enhance the emission by increasing the radiative decay rate [84].

In this work, lanthanide doped upconversion nanoparticles with 2% of erbium and 18% of ytterbium have been trapped and isolated using DNH apertures. Erbium ions can absorb 980 nm incident light through energy transfer from ytterbium and emit at 400nm, 550 nm, 650 nm and 1550 nm. Our group has previously measured enhancement from upconversion nanocrystals in hexane (as the solvent) and optically trapped them in rectangular apertures [103], but a DNH structure is expected to provide higher field enhancement and correspondingly higher emission enhancement. Taking advantage of this field enhancement they were able to see the emission at 550 and 650 nm.

Here, in our work, the first step was to fabricate DNH structures in a 70 nm gold layer on a glass substrate using the colloidal lithography method. The DNH aperture enhances the local field around its cusps and has multiple resonances. The samples

were made with different average cusp separations, from 26 nm to 95 nm. Figure 3.6 shows an SEM image of one of the fabricated DNH apertures.

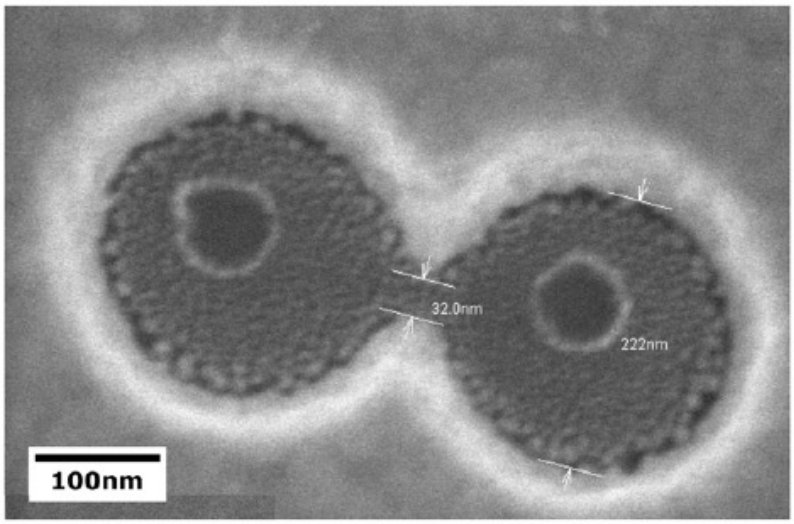

Figure 3.6: Image of a fabricated DNH structure with 32 nm cusp separation and 222 nm aperture diameter, taken with a scanning electron microscope.

Figure 3.7 shows the optical trapping setup that has been used to trap and isolate the particles and get the enhanced emission. The laser beam is expanded and focused on the DNH aperture using a beam expander and objective lens correspondingly. The highly enhanced field creates a trapping potential well around the cusp of the target DNH. This potential well causes the particles to be pulled into trapping. In chapter 2, we mentioned that the dielectric of the surrounding medium is an important factor in trapping the particle. So, here, hexane has been used to make the trap easier.

The transmitted wave due to the excitation of the particle with a laser beam is collected in an APD (avalanche photodiode) and is shown in Figure 3.8. A clear jump immediately after turning the laser on is observed. That means, thanks to the field enhancement created by the DNHs, we can easily trap the nanoparticle. The trapping is also very stable and helps to isolate the particle on the cusp of the DNH.

The next step was to collect the reflected signal and study the emission from the particles. A visible spectrometer and an NIR spectrometer were connected to the setup to read the spectrum in different wavelength ranges. Different peaks at 400 nm, 550 nm, 650 nm, and 1550 nm were observed. The peaks at 400 nm and 1550 nm weren't seen in the past work using rectangular apertures. That shows higher field enhancement of the DNH structure. The emission counts also show a

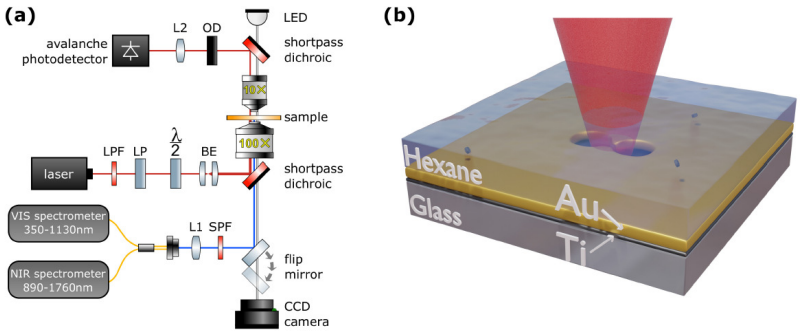

Figure 3.7: (a) Schematic of the optical tweezers setup used to trap and excite upconversion nanoparticles. (b) Schematic drawing of trapping an upconversion nanocrystal in a double nanohole.

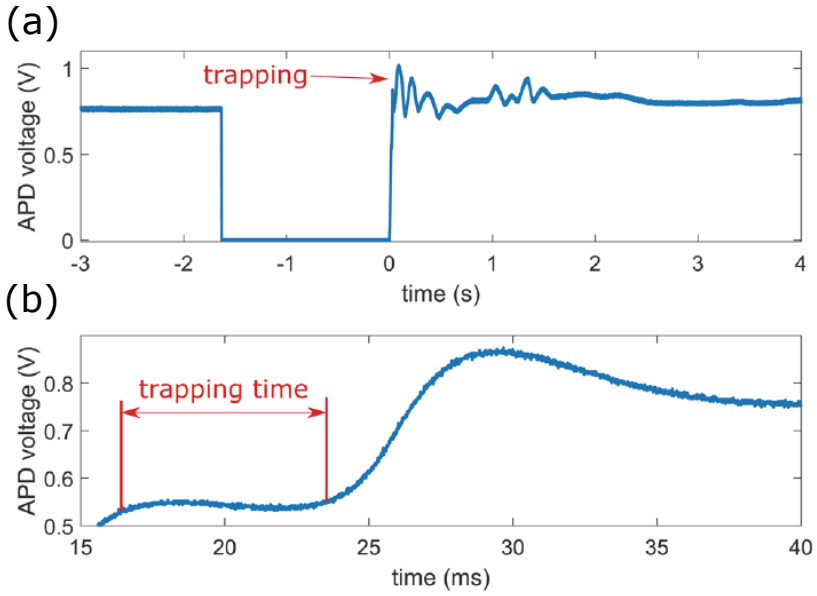

Figure 3.8: (a) Optical transmission through a 32 nm DNH aperture in a metal film trapping a 26.2 nm nanocrystal, as measured by the APD voltage. The laser is turned on at 0 s. (b) Magnified region showing the APD voltage change shortly after the laser is turned on and trapping time measurement.

50-fold improvement in the emission from the DNH aperture in comparison with the rectangular aperture.

We then repeated the measurement for samples of different sizes and for different particle sizes to find out which sample give the highest field enhancement. The results are shown in Figure 3.9. The sample with a cusp separation of 32 nm showed the highest field enhancement. In chapter 2 we mentioned that as the particle size de-

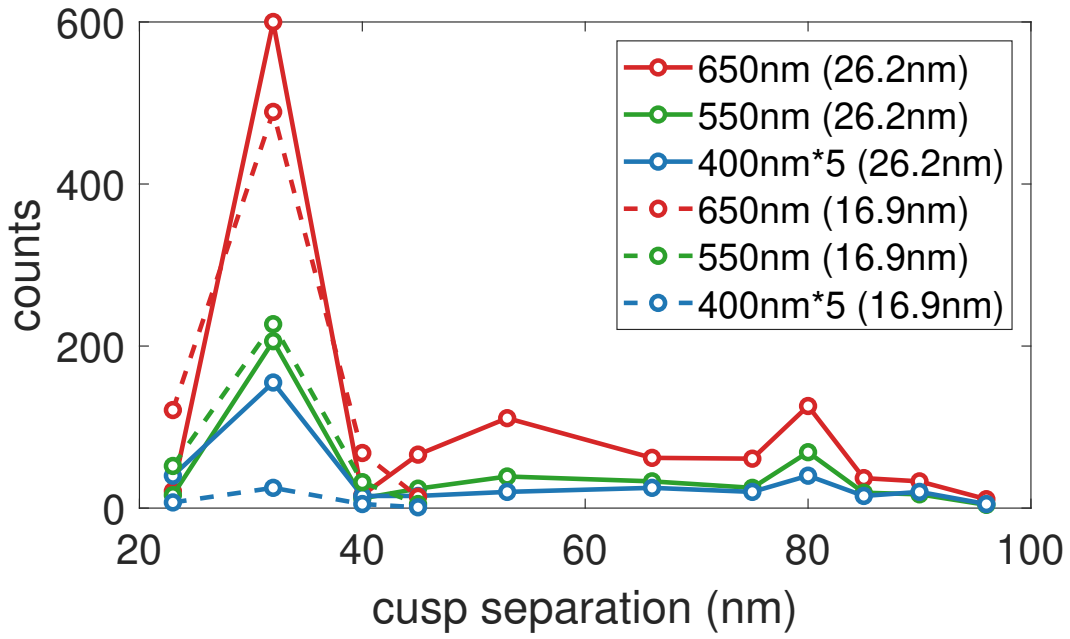

Figure 3.9: Investigating the influence of the DNH cusp separation on emission enhancement. Emission from 17 nm and 26 nm nanocrystals at 400 nm, 550 nm, 650 nm for varying DNH cusp separations. Emission counts at 400 nm are multiplied by 5 for visibility.

creases the gradient force and so the optical enahncement decreases. Therefore using the particle with a size of 26 nm gives more enhancement. These results show that the resonance wavelengths shift as the cusp separation changes. The colloidal lithography method used to prepare these samples adjusts the cusp separation by changing the plasma etching time, and this also affects the diameter of the apertures. Changing both the cusp separation and aperture diameter can impact both the enhancement factor and resonant wavelengths.

For the next step, using the sample with 32 nm cusp separation, we took a hundred measurements and recorded the emission at 650 nm. The measurements have been done for nanocrystals with a nominal diameter of 22.7 nm (standard deviation of 2.4 nm) and a nominal number of Er ions per nanocrystal of 2.48. The purpose of using these new nanocrystals was to have particles with the lowest number of erbium and, in other words, to have single emitters. We observed seven discrete levels in the visible spectrometer for those measurements, as shown in Figure 3.10. The acquisition time is 10 ms. This result proves that we can categorize the emission results and associate each level with the number of emitters in that level. For example, the results with a

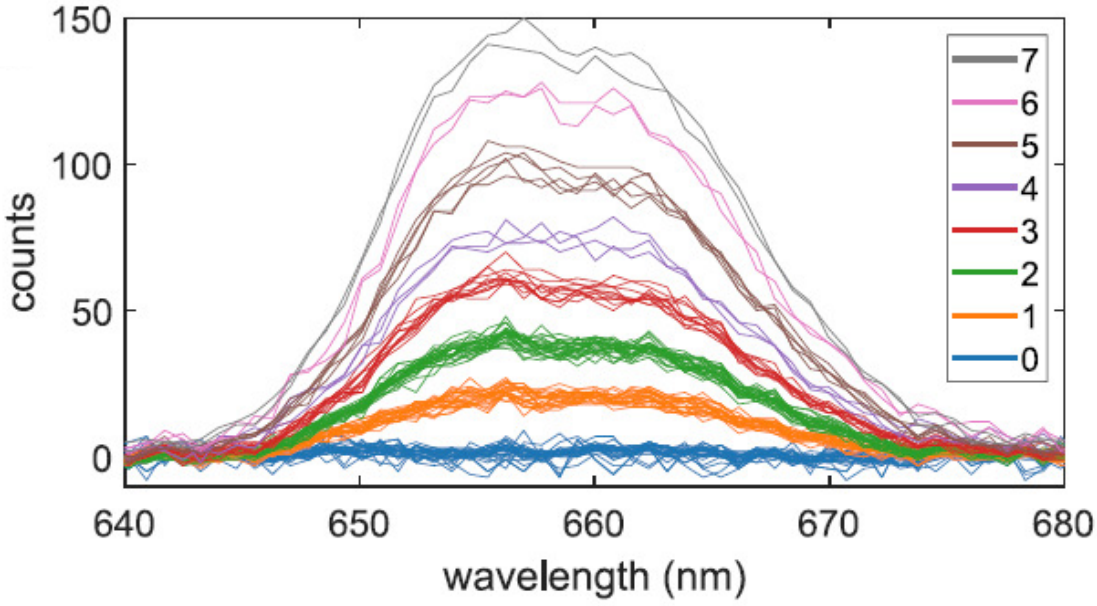

Figure 3.10: Emission counts from nanocrystals showing discrete levels corresponding to different amounts of active erbium emitters. Collected by a spectrometer with 1 s acquisition time.

zero count show the emission from zero emitter particles and the results with emission counts of around 30 are from the particles with single emitters.

The same procedure has been used to get the discrete levels at 1550 nm. This time we used 500 nm polystyrene to fabricate DNHs with the same cusp separation but bigger diameters. Using these samples, we are looking forward to getting more enhancement and being able to see higher emission counts at 1550 nm. Because from the previous measurements, we learned that the emission at 1550 nm is naturally far lower than the emission at 650 nm. Therefore, higher enhancement may result in higher counts at 1550 nm.

Figure 3.11 shows the final result that proves the sample with a 24 nm cusp separation gives the most enhancement. The particle size in this experiment was 24 nm. Figure 3.12 shows the emission spectra from 24 nm nanocrystals observed for a sample with an average cusp separation of 24 nm. The acquisition time is 1 s in this case. We found that the counts are three times greater than the counts from previous samples made of 300 nm polystyrene. This helped us to see clear peaks at 1550 nm for single emitters with less than expected integration time. Figure 3.13 shows the discrete levels at 1550 nm for a particle size of 24 nm. Now, we know that by using

these samples with a 24 nm cusp separation, we can get an emission count of around 100 for 10 s of acquisition time. So whenever we trap a particle that has 100 counts, we know that particle is a single emitter.

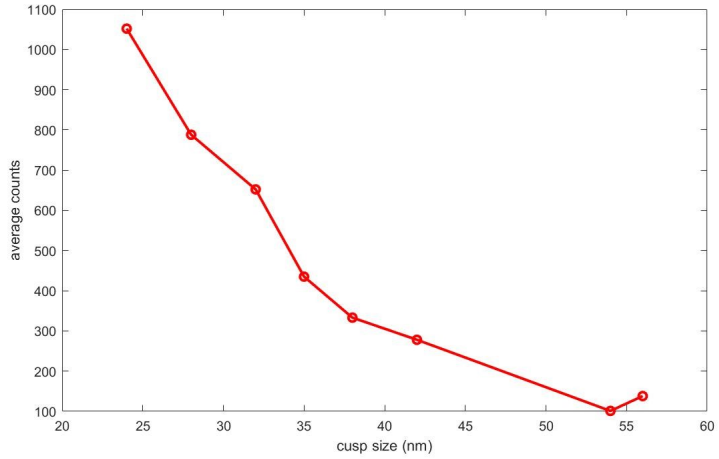

Figure 3.11: Investigating the influence of the DNH cusp separation on emission enhancement. Emission from 24 nm nanocrystals at 1550 nm for varying DNH cusp separations.

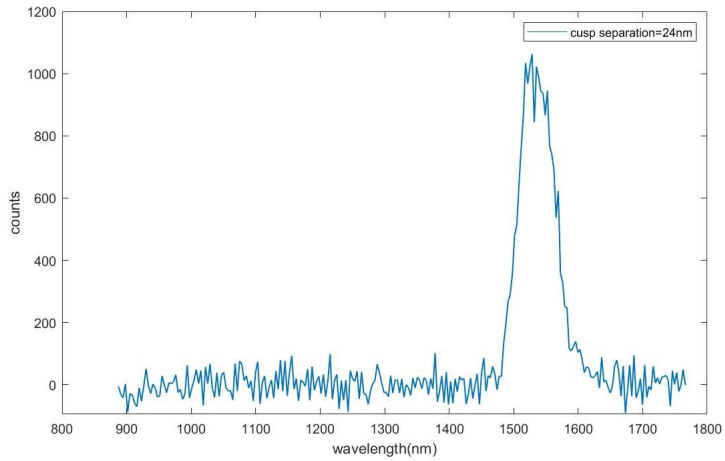

Figure 3.12: Emission at 1550 nm from a 24 nm nanocrystal observed for a sample with 24 nm average cusp separation. Collected by a spectrometer with 1 s acquisition time.

The final step will be to isolate the single emitters in the cusp separation of DNHs forever, excite the structure with a 980 nm laser, and study the emission at a single photon detector to get single photons.

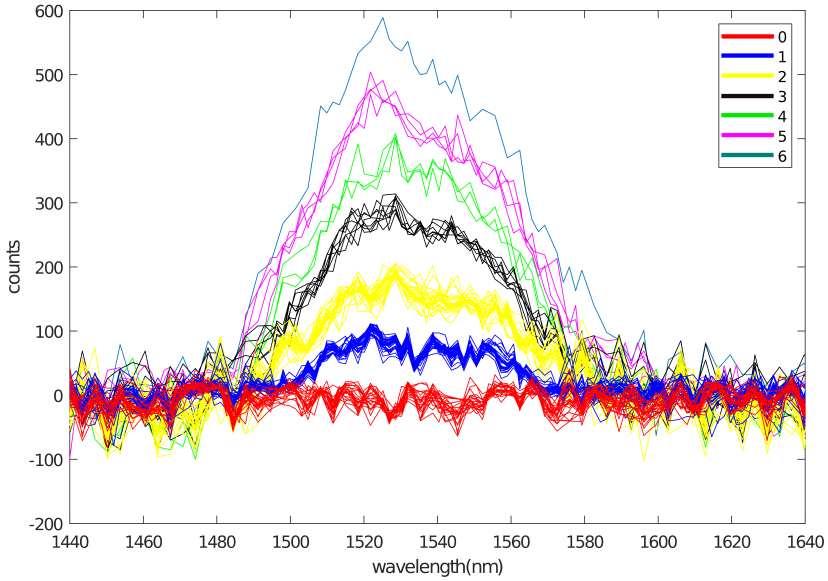

Figure 3.13: Emission counts from nanocrystals showing discrete levels corresponding to different amounts of active erbium emitters. Collected by a spectrometer with a 10 s acquisition time.

3.3 Improving Sensitivity of Existing Surface Plasmon Resonance Systems with Grating-Coupled Short-Range Surface Plasmons (Appendix C)

In chapter 2, we introduced localized surface plasmons, which are non-propagating modes of surface plasmon waves at the interface of a metal and a dielectric. They are scattering of a conductive nanoparticle in an oscillating incident light. To increase the coupling between the surface plasmon and the incident light, using multilayer structures, the IMI structure is proposed [52]. IMI structures take advantage of the coupling between each metal-dielectric interface and experience constructing enhanced fields. The other feature of the IMI structure is that, by specific design they can support short-range surface plasmon mode as well. As the metal layer thickness decreases, SRSP provides more confinement and enhancement of the light within the metal. SRSP mode also has a higher effective mode index and a larger propagation constant than the usual SPPs. One of the main applications of IMI structures is in designing SPR sensors. SPR sensors are used for the pharmaceutical industry, water safety testing, and medical diagnostics such as blood testing.

A conventional SPR sensor is made of three layers: a glass prism, a gold film, and the analyte layer. The analyte layer is usually water because, in most sensing applications, the particles being measured are dissolving in water. In addition, the water has a refractive index of 1.33, which gives rise to surface plasmon waves. The effect of the refractive index of the dielectric in creating surface plasmon resonance has been discussed in chapter 2. The attenuated total reflection (ATR) method is used to detect the changes in the refractive index of the analyte layer [4]. Incident light with a specific angle excites the structure through the prism, and at a particular wavelength, a dip in the reflection on the other side of the prism will be detected. Due to the lossy nature of the metal, light is absorbed at the coupling condition, resulting in a dip in the total reflection.

In this work, the aim is to propose a new design for SPR sensors to increase the sensitivity and resolution of the sensor. In order to increase surface sensitivity, the employment of short-range surface plasmon (SRSP) modes is one possible avenue. To do so, we proposed a grating structure instead of using the regular continuous gold films. We then decreased the thickness of the gold layer from 50 nm (the thickness of the conventional SPR sensor) to 10 nm to increase the field enhancement

of SRSP mode. There is a limit to how much the gold layer can be thinned. In the fabrication process on typical substrates, gold atoms distribute and aggregate in three-dimensional directions and create isolated areas. This leads to a threshold or minimum for the fabrication of Au layers. For SPR sensors, we need to be able to make a continuous layer and not have too much surface roughness. The grating structure, like a prism, also helps to increase the wave vector of the incident light and excite SRSP. Figure 3.14 shows the schematic of the conventional system and the proposed structure.

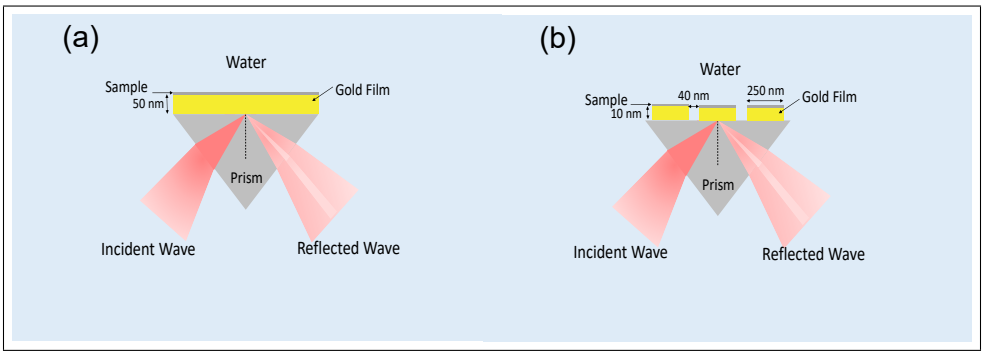

Figure 3.14: (a) Prism coupled SPR structure for 50 nm gold film (b) Modified structure for 10 nm gold film using a grating.

Figure 3.15 shows the dispersion curve of surface plasmon, the light in a prism, and the light in water. This figure shows that in our design, SRSP has been excited at the interface of the gold and water because the light line in the water cut the SRSP curve.

We then plotted the reflection with respect to the incident angle to find the proper incident angle for coupling and reflection dip. Figure 3.16 shows that the proper incident angle for the structure is 73°.

Eq. 3.2 and 3.3 have been used to calculate the period of the structure to match the wave vector of light in the prism to that of the SRSP.

$$k_{\text{prism}} + K_G = \beta \tag{3.2}$$

where:

$$K_G = \frac{2\pi}{\Lambda} \tag{3.3}$$

with Λ being the grating period and β is the propagation constant of the SRSP. This gives a period of 636 nm. However, the coupling is low for this period and gives only

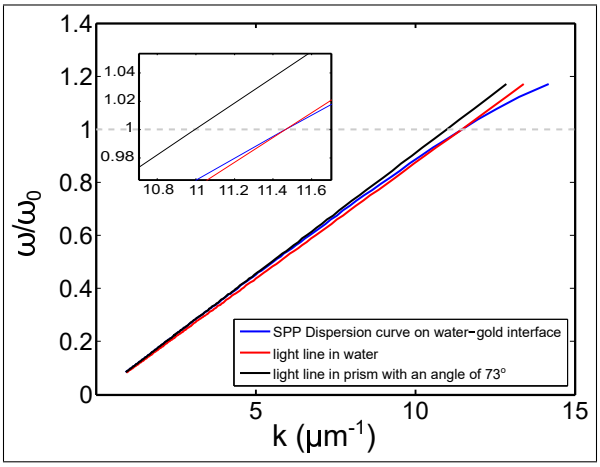

Figure 3.15: Dispersion for coupling to surface plasmon at water-gold interface when incident from glass-gold side of the prism. The intersection point is at 73°, which gives a dip due to losses in the SPP.

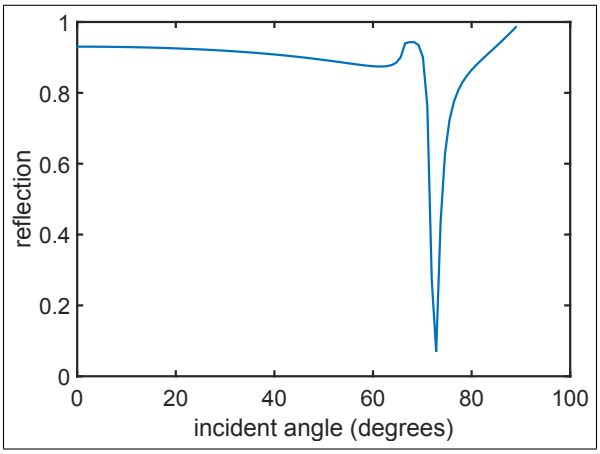

Figure 3.16: Reflection from a 50 nm thick gold film on glass with a water top layer for different incident angles.

a 30 % dip in the reflection. As a result, we tried tuning the period to excite LSPs in the structure as well. Rigours coupled-wave analysis was used to study periodic LSP structures. Figure 3.17 shows the reflection spectra of a periodic structure supporting the SRSP mode with an incidence angle of 73° for different period and gap sizes. The period of 250nm with a gap size of 40 nm was chosen to have a dip in the reflection at 760nm, which is the commercial SPR sensor wavelength. The simulation results that show this dip in the reflection comes from localized surface plasmon are provided in Appendix C.

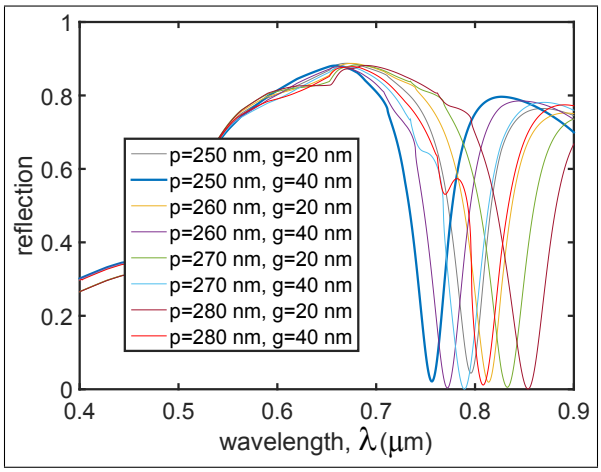

Figure 3.17: Reflection spectra periodic structure supporting SRSP mode with an incidence angle of 73°. The period, p, and gap g were varied in each curve to find the case which is most closely matched to the operating wavelength of 760 nm.

In the last step, we calculated the sensitivity and resolution of the sensor. The sensitivity of a SPR sensor is defined by the ratio of the change in the location of the reflection dip with respect to the incident angle caused by the change in the refractive index of the analyte layer. A 1 nm adlayer is used at the top of the gold with a refractive index of 1.5 for both the conventional system and the proposed structure to see the changes in the reflection dip. We chose this refractive index because biomaterials like proteins (hydrocarbons) have refractive index around 1.5. Figure 3.18 shows that for the proposed structure, the observed change in the incident angle is 3.3 times greater than the conventional system. That means, with the same change in the refractive index of the top layer, the incident angle change is more detectable. The reflection curve of the proposed structure is broader than the conventional system due to the lossy nature of the SRSP mode.

Some researchers believe that a narrower peak gives more information about the

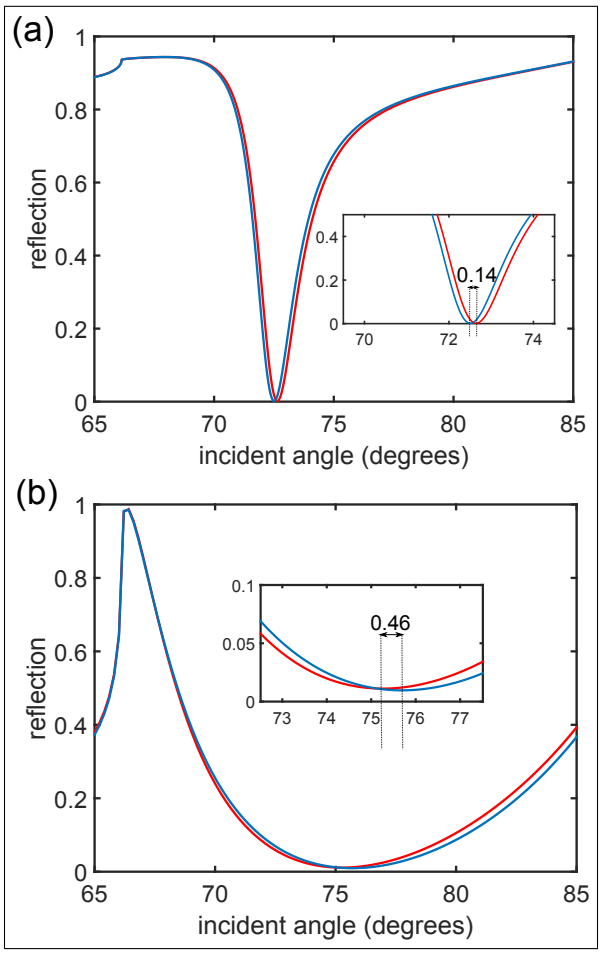

Figure 3.18: Sensitivity calculations for (a) a 50 nm thick gold film with a 1 nm adlayer, and (b) a 10 nm thick gold film with 250 nm period and 210 nm length of each gold segment and a 1 nm adlayer. The insets are shown to clearly depict the angle shifts with the adlayer in each case.

changes in the incident angle. We believe that this is not true because, in the extreme scenario where the width of the peak is less than one pixel spacing of the detector array, no change in the output signal will be detected. As a result, an extremely narrow peak may not provide any information at all. To prove this idea, we did resolution calculations for both structures. The resolution of an SPR sensor is the smallest change in the refractive index of the adlayer that produces a detectable change in the incident angle while considering the noise of the system. Here we added the shot noise, which is proportional to the square root of the detected counts. We used the random function in the MATLAB code to use random values for the added noise. The results show that the resolution of the proposed sensor is four times improved. This improvement is in fact because of the broader peak, which helps the signal use a larger number of bins. As a result, the noise in individual bins may be averaged to lower total noise.

3.4 Accessible High-Performance Double Nanohole Tweezers (Appendix D)

The usual way to find double nanoholes on a gold sample for trapping is to use a scanning electron microscope (SEM) image. This method is fast and accurate in finding DNHs, but the problem is that it is not time and cost-effective. During our work on UCNC trapping, we realized that the brightness of different types of holes, like single holes, double holes, and triangular holes, in CCD (charge-coupled device) camera images is different. So, one can recognize a double nanohole by comparing the brightness of the holes on the CCD camera. The other important parameter that could help to find a DNH was to see more changes in the transmission signal (detected by the APD (Avalanche photodiode)) with changes in the polarization of the incident light. A halfwave plate placed after the laser in the setup was used to change the polarization of the laser beam. These two factors brought an idea to our minds to investigate the effect of these two parameters in finding double nanoholes. For this aim, nanoapertures in gold on glass substrates were fabricated by using the colloidal lithography method introduced in chapter 2. Then, to find a DNH, a combination of CCD camera images and polarization-dependent transmission of the laser beam was used.

The changes in the transmitted signal in the avalanche photodiode (APD) by changing the polarization on the different holes with different brightness are shown in Figure 3.19. Figure 3.19.(a) to (d) show the different brightness of single, double, triangular, and diamond-shaped nanoholes. Figure 3.19.(e) to (h) shows the difference in the polarization dependence of the corresponding holes. It is clear that DNH apertures show more changes with the change in the polarization in comparison with single and triangular holes. The polarization dependence of the DNH structure seems identical to that of the diamond configurations. The reason is that the polarization dependence is as strong as the aperture structure is stretched. The transmission is higher for diamond clusters than for DNHs because the aperture in the gold is larger for the first one. However, the difference in the brightness of these two types of holes helps to easily distinguish them. Therefore, a double nanohole can be chosen without having the SEM image.

In another attempt, we investigated the effect of the orientation of the holes on the polarization. Figure 3.20 and Figure 3.21 show the transmission through a DNH and a triangular aperture by rotating the half-wave plate (HWP) in front of the laser.

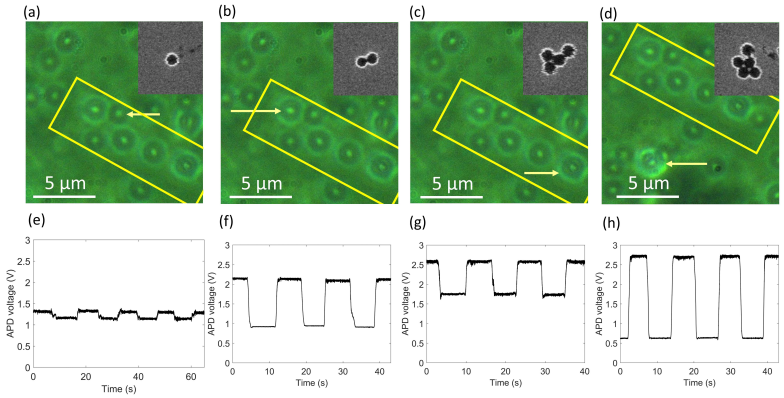

Figure 3.19: Identifying DNHs and other nanohole configurations on a sample. (a-d) CCD images of white light transmission of single, double, and varying cluster apertures. In these images, the same area was artificially marked with yellow contours and an aperture of interest was shown with a yellow array. The brightness of apertures were varying depending on nanoholes configuration: (a) single nanoholes (SNHs) were the dimmest structures, (b) DNHs were brighter than SNHs but dimmer than clusters, (c and d) clusters were the brightest apertures among varying configurations. Inset of figures (a-d) show SEM images of the marked nanoaperture (full SEM image is shown in Supplement 1. (e-h) Maximum and minimum polarization dependence of the laser transmission of an aperture of interest, marked in (a) to (d) and measured with the APD: (e) polarization dependence of the SNH shown in (a) using 4.1 mW. (f) Polarization dependence of the DNH shown in (b) using 4.1 mW incident laser. (g and h) Polarization dependence of the clusters shown in (c) and (d), using 4.1 mW and 6.8 mW. The HWP was switched between maximum and minimum transmission values in the plots (e-h)

The polarization dependence of the DNH is clear. However, the triangular aperture does not show too much changes with the polarization.

To verify our experimental results, we used FDTD simulation. Figure 3.22 verifies that the transmission shows negligible polarization dependence for a triangular aperture. Figure 3.22 shows more changes to the triangular aperture for one of the orientations, while this cannot be seen in the FDTD simulation. The reason is that in the FDTD simulation, we have imported the SEM image of one of the triangular apertures. Because the size of the aperture varies around an average size, there is a slight difference in the size of the measured apertures. Furthermore, the transmission of the apertures is dependent on the curvature of the apertures, which can be different for different apertures. Therefore, based on the size and curvature of the aperture, the polarization dependence can be different for different triangular apertures, but

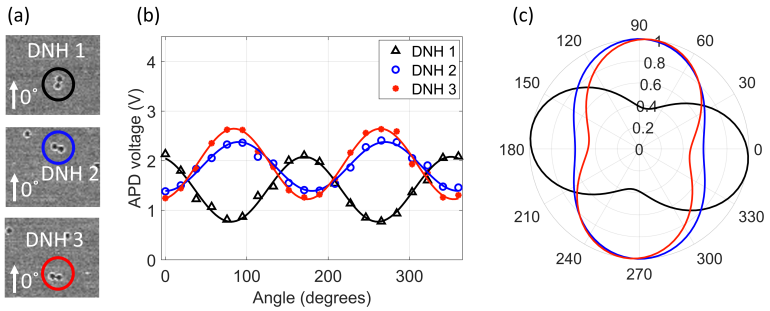

Figure 3.20: Polarization dependence of the laser transmission of DNHs. (a) SEM images of DNHs with their axes normal or parallel in respect to each other. Full SEM image is shown in Supplement 1. (b) Parallel DNHs show similar polarization dependence of the laser transmission and DNHs with normal axes in respect to each other show opposite transmission response of the laser beam. The laser polarization direction was rotated by using an HWP in front of the last output, starting from the zero-order line of the HWP. (c) Polar plots of normalized transmissions for DNHs shown in (a and b).

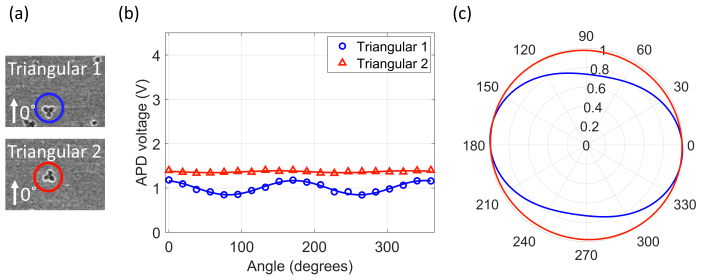

Figure 3.21: Polarization dependence of triangular clusters with different orientation. (a) SEM images of two triangular clusters (labeled as Triangular 1 and Triangular 2) on a sample. (b) Polarization dependence of transmission through the aperture was obtained by rotating the HWP in front of the laser and measured the transmission signal in the APD. (c) Polar plot of the normalized transmission signals shown in (b).

still the changes are far less than the changes seen in the DNH.

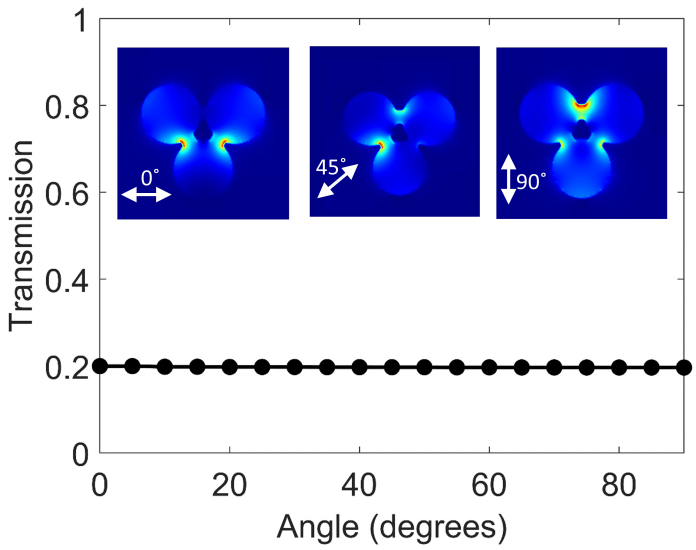

Figure 3.22: The transmission for varying the polarization angle of the incident beam for a triangular structure, obtained by FDTD simulations. The triangular structure showed negligible polarization dependence. The insets show the electric field distribution of the triangular structure for 0°, 45°, and 90° directions of the incident electric field. Triangle nanostructure was simulated with the same dimensions as Triangular 1 in Figure 4 of the main text.

Chapter 4

Conclusions and Future Works

4.1 Conclusions

In this dissertation, the interaction of light and matter in nanostructures has been analyzed and employed to design sensors and trap and manipulate UCNCs.

In the first project, we developed a method that uses single mode matching theory to calculate the reflection phase at the end face of a plasmonic MIM structure. We showed that the correct calculation of the reflection phase is a key factor for the correct calculation of plasmon resonances. The results have been compared with the experimental results and FDTD simulation results. In the calculation of the reflection phase, we considered the real loss of metal by considering the imaginary part of the relative permittivity of the metal. In using single mode matching theory, we used the unconjugated form of the orthogonality relation, which is the proper form rather than the conjugated form because it isolates each mode and gives zero values to different modes. These two significant factors have never been put together for the calculation of the reflection phase. SPP dispersion and scattering must be taken into account while designing a plasmonic device to operate at a specific wavelength. For this reason, it is noteworthy to have a clear understanding of the calculation of plasmonic wavelength. However, in our calculations, we ignored the effect of evanescent waves because they do not transfer energy when the length of the cavity is long enough. But this affects the dispersion relation of the cavity as well. So, the remaining challenge to have a precise calculation of the reflection phase is to consider the effect of these waves in the calculations.

In the second project, we have tuned the geometry of DNH apertures to increase

the enhancement of upconversion nanocrystals by approximately 50x over rectangular apertures, allowing us to observe emission at 400 nm and 1550 nm. These results show that changing the cusp separation of the DNH aperture by varying the plasma etching time with the colloidal lithography method can have a significant effect on emission enhancement. Using the best aperture found in the last step, discrete levels of the emission at 1550 have been observed, showing a path for getting a single photon at 1550 nm for quantum technologies. Using the discrete levels, we can find the emission levels of the single emitters, but the probability of having a single Er in a discrete level was only 30%. Therefore, it is important to attach the single emitters at the cusp of DNHs. In that case, by exciting the attached single emitter in the cusp and connecting the optical setup to a single photon detector, a stable single photon source can be achieved. One technique to isolate single emitters in the cusp is to excite the emitter with UV light after trapping. However, attaching the particle to the cusp of the DNHs is challenging due to the particle movement around the cusp caused by small movements in the optical setup and changes in the temperature. From the experimental view, the alignment of the single-mode fibre connected to the spectrometer is also challenging because the single-mode fibre has a smaller radius than the multimode fibre, and the counts at 1550 nm are also much lower than visible wavelengths. If the alignment is not perfect, it would be hard to see the emission from a single emitter.

In the third project, for the purpose of designing an SPR sensor that is compatible with standard commercial SPR sensors, we suggest a periodic SRSP structure. This is accomplished by coupling the SRSP resonance of a rectangular grating structure to the LSP resonance. The results show 3.3 times higher surface sensitivity, which is promising for high-performance detection applications. Because of the higher loss of SRSPs, the reflection curve of the sensor is much broader than that of conventional sensors. We believe that this broader curve helps to improve the sensitivity because it uses more pixels to show the change in the sensor output. A narrow peak cannot detect a subpixel-sized shift. To prove this idea, the other main characteristic of a SPR sensor, resolution, is also calculated. A noise analysis shows that the resolution in the proposed SRSP design is also 4 times higher than the normal prism structures. Our work proves the positive effect of using SRSPs in improving the sensitivity of such structures. Using this idea, the different sizes and shapes of grating structures can be examined to develop the performance of the SPR sensor even more.

The final project demonstrates a method for determining the position and orien-

tation of DNHs in a gold film that does not require the use of SEM or other complex methods. We could find DNHs in a gold film by just using the brightness of the holes or, in fact, the transmission of the pump laser through the aperture. The other technique that completes this method and assures us of finding a DNH is to check the polarization dependency of the aperture. DNHs show more dependence on polarization changes. In comparison to the previous technique, this one is simpler because it simply requires an evaporator, and the necessity for time-consuming characterization and registration stages has been avoided. However, the orientation of the hole cannot be determined using this method and needs further investigation.

Bibliography

[1] RS Anwar, H Ning, and L Mao. Recent advancements in surface plasmon polaritons-plasmonics in subwavelength structures in microwave and terahertz regimes. *Digital Communications and Networks*, 4(4):244–257, 2018.

[2] SA Maier et al. *Plasmonics: fundamentals and applications*, volume 1. Springer, 2007.

[3] JT Hastings, J Guo, PD Keathley, PB Kumaresh, Y Wei, S Law, and LG Bachas. Optimal self-referenced sensing using long-and short-range surface plasmons. *Optics Express*, 15(26):17661–17672, 2007.

[4] CJ Alleyne, AG Kirk, RC McPhedran, NP Nicorovici, and D Maystre. Enhanced spr sensitivity using periodic metallic structures. *Optics Express*, 15(13):8163–8169, 2007.

[5] JF Suyver, J Grimm, MK Van Veen, D Biner, KW Krämer, and HU Güdel. Upconversion spectroscopy and properties of nayf4 doped with er3+, tm3+ and/or yb3+. *Journal of Luminescence*, 117(1):1–12, 2006.

[6] A Kotnala. *Double Nanohole Optical Tweezer for Single Molecule and Nanoparticle Analysis*. PhD thesis, 2015.

[7] ML Juan, R Gordon, Y Pang, F Eftekhari, and R Quidant. Self-induced back-action optical trapping of dielectric nanoparticles. *Nature Physics*, 5(12):915–919, 2009.

[8] J Berthelot, SS Aćimović, ML Juan, MP Kreuzer, J Renger, and R Quidant. Three-dimensional manipulation with scanning near-field optical nanotweezers. *Nature Nanotechnology*, 9(4):295–299, 2014.

[9] A Kotnala and R Gordon. Double nanohole optical tweezers visualize protein p53 suppressing unzipping of single dna-hairpins. *Biomedical Optics Express*, 5(6):1886–1894, 2014.

[10] A Alizadehkhaledi, AL Frencken, MK Dezfouli, S Hughes, F CJM van Veggel, and R Gordon. Cascaded plasmon-enhanced emission from a single upconverting nanocrystal. *ACS Photonics*, 6(5):1125–1131, 2019.

[11] Z Sharifi, M Dobinson, G Hajisalem, MS Shariatdoust, AL Frencken, F CJM van Veggel, and R Gordon. Isolating and enhancing single-photon emitters for 1550 nm quantum light sources using double nanohole optical tweezers. *The Journal of Chemical Physics*, 154(18):184204, 2021.

[12] MJ Levene, J Korlach, SW Turner, M Foquet, HG Craighead, and WW Webb. Zero-mode waveguides for single-molecule analysis at high concentrations. *Science*, 299(5607):682–686, 2003.

[13] Henri J Lezec, A Degiron, E Devaux, RA Linke, L Martin-Moreno, FJ Garcia-Vidal, and TW Ebbesen. Beaming light from a subwavelength aperture. *Science*, 297(5582):820–822, 2002.

[14] AL Ravindranath, MS Shariatdoust, S Mathew, and R Gordon. Colloidal lithography double-nanohole optical trapping of nanoparticles and proteins. *Optics Express*, 27(11):16184–16194, 2019.

[15] M Dragoman and D Dragoman. Plasmonics: Applications to nanoscale terahertz and optical devices. *Progress in Quantum Electronics*, 32(1):1–41, 2008.

[16] A Khademi, T Dewolf, and R Gordon. Quantum plasmonic epsilon near zero: field enhancement and cloaking. *Optics Express*, 26(12):15656–15664, 2018.

[17] SA Maier, ML Brongersma, PG Kik, S Meltzer, A AG Requicha, and HA Atwater. Plasmonics—a route to nanoscale optical devices. *Advanced Materials*, 13(19):1501–1505, 2001.

[18] S Nie and SR Emory. Probing single molecules and single nanoparticles by surface-enhanced raman scattering. *Science*, 275(5303):1102–1106, 1997.

[19] K Kneipp, Y Wang, H Kneipp, LT Perelman, I Itzkan, RR Dasari, and MS Feld. Single molecule detection using surface-enhanced raman scattering (sers). *Physical Review Letters*, 78(9):1667, 1997.

[20] Y Cai, Y Li, P Nordlander, and PS Cremer. Fabrication of elliptical nanorings with highly tunable and multiple plasmonic resonances. *Nano Letters*, 12(9):4881–4888, 2012.

[21] H Raether. Surface plasmons on smooth surfaces. *Surface Plasmons on Smooth and Rough Surfaces and on Gratings*, pages 4–39, 1988.

[22] JF O'Hara, RD Averitt, and AJ Taylor. Prism coupling to terahertz surface plasmon polaritons. *Optics Express*, 13(16):6117–6126, 2005.

[23] J Saxler, J Gómez Rivas, C Janke, HPM Pellemans, P Haring Bolivar, and H Kurz. Time-domain measurements of surface plasmon polaritons in the terahertz frequency range. *Physical Review B*, 69(15):155427, 2004.

[24] X Shou, A Agrawal, and A Nahata. Role of metal film thickness on the enhanced transmission properties of a periodic array of subwavelength apertures. *Optics Express*, 13(24):9834–9840, 2005.

[25] E Babaei, Z Sharifi, and R Gordon. Improving sensitivity of existing surface plasmon resonance systems with grating-coupled short-range surface plasmons. *JOSA B*, 36(8):F144–F148, 2019.

[26] Y Chen and H Ming. Review of surface plasmon resonance and localized surface plasmon resonance sensor. *Photonic Sensors*, 2(1):37–49, 2012.

[27] CY Chen and E Burstein. Giant raman scattering by molecules at metal-island films. *Physical Review Letters*, 45(15):1287, 1980.

[28] K Sokolov, G Chumanov, and TM Cotton. Enhancement of molecular fluorescence near the surface of colloidal metal films. *Analytical Chemistry*, 70(18):3898–3905, 1998.

[29] R Karlsson and A Fält. Experimental design for kinetic analysis of protein-protein interactions with surface plasmon resonance biosensors. *Journal of Immunological Methods*, 200(1-2):121–133, 1997.

[30] P Neutens, P Van Dorpe, I De Vlaminck, L Lagae, and G Borghs. Electrical detection of confined gap plasmons in metal–insulator–metal waveguides. *Nature Photonics*, 3(5):283–286, 2009.

[31] RF Oulton, VJ Sorger, DA Genov, DFP Pile, and X Zhang. A hybrid plasmonic waveguide for subwavelength confinement and long-range propagation. *Nature Photonics*, 2(8):496–500, 2008.

[32] Z Li, F Hao, Y Huang, Y Fang, P Nordlander, and H Xu. Directional light emission from propagating surface plasmons of silver nanowires. *Nano Letters*, 9(12):4383–4386, 2009.

[33] E Verhagen, L Kuipers, and A Polman. Enhanced nonlinear optical effects with a tapered plasmonic waveguide. *Nano Letters*, 7(2):334–337, 2007.

[34] SM Hashemi Rafsanjani, T Cheng, S Mittler, and C Rangan. Theoretical proposal for a biosensing approach based on a linear array of immobilized gold nanoparticles. *Journal of Applied Physics*, 107(9):094303, 2010.

[35] A Lahav, M Auslender, and I Abdulhalim. Sensitivity enhancement of guided-wave surface-plasmon resonance sensors. *Optics Letters*, 33(21):2539–2541, 2008.

[36] SA Maier, PG Kik, HA Atwater, S Meltzer, E Harel, BE Koel, and Ari AG Requicha. Local detection of electromagnetic energy transport below the diffraction limit in metal nanoparticle plasmon waveguides. *Nature Materials*, 2(4):229–232, 2003.

[37] J Grandidier, GC Des Francs, S Massenot, A Bouhelier, L Markey, JC Weeber, C Finot, and A Dereux. Gain-assisted propagation in a plasmonic waveguide at telecom wavelength. *Nano Letters*, 9(8):2935–2939, 2009.

[38] WA Murray, JR Suckling, and WL Barnes. Overlayers on silver nanotriangles: field confinement and spectral position of localized surface plasmon resonances. *Nano Letters*, 6(8):1772–1777, 2006.

[39] Y Guan, Z Xue, J Liang, Z Huang, and W Yang. One-pot synthesis of size-tunable hollow gold nanoshells via aptes-in-water suspension. *Colloids and Surfaces A: Physicochemical and Engineering Aspects*, 502:6–12, 2016.

[40] LJ Sherry, SH Chang, GC Schatz, RP Van Duyne, BJ Wiley, and Y Xia. Localized surface plasmon resonance spectroscopy of single silver nanocubes. *Nano Letters*, 5(10):2034–2038, 2005.

[41] N Engheta, A Salandrino, and A Alu. Circuit elements at optical frequencies: nanoinductors, nanocapacitors, and nanoresistors. *Physical Review Letters*, 95(9):095504, 2005.

[42] K Imura, T Nagahara, and H Okamoto. Plasmon mode imaging of single gold nanorods. *Journal of the American Chemical Society*, 126(40):12730–12731, 2004.

[43] K Imura, T Nagahara, and H Okamoto. Near-field optical imaging of plasmon modes in gold nanorods. *The Journal of Chemical Physics*, 122(15):154701, 2005.

[44] H Ditlbacher, A Hohenau, D Wagner, U Kreibig, M Rogers, F Hofer, FR Aussenegg, and J Krenn. Silver nanowires as surface plasmon resonators. *Physical Review Letters*, 95(25):257403, 2005.

[45] T Laroche and C Girard. Near-field optical properties of single plasmonic nanowires. *Applied Physics Letters*, 89(23):233119, 2006.

[46] F Neubrech, T Kolb, R Lovrincic, G Fahsold, A Pucci, J Aizpurua, TW Cornelius, ME Toimil-Molares, R Neumann, and S Karim. Resonances of individual metal nanowires in the infrared. *Applied Physics Letters*, 89(25):253104, 2006.

[47] J Takahara, S Yamagishi, H Taki, A Morimoto, and T Kobayashi. Guiding of a one-dimensional optical beam with nanometer diameter. *Optics Letters*, 22(7):475–477, 1997.

[48] T Søndergaard and SI Bozhevolnyi. Metal nano-strip optical resonators. *Optics Express*, 15(7):4198–4204, 2007.

[49] SI Bozhevolnyi and T Søndergaard. General properties of slow-plasmon resonant nanostructures: nano-antennas and resonators. *Optics Express*, 15(17):10869–10877, 2007.

[50] T Søndergaard, J Beermann, A Boltasseva, and SI Bozhevolnyi. Slow-plasmon resonant-nanostrip antennas: Analysis and demonstration. *Physical Review B*, 77(11):115420, 2008.

[51] G Della Valle, T Søndergaard, and SI Bozhevolnyi. Plasmon-polariton nanostrip resonators: from visible to infra-red. *Optics Express*, 16(10):6867–6876, 2008.

[52] E Kretschmann and H Raether. Radiative decay of non radiative surface plasmons excited by light. *Zeitschrift für Naturforschung A*, 23(12):2135–2136, 1968.

[53] J Backlund, J Bengtsson, C-F Carlstrom, and A Larsson. Multifunctional grating couplers for bidirectional incoupling into planar waveguides. *IEEE Photonics Technology Letters*, 12(3):314–316, 2000.

[54] K Kintaka, J Nishii, J Ohmori, Y Imaoka, M Nishihara, S Ura, R Satoh, and H Nishihara. Integrated waveguide gratings for wavelength-demultiplexing of free space waves from guided waves. *Optics Express*, 12(14):3072–3078, 2004.

[55] Z Zhu and TG Brown. Nonperturbative analysis of cross coupling in corrugated metal films. *JOSA A*, 17(10):1798–1806, 2000.

[56] WL Barnes, TW Preist, SC Kitson, and JR Sambles. Physical origin of photonic energy gaps in the propagation of surface plasmons on gratings. *Physical Review B*, 54(9):6227, 1996.

[57] M Masale. The theory of attenuated total reflection by surface polaritons on one-sided corrugated thin films. *Physica B: Condensed Matter*, 325:385–393, 2003.

[58] J Homola. Electromagnetic theory of surface plasmons. In *Surface plasmon resonance based sensors*, pages 3–44. Springer, 2006.

[59] MJ Jory, PS Vukusic, and JR Sambles. Development of a prototype gas sensor using surface plasmon resonance on gratings. *Sensors and Actuators B: Chemical*, 17(3):203–209, 1994.

[60] U Schröter and D Heitmann. Grating couplers for surface plasmons excited on thin metal films in the kretschmann-raether configuration. *Physical Review B*, 60(7):4992, 1999.

[61] SI Bozhevolnyi, J Erland, K Leosson, P MW Skovgaard, and JM Hvam. Waveguiding in surface plasmon polariton band gap structures. *Physical Review Letters*, 86(14):3008, 2001.

[62] SI Bozhevolnyi, VS Volkov, K Leosson, and A Boltasseva. Bend loss in surface plasmon polariton band-gap structures. *Applied Physics Letters*, 79(8):1076–1078, 2001.

[63] SC Kitson, William L Barnes, and JR Sambles. Full photonic band gap for surface modes in the visible. *Physical Review Letters*, 77(13):2670, 1996.

[64] J Homola. Surface plasmon resonance sensors for detection of chemical and biological species. *Chemical Reviews*, 108(2):462–493, 2008.

[65] R Scheps. Upconversion laser processes. *Progress in Quantum Electronics*, 20(4):271–358, 1996.

[66] G Chen, H Qiu, PN Prasad, and X Chen. Upconversion nanoparticles: design, nanochemistry, and applications in theranostics. *Chemical Reviews*, 114(10):5161–5214, 2014.

[67] X Huang, S Han, W Huang, and X Liu. Enhancing solar cell efficiency: the search for luminescent materials as spectral converters. *Chemical Society Reviews*, 42(1):173–201, 2013.

[68] DJ Gargas, EM Chan, AD Ostrowski, S Aloni, M Virginia P Altoe, ES Barnard, B Sanii, JJ Urban, DJ Milliron, BE Cohen, et al. Engineering bright sub-10-nm upconverting nanocrystals for single-molecule imaging. *Nature Nanotechnology*, 9(4):300–305, 2014.

[69] MV Padalkar and N Pleshko. Wavelength-dependent penetration depth of near infrared radiation into cartilage. *Analyst*, 140(7):2093–2100, 2015.

[70] S Wu and journal=Advanced Materials volume=28 number=6 pages=1208–1226 year=2016 publisher=Wiley Online Library Butt, HJ. Near-infrared-sensitive materials based on upconverting nanoparticles.

[71] P Juzenas, A Juzeniene, O Kaalhus, V Iani, and J Moan. Noninvasive fluorescence excitation spectroscopy during application of 5-aminolevulinic acid in vivo. *Photochemical & Photobiological Sciences*, 1(10):745–748, 2002.

[72] JPC Do Nascimento, AJM Sales, DG Sousa, MAS Da Silva, SGC Moreira, K Pavani, MJ Soares, MPF Graça, J Suresh Kumar, and ASB Sombra. Temperature-, power-, and concentration-dependent two and three photon upconversion in er 3+/yb 3+ co-doped lanthanum ortho-niobate phosphors. *RSC Advances*, 6(72):68160–68169, 2016.

[73] D Yin, S Peng, Y Qi, S Zheng, Y Zhou, and X Wang. Enhancement of the 1.53 μm fluorescence and energy transfer in er3+/yb3+/ce3+ tri-doped wo3 modified tellurite-based glass. *Journal of Alloys and Compounds*, 581:534–541, 2013.

[74] J Zhang and J Heo. 980 nm upconversion luminescence from oxy-fluoride glasses and glass-ceramics doped with yb3+ and er3+ ions. *Journal of Non-crystalline Solids*, 383:188–191, 2014.

[75] Y Guo, L Zhang, L Hu, NK Chen, and J Zhang. Er3+ ions doped bismuthate glasses sensitized by yb3+ ions for highly efficient 2.7 μm laser applications. *Journal of Luminescence*, 138:209–213, 2013.

[76] F Huang, X Liu, W Li, L Hu, and D Chen. Energy transfer mechanism in er3+ doped fluoride glass sensitized by tm3+ or ho3+ for 2.7-\mu m emission. *Chinese Optics Letters*, 12(5):051601, 2014.

[77] F Huang, X Liu, Y Ma, S Kang, L Hu, and D Chen. Origin of near to middle infrared luminescence and energy transfer process of er3+/yb3+ co-doped fluorotellurite glasses under different excitations. *Scientific Reports*, 5(1):1–6, 2015.

[78] X Li, X Liu, L Zhang, L Hu, and J Zhang. Emission enhancement in er3+/pr3+-codoped germanate glasses and their use as a 2.7-mm laser material. *Chinese Optics Letters*, 11(12):121601–121601, 2013.

[79] B Yao, X Liu, X Yu, X Duan, Y Ju, and Y Wang. Resonantly pumped q-switched er: Gdvo 4 laser. *Chinese Optics Letters*, 11(3):031405, 2013.

[80] I Arul Rayappan and K Marimuthu. Structural and luminescence behavior of the er3+ doped alkali fluoroborate glasses. *Journal of Non-crystalline Solids*, 367:43–50, 2013.

[81] VG Artioushenko, NI Afanasyeva, AA Lerman, AP Kryukov, EF Kuzin, NN Zharkova, VG Plotnichenko, GA Frank, GI Didenko, VV Sokolov, et al. Medical applications of mir-fiber spectroscopic probes. In *Biochemical and Medical Sensors*, volume 2085, pages 137–142. International Society for Optics and Photonics, 1994.

[82] B DO Richards, A Jha, G Jose, T Teddy-Fernandez, D Binks, and Y Tsang. Tellurite glass as a solid-state mid-infrared laser host material. In *Mid-Infrared Coherent Sources*, pages MW1C–7. Optical Society of America, 2013.

[83] S Li, P Wang, H Xia, J Peng, L Tang, Y Zhang, and H Jiang. Tm3+ and nd3+ singly doped liyf4 single crystals with 3-5\mu m mid-infrared luminescence. *Chinese Optics Letters*, 12(2):021601, 2014.

[84] DM Wu, A García-Etxarri, A Salleo, and JA Dionne. Plasmon-enhanced upconversion. *The journal of Physical Chemistry Letters*, 5(22):4020–4031, 2014.

[85] AM Dibos, M Raha, CM Phenicie, and JD Thompson. Atomic source of single photons in the telecom band. *Physical Review Letters*, 120(24):243601, 2018.

[86] T Zhong, JM Kindem, JG Bartholomew, J Rochman, I Craiciu, V Verma, SW Nam, F Marsili, MD Shaw, AD Beyer, et al. Optically addressing single rare-earth ions in a nanophotonic cavity. *Physical Review Letters*, 121(18):183603, 2018.

[87] L Novotny and N Van Hulst. Antennas for light. *Nature Photonics*, 5(2):83–90, 2011.

[88] V Giannini, AI Fernández-Domínguez, SC Heck, and SA Maier. Plasmonic nanoantennas: fundamentals and their use in controlling the radiative properties of nanoemitters. *Chemical Reviews*, 111(6):3888–3912, 2011.

[89] M Pelton, J Aizpurua, and G Bryant. Metal-nanoparticle plasmonics. *Laser & Photonics Reviews*, 2(3):136–159, 2008.

[90] T Utikal, E Eichhammer, L Petersen, A Renn, S Götzinger, and V Sandoghdar. Spectroscopic detection and state preparation of a single praseodymium ion in a crystal. *Nature Communications*, 5(1):1–8, 2014.

[91] I Nakamura, T Yoshihiro, H Inagawa, S Fujiyoshi, and M Matsushita. Spectroscopy of single pr3+ ion in laf3 crystal at 1.5 k. *Scientific Reports*, 4(1):1–6, 2014.

[92] E Eichhammer, T Utikal, S Götzinger, and V Sandoghdar. Spectroscopic detection of single pr3+ ions on the 3h4- 1d2 transition. *New Journal of Physics*, 17(8):083018, 2015.

[93] R Kolesov, K Xia, R Reuter, M Jamali, R Stöhr, T Inal, P Siyushev, and J Wrachtrup. Mapping spin coherence of a single rare-earth ion in a crystal onto a single photon polarization state. *Physical Review Letters*, 111(12):120502, 2013.

[94] P Siyushev, K Xia, R Reuter, M Jamali, N Zhao, N Yang, C Duan, N Kukharchyk, AD Wieck, R Kolesov, et al. Coherent properties of single rare-earth spin qubits. *Nature Communications*, 5(1):1–6, 2014.

[95] K Xia, R Kolesov, Y Wang, P Siyushev, R Reuter, T Kornher, N Kukharchyk, AD Wieck, B Villa, S Yang, et al. All-optical preparation of coherent dark states of a single rare earth ion spin in a crystal. *Physical Review Letters*, 115(9):093602, 2015.

[96] C Yin, M Rancic, GG de Boo, N Stavrias, JC McCallum, MJ Sellars, and S Rogge. Optical addressing of an individual erbium ion in silicon. *Nature*, 497(7447):91–94, 2013.

[97] JCG Bünzli and C Piguet. Taking advantage of luminescent lanthanide ions. *Chemical Society Reviews*, 34(12):1048–1077, 2005.

[98] ID Hughes, M Däne, A Ernst, W Hergert, M Lüders, J Poulter, JB Staunton, A Svane, Z Szotek, and WM Temmerman. Lanthanide contraction and magnetism in the heavy rare earth elements. *Nature*, 446(7136):650–653, 2007.

[99] C O'Brien, T Zhong, A Faraon, and C Simon. Nondestructive photon detection using a single rare-earth ion coupled to a photonic cavity. *Physical Review A*, 94(4):043807, 2016.

[100] C Lopez, A Trimeche, D Comparat, and YJ Picard. Real-time trajectory control of deterministically produced ions. *Physical Review Applied*, 11(6):064049, 2019.

[101] R Kolesov, K Xia, R Reuter, R Stöhr, A Zappe, J Meijer, PR Hemmer, and J Wrachtrup. Optical detection of a single rare-earth ion in a crystal. *Nature Communications*, 3(1):1–7, 2012.

[102] K Groot-Berning, T Kornher, G Jacob, F Stopp, ST Dawkins, R Kolesov, J Wrachtrup, K Singer, and F Schmidt-Kaler. Deterministic single-ion implantation of rare-earth ions for nanometer-resolution color-center generation. *Physical Review Letters*, 123(10):106802, 2019.

[103] A Alizadehkhaledi, AL Frencken, F CJM van Veggel, and R Gordon. Isolating nanocrystals with an individual erbium emitter: A route to a stable single-photon source at 1550 nm wavelength. *Nano Letters*, 20(2):1018–1022, 2019.

[104] JT Choy, B JM Hausmann, TM Babinec, I Bulu, M Khan, P Maletinsky, A Yacoby, and M Lončar. Enhanced single-photon emission from a diamond–silver aperture. *Nature Photonics*, 5(12):738–743, 2011.

[105] JC Maxwell. Viii. a dynamical theory of the electromagnetic field. *Philosophical Transactions of the Royal Society of London*, (155):459–512, 1865.

[106] JC Maxwell. *A treatise on electricity and magnetism*, volume 1. Clarendon press, 1873.

[107] A Ashkin. Acceleration and trapping of particles by radiation pressure. *Physical Review Letters*, 24(4):156, 1970.

[108] A Ashkin and JM Dziedzic. Optical levitation by radiation pressure. *Applied Physics Letters*, 19(8):283–285, 1971.

[109] A Ashkin and JM Dziedzic. Optical levitation of liquid drops by radiation pressure. *Science*, 187(4181):1073–1075, 1975.

[110] A Ashkin, JM Dziedzic, JE Bjorkholm, and S Chu. Observation of a single-beam gradient force optical trap for dielectric particles. *Optics Letters*, 11(5):288–290, 1986.

[111] Y Pang and R Gordon. Optical trapping of a single protein. *Nano Letters*, 12(1):402–406, 2012.

[112] Y Harada and T Asakura. Radiation forces on a dielectric sphere in the rayleigh scattering regime. *Optics Communications*, 124(5-6):529–541, 1996.

[113] R Gordon. Nanostructured metals for light-based technologies. *Nanotechnology*, 30(21):212001, 2019.

[114] ES Kwak, TD Onuta, D Amarie, R Potyrailo, B Stein, SC Jacobson, WL Schaich, and B Dragnea. Optical trapping with integrated near-field apertures. *The Journal of Physical Chemistry B*, 108(36):13607–13612, 2004.

[115] A Baev, EP Furlani, PN Prasad, AN Grigorenko, and NW Roberts. Laser nanotrapping and manipulation of nanoscale objects using subwavelength apertured plasmonic media. *Journal of Applied Physics*, 103(8):084316, 2008.

[116] LA Blanco and M Nieto-Vesperinas. Optical forces near subwavelength apertures in metal discs. *Journal of Optics A: Pure and Applied Optics*, 9(8):S235, 2007.

[117] DG Grier. A revolution in optical manipulation. *Nature*, 424(6950):810–816, 2003.

[118] A Ashkin and JM Dziedzic. Optical trapping and manipulation of viruses and bacteria. *Science*, 235(4795):1517–1520, 1987.

[119] K Svoboda, CF Schmidt, D Branton, and SM Block. Conformation and elasticity of the isolated red blood cell membrane skeleton. *Biophysical Journal*, 63(3):784–793, 1992.

[120] SH Mirsadeghi and JF Young. Ultrasensitive diagnostic analysis of au nanoparticles optically trapped in silicon photonic circuits at sub-milliwatt powers. *Nano Letters*, 14(9):5004–5009, 2014.

[121] EX Jin and X Xu. Enhanced optical near field from a bowtie aperture. *Applied Physics Letters*, 88(15):153110, 2006.

[122] RA Jensen, IC Huang, O Chen, JT Choy, TS Bischof, M Loncar, and MG Bawendi. Optical trapping and two-photon excitation of colloidal quantum dots using bowtie apertures. *ACS Photonics*, 3(3):423–427, 2016.

[123] A AE Saleh and JA Dionne. Toward efficient optical trapping of sub-10-nm particles with coaxial plasmonic apertures. *Nano Letters*, 12(11):5581–5586, 2012.

[124] D Yoo, KL Gurunatha, HK Choi, DA Mohr, CT Ertsgaard, R Gordon, and SH Oh. Low-power optical trapping of nanoparticles and proteins with resonant coaxial nanoaperture using 10 nm gap. *Nano Letters*, 18(6):3637–3642, 2018.

[125] M Righini, P Ghenuche, S Cherukulappurath, Viktor Myroshnychenko, Francisco Javier Garcia de Abajo, and Romain Quidant. Nano-optical trapping of rayleigh particles and escherichia coli bacteria with resonant optical antennas. *Nano Letters*, 9(10):3387–3391, 2009.

[126] W Zhang, L Huang, C Santschi, and O JF Martin. Trapping and sensing 10 nm metal nanoparticles using plasmonic dipole antennas. *Nano Letters*, 10(3):1006–1011, 2010.

[127] BJ Roxworthy, KD Ko, A Kumar, KH Fung, E KC Chow, GL Liu, NX Fang, and KC Toussaint Jr. Application of plasmonic bowtie nanoantenna arrays for optical trapping, stacking, and sorting. *Nano Letters*, 12(2):796–801, 2012.

[128] A Lesuffleur, LKS Kumar, and R Gordon. Enhanced second harmonic generation from nanoscale double-hole arrays in a gold film. *Applied Physics Letters*, 88(26):261104, 2006.

[129] LKS Kumar, A Lesuffleur, MC Hughes, and R Gordon. Double nanohole apex-enhanced transmission in metal films. *Applied Physics B*, 84(1):25–28, 2006.

[130] Y Chen, A Kotnala, L Yu, J Zhang, and R Gordon. Wedge and gap plasmonic resonances in double nanoholes. *Optics Express*, 23(23):30227–30236, 2015.

[131] M Mivelle, TS van Zanten, L Neumann, NF van Hulst, and MF Garcia-Parajo. Ultrabright bowtie nanoaperture antenna probes studied by single molecule fluorescence. *Nano Letters*, 12(11):5972–5978, 2012.

[132] UC Fischer and HP Zingsheim. Submicroscopic pattern replication with visible light. *Journal of Vacuum Science and Technology*, 19(4):881–885, 1981.

[133] HW Deckman and JH Dunsmuir. Natural lithography. *Applied Physics Letters*, 41(4):377–379, 1982.

[134] JC Hulteen and RP Van Duyne. Nanosphere lithography: A materials general fabrication process for periodic particle array surfaces. *Journal of Vacuum Science & Technology A: Vacuum, Surfaces, and Films*, 13(3):1553–1558, 1995.

[135] CL Haynes and RP Van Duyne. Nanosphere lithography: a versatile nanofabrication tool for studies of size-dependent nanoparticle optics, 2001.

[136] G Zhang and D Wang. Colloidal lithography—the art of nanochemical patterning. *Chemistry–An Asian Journal*, 4(2):236–245, 2009.

[137] A Plettl, F Enderle, M Saitner, A Manzke, C Pfahler, S Wiedemann, and P Ziemann. Non-close-packed crystals from self-assembled polystyrene spheres by isotropic plasma etching: Adding flexibility to colloid lithography. *Advanced Functional Materials*, 19(20):3279–3284, 2009.

[138] SH Lee, KC Bantz, NC Lindquist, SH Oh, and CL Haynes. Self-assembled plasmonic nanohole arrays. *Langmuir*, 25(23):13685–13693, 2009.

[139] MP Murray-Méthot, M Ratel, and JF Masson. Optical properties of au, ag, and bimetallic au on ag nanohole arrays. *The Journal of Physical Chemistry C*, 114(18):8268–8275, 2010.

[140] JF Masson, MP Murray-Méthot, and LS Live. Nanohole arrays in chemical analysis: manufacturing methods and applications. *Analyst*, 135(7):1483–1489, 2010.

[141] TD Onuta, M Waegele, CC DuFort, WL Schaich, and B Dragnea. Optical field enhancement at cusps between adjacent nanoapertures. *Nano Letters*, 7(3):557–564, 2007.

[142] R Gordon. Light in a subwavelength slit in a metal: propagation and reflection. *Physical Review B*, 73(15):153405, 2006.

[143] A Chandran, ES Barnard, JS White, and ML Brongersma. Metal-dielectric-metal surface plasmon-polariton resonators. *Physical Review B*, 85(8):085416, 2012.

[144] HT Miyazaki and Y Kurokawa. Squeezing visible light waves into a 3-nm-thick and 55-nm-long plasmon cavity. *Physical Review Letters*, 96(9):097401, 2006.

[145] C Chen, ML Juan, Y Li, G Maes, G Borghs, P Van Dorpe, and R Quidant. Enhanced optical trapping and arrangement of nano-objects in a plasmonic nanocavity. *Nano Letters*, 12(1):125–132, 2012.

[146] MU Raza, SSS Peri, LC Ma, SM Iqbal, and G Alexandrakis. Self-induced back action actuated nanopore electrophoresis (sane). *Nanotechnology*, 29(43):435501, 2018.

[147] A Zehtabi-Oskuie, AA Zinck, RM Gelfand, and R Gordon. Template stripped double nanohole in a gold film for nano-optical tweezers. *Nanotechnology*, 25(49):495301, 2014.

[148] E Verhagen, L Kuipers, and A Polman. Field enhancement in metallic subwavelength aperture arrays probed by erbium upconversion luminescence. *Optics Express*, 17(17):14586–14598, 2009.

[149] K Okamoto and S Kawata. Radiation force exerted on subwavelength particles near a nanoaperture. *Physical Review Letters*, 83(22):4534, 1999.

[150] KJ Russell, TL Liu, S Cui, and EL Hu. Large spontaneous emission enhancement in plasmonic nanocavities. *Nature Photonics*, 6(7):459–462, 2012.

[151] JK Yang, CS Kee, and JW Lee. Three-dimensional subwavelength confinement of terahertz electromagnetic surface modes in a coupled slit structure. *Optics Express*, 19(21):20199–20204, 2011.

[152] H Choo, MK Kim, M Staffaroni, TJ Seok, J Bokor, S Cabrini, PJ Schuck, MC Wu, and E Yablonovitch. Nanofocusing in a metal–insulator–metal gap plasmon waveguide with a three-dimensional linear taper. *Nature Photonics*, 6(12):838–844, 2012.

[153] X Chen, HR Park, NC Lindquist, J Shaver, M Pelton, and SH Oh. Squeezing millimeter waves through a single, nanometer-wide, centimeter-long slit. *Scientific Reports*, 4(1):1–5, 2014.

[154] MA Seo, HR Park, SM Koo, DJ Park, JH Kang, OK Suwal, SS Choi, PCM Planken, GS Park, NK Park, et al. Terahertz field enhancement by a metallic nano slit operating beyond the skin-depth limit. *Nature Photonics*, 3(3):152–156, 2009.

[155] OK Suwal, J Rhie, N Kim, and DS Kim. Nonresonant 104 terahertz field enhancement with 5-nm slits. *Scientific Reports*, 7(1):1–7, 2017.

[156] YM Bahk, S Han, J Rhie, J Park, H Jeon, N Park, and DS Kim. Ultimate terahertz field enhancement of single nanoslits. *Physical Review B*, 95(7):075424, 2017.

[157] HT Miyazaki and Y Kurokawa. Controlled plasmon resonance in closed metal/insulator/metal nanocavities. *Applied Physics Letters*, 89(21):211126, 2006.

[158] FJ Garcia-Vidal, E Moreno, JA Porto, and L Martin-Moreno. Transmission of light through a single rectangular hole. *Physical Review Letters*, 95(10):103901, 2005.

[159] JR Suckling, AP Hibbins, MJ Lockyear, TW Preist, JR Sambles, and CR Lawrence. Finite conductance governs the resonance transmission of thin metal slits at microwave frequencies. *Physical Review Letters*, 92(14):147401, 2004.

[160] JS White, G Veronis, Z Yu, ES Barnard, A Chandran, S Fan, and ML Brongersma. Extraordinary optical absorption through subwavelength slits. *Optics Letters*, 34(5):686–688, 2009.

[161] T Ishi, J Fujikata, K Makita, T Baba, and K Ohashi. Si nano-photodiode with a surface plasmon antenna. *Japanese Journal of Applied Physics*, 44(3L):L364, 2005.

[162] S Refki, S Hayashi, A Rahmouni, DV Nesterenko, and Z Sekkat. Anticrossing behavior of surface plasmon polariton dispersions in metal-insulator-metal structures. *Plasmonics*, 11(2):433–440, 2016.

[163] Z Sekkat, S Hayashi, DV Nesterenko, A Rahmouni, S Refki, H Ishitobi, Y Inouye, and S Kawata. Plasmonic coupled modes in metal-dielectric multilayer structures: Fano resonance and giant field enhancement. *Optics Express*, 24(18):20080–20088, 2016.

[164] S Hayashi, DV Nesterenko, A Rahmouni, and Z Sekkat. Polarization effects in light-tunable fano resonance in metal-dielectric multilayer structures. *Physical Review B*, 95(16):165402, 2017.

[165] K Wen, L Yan, W Pan, B Luo, Z Guo, and Y Guo. Transmission characteristics and applications of plasmonic slit waveguide based on metal-insulator-metal structure. *Optical Engineering*, 51(10):104601, 2012.

[166] YC Jun, KCY Huang, and ML Brongersma. Plasmonic beaming and active control over fluorescent emission. *Nature Communications*, 2(1):1–6, 2011.

[167] Y Kurokawa and HT Miyazaki. Metal-insulator-metal plasmon nanocavities: Analysis of optical properties. *Physical Review B*, 75(3):035411, 2007.

[168] NC Lindquist, P Nagpal, KM McPeak, DJ Norris, and SH Oh. Engineering metallic nanostructures for plasmonics and nanophotonics. *Reports on Progress in Physics*, 75(3):036501, 2012.

[169] Y Takakura. Optical resonance in a narrow slit in a thick metallic screen. *Physical Review Letters*, 86(24):5601, 2001.

[170] F Yang and JR Sambles. Resonant transmission of microwaves through a narrow metallic slit. *Physical Review Letters*, 89(6):063901, 2002.

[171] L Novotny. Effective wavelength scaling for optical antennas. *Physical Review Letters*, 98(26):266802, 2007.

[172] J Park, H Kim, IM Lee, S Kim, J Jung, and B Lee. Resonant tunneling of surface plasmon polariton in the plasmonic nano-cavity. *Optics Express*, 16(21):16903–16915, 2008.

[173] HA Jamid and SJ Al-Bader. Diffraction of surface plasmon-polaritons in an abruptly terminated dielectric-metal interface. *IEEE Photonics Technology letters*, 7(3):321–323, 1995.

[174] TA Leskova and NI Gapotchenko. Fabry-perot type interferrometer for surface polaritons: Resonance effects. *Solid State Communications*, 53(4):351–357, 1985.

[175] TA Leskova, AA Maradudin, and W Zierau. Surface plasmon polariton propagation near an index step. *Optics Communications*, 249(1-3):23–35, 2005.

[176] WP Huang and J Mu. Complex coupled-mode theory for optical waveguides. *Optics Express*, 17(21):19134–19152, 2009.

[177] SB Hasan, R Filter, A Ahmed, R Vogelgesang, R Gordon, C Rockstuhl, and F Lederer. Relating localized nanoparticle resonances to an associated antenna problem. *Physical Review B*, 84(19):195405, 2011.

[178] G Liu and B Jacquier. *Spectroscopic properties of rare earths in optical materials*, volume 83. Springer Science & Business Media, 2006.

[179] N Gisin. How far can one send a photon? *Frontiers of Physics*, 10(6):1–8, 2015.

[180] MD Eisaman, J Fan, A Migdall, and SV Polyakov. Invited review article: Single-photon sources and detectors. *Review of Scientific instruments*, 82(7):071101, 2011.

[181] YA Chen, Q Zhang, TY Chen, WQ Cai, SK Liao, J Zhang, K Chen, J Yin, JG Ren, Z Chen, et al. An integrated space-to-ground quantum communication network over 4,600 kilometres. *Nature*, 589(7841):214–219, 2021.

[182] E Desurvire and MN Zervas. Erbium-doped fiber amplifiers: principles and applications. *Physics Today*, 48(2):56, 1995.

[183] W Redjem, A Durand, T Herzig, A Benali, S Pezzagna, J Meijer, A Yu Kuznetsov, HS Nguyen, Sébastien Cueff, J-M Gérard, et al. Single artificial atoms in silicon emitting at telecom wavelengths. *Nature Electronics*, 3(12):738–743, 2020.

[184] PJ Schuck, DP Fromm, A Sundaramurthy, GS Kino, and WE Moerner. Improving the mismatch between light and nanoscale objects with gold bowtie nanoantennas. *Physical Review Letters*, 94(1):017402, 2005.

[185] A Teitelboim, B Tian, DJ Garfield, A Fernandez-Bravo, AC Gotlin, PJ Schuck, BE Cohen, and EM Chan. Energy transfer networks within upconverting nanoparticles are complex systems with collective, robust, and history-dependent dynamics. *The Journal of Physical Chemistry C*, 123(4):2678–2689, 2019.

[186] B Zhou, B Shi, D Jin, and X Liu. Controlling upconversion nanocrystals for emerging applications. *Nature Nanotechnology*, 10(11):924–936, 2015.

[187] M Saboktakin, X Ye, UK Chettiar, N Engheta, CB Murray, and CR Kagan. Plasmonic enhancement of nanophosphor upconversion luminescence in au nanohole arrays. *ACS Nano*, 7(8):7186–7192, 2013.

[188] Y Pang and R Gordon. Optical trapping of 12 nm dielectric spheres using double-nanoholes in a gold film. *Nano Letters*, 11(9):3763–3767, 2011.

[189] M Righini, AS Zelenina, C Girard, and R Quidant. Parallel and selective trapping in a patterned plasmonic landscape. *Nature Physics*, 3(7):477–480, 2007.

[190] M Righini, G Volpe, C Girard, D Petrov, and R Quidant. Surface plasmon optical tweezers: tunable optical manipulation in the femtonewton range. *Physical Review Letters*, 100(18):186804, 2008.

[191] A Kotnala and R Gordon. Quantification of high-efficiency trapping of nanoparticles in a double nanohole optical tweezer. *Nano Letters*, 14(2):853–856, 2014.

[192] H Xu, S Jones, BC Choi, and R Gordon. Characterization of individual magnetic nanoparticles in solution by double nanohole optical tweezers. *Nano Letters*, 16(4):2639–2643, 2016.

[193] Q Jiang, B Rogez, JB Claude, G Baffou, and J Wenger. Quantifying the role of the surfactant and the thermophoretic force in plasmonic nano-optical trapping. *Nano Letters*, 20(12):8811–8817, 2020.

[194] C Hong, S Yang, and JC Ndukaife. Stand-off trapping and manipulation of sub-10 nm objects and biomolecules using opto-thermo-electrohydrodynamic tweezers. *Nature Nanotechnology*, 15(11):908–913, 2020.

[195] SSS Peri, MK Sabnani, MU Raza, EL Urquhart, S Ghaffari, JS Lee, MJ Kim, J Weidanz, and G Alexandrakis. Quantification of low affinity binding interactions between natural killer cell inhibitory receptors and targeting ligands with a self-induced back-action actuated nanopore electrophoresis (sane) sensor. *Nanotechnology*, 32(4):045501, 2020.

[196] D Verschueren, X Shi, and C Dekker. Nano-optical tweezing of single proteins in plasmonic nanopores. *Small Methods*, 3(5):1800465, 2019.

[197] F Eftekhari, C Escobedo, J Ferreira, X Duan, EM Girotto, AG Brolo, R Gordon, and D Sinton. Nanoholes as nanochannels: flow-through plasmonic sensing. *Analytical Chemistry*, 81(11):4308–4311, 2009.

[198] A Lesuffleur, LKS Kumar, AG Brolo, KL Kavanagh, and R Gordon. Apex-enhanced raman spectroscopy using double-hole arrays in a gold film. *The Journal of Physical Chemistry C*, 111(6):2347–2350, 2007.

[199] F Wang, J Wang, and X Liu. Direct evidence of a surface quenching effect on size-dependent luminescence of upconversion nanoparticles. *Angewandte Chemie International Edition*, 49(41):7456–7460, 2010.

[200] A Kotnala, D DePaoli, and R Gordon. Sensing nanoparticles using a double nanohole optical trap. *Lab on a Chip*, 13(20):4142–4146, 2013.

[201] C Lee, EZ Xu, Y Liu, A Teitelboim, K Yao, A Fernandez-Bravo, AM Kotulska, SH Nam, YD Suh, A Bednarkiewicz, et al. Giant nonlinear optical responses from photon-avalanching nanoparticles. *Nature*, 589(7841):230–235, 2021.

[202] J Zenneck. Über die fortpflanzung ebener elektromagnetischer wellen längs einer ebenen leiterfläche und ihre beziehung zur drahtlosen telegraphie. *Annalen der Physik*, 328(10):846–866, 1907.

[203] E Kretschmann. Die bestimmung optischer konstanten von metallen durch anregung von oberflächenplasmaschwingungen. *Zeitschrift für Physik A Hadrons and nuclei*, 241(4):313–324, 1971.

[204] B Liedberg, C Nylander, and I Lundström. Biosensing with surface plasmon resonance—how it all started. *Biosensors and Bioelectronics*, 10(8):i–ix, 1995.

[205] EN Economou. Surface plasmons in thin films. *Physical Review*, 182(2):539, 1969.

[206] P Berini. Bulk and surface sensitivities of surface plasmon waveguides. *New Journal of Physics*, 10(10):105010, 2008.

[207] G Rosenblatt, B Simkhovich, and M Orenstein. Brewster plasmons: new optical degrees of freedom driving the forced repose of nanostructures (conference presentation). In *Metamaterials, Metadevices, and Metasystems 2018*, volume 10719, page 107191R. International Society for Optics and Photonics, 2018.

[208] C Yeh and FI Shimabukuro. *The essence of dielectric waveguides*. Springer, 2008.

[209] MG Moharam and Thomas K Gaylord. Rigorous coupled-wave analysis of metallic surface-relief gratings. *JOSA A*, 3(11):1780–1787, 1986.

[210] S Park, G Lee, SH Song, CH Oh, and PS Kim. Resonant coupling of surface plasmons to radiation modes by use of dielectric gratings. *Optics Letters*, 28(20):1870–1872, 2003.

[211] P Offermans, MC Schaafsma, SRK Rodriguez, Y Zhang, M Crego-Calama, SH Brongersma, and J Gomez Rivas. Universal scaling of the figure of merit of plasmonic sensors. *ACS Nano*, 5(6):5151–5157, 2011.

[212] M Piliarik and J Homola. Surface plasmon resonance (spr) sensors: approaching their limits? *Optics Express*, 17(19):16505–16517, 2009.

[213] P Nagpal, NC Lindquist, SH Oh, and DJ Norris. Ultrasmooth patterned metals for plasmonics and metamaterials. *Science*, 325(5940):594–597, 2009.

[214] A Kossoy, V Merk, D Simakov, K Leosson, S Kéna-Cohen, and SA Maier. Optical and structural properties of ultra-thin gold films. *Advanced Optical Materials*, 3(1):71–77, 2015.

[215] AV Kabashin, P Evans, S Pastkovsky, W Hendren, GA Wurtz, R Atkinson, R Pollard, VA Podolskiy, and AV Zayats. Plasmonic nanorod metamaterials for biosensing. *Nature Materials*, 8(11):867–871, 2009.

[216] ML Juan, M Righini, and R Quidant. Plasmon nano-optical tweezers. *Nature Photonics*, 5(6):349–356, 2011.

[217] Q Jiang, JB Claude, and J Wenger. Plasmonic nano-optical trap stiffness measurements and design optimization. *Nanoscale*, 13(7):4188–4194, 2021.

[218] IC Huang, J Holzgrafe, RA Jensen, JT Choy, MG Bawendi, and M Lončar. 10 nm gap bowtie plasmonic apertures fabricated by modified lift-off process. *Applied Physics Letters*, 109(13):133105, 2016.

[219] H Tan, H Hu, L Huang, and K Qian. Plasmonic tweezers for optical manipulation and biomedical applications. *Analyst*, 145(17):5699–5712, 2020.

[220] Y Zhang, C Min, X Dou, X Wang, HP Urbach, MG Somekh, and X Yuan. Plasmonic tweezers: for nanoscale optical trapping and beyond. *Light: Science & Applications*, 10(1):1–41, 2021.

[221] TD Bouloumis, DG Kotsifaki, X Han, SN Chormaic, and VG Truong. Fast and efficient nanoparticle trapping using plasmonic connected nanoring apertures. *Nanotechnology*, 32(2):025507, 2020.

[222] A Kotnala, H Ding, and Y Zheng. Enhancing single-molecule fluorescence spectroscopy with simple and robust hybrid nanoapertures. *ACS Photonics*, 8(6):1673–1682, 2021.

[223] N Li, J Cadusch, A Liu, AJ Barlow, A Roberts, and KB Crozier. Algorithm-designed plasmonic nanotweezers: Quantitative comparison by theory, cathodoluminescence, and nanoparticle trapping. *Advanced Optical Materials*, 9(19):2100758, 2021.

[224] Z Xu, W Song, and KB Crozier. Direct particle tracking observation and brownian dynamics simulations of a single nanoparticle optically trapped by a plasmonic nanoaperture. *Acs Photonics*, 5(7):2850–2859, 2018.

[225] Q Jiang, P Roy, JB Claude, and journal=Nano Letters volume=21 number=16 pages=7030–7036 year=2021 publisher=ACS Publications Wenger, J. Single photon source from a nanoantenna-trapped single quantum dot.

[226] MS Shariatdoust, AL Frencken, A Khademi, A Alizadehkhaledi, F CJM van Veggel, and R Gordon. Harvesting dual-wavelength excitation with plasmon-enhanced emission from upconverting nanoparticles. *ACS Photonics*, 5(9):3507–3512, 2018.

[227] M Belkin, SH Chao, MP Jonsson, C Dekker, and A Aksimentiev. Plasmonic nanopores for trapping, controlling displacement, and sequencing of dna. *ACS Nano*, 9(11):10598–10611, 2015.

[228] AA Al Balushi, A Kotnala, S Wheaton, RM Gelfand, Y Rajashekara, and R Gordon. Label-free free-solution nanoaperture optical tweezers for single molecule protein studies. *Analyst*, 140(14):4760–4778, 2015.

[229] X Peng, A Kotnala, BB Rajeeva, M Wang, K Yao, N Bhatt, D Penley, and Y Zheng. Plasmonic nanotweezers and nanosensors for point-of-care applications. *Advanced Optical Materials*, 9(13):2100050, 2021.

[230] C Ying, E Karakaci, Esteban BU, A Ianiro, C Foster, S Awasthi, A Guha, L Bryan, J List, S Balog, et al. Watching single unmodified enzymes at work. *ArXiv Preprint ArXiv:2107.06407*, 2021.

[231] R Gordon. Biosensing with nanoaperture optical tweezers. *Optics & Laser Technology*, 109:328–335, 2019.

[232] S Wheaton and R Gordon. Single molecule protein sizing in double nano-hole optical tweezers. In *Optical Trapping Applications*, pages OtM3E–5. Optical Society of America, 2015.

[233] AA Al Balushi and R Gordon. Label-free free-solution single-molecule protein–small molecule interaction observed by double-nanohole plasmonic trapping. *ACS Photonics*, 1(5):389–393, 2014.

[234] SSS Peri, MK Sabnani, MU Raza, S Ghaffari, S Gimlin, DD Wawro, JS Lee, MJ Kim, J Weidanz, and G Alexandrakis. Detection of specific antibody-ligand interactions with a self-induced back-action actuated nanopore electrophoresis sensor. *Nanotechnology*, 31(8):085502, 2019.

[235] A Zehtabi-Oskuie, H Jiang, BR Cyr, DW Rennehan, AA Al-Balushi, and R Gordon. Double nanohole optical trapping: dynamics and protein-antibody co-trapping. *Lab on a Chip*, 13(13):2563–2568, 2013.

[236] S Wheaton, RM Gelfand, and R Gordon. Probing the raman-active acoustic vibrations of nanoparticles with extraordinary spectral resolution. *Nature Photonics*, 9(1):68–72, 2015.

[237] R Regmi, AA Al Balushi, H Rigneault, R Gordon, and J Wenger. Nanoscale volume confinement and fluorescence enhancement with double nanohole aperture. *Scientific Reports*, 5(1):1–10, 2015.

[238] SH Behrens and DG Grier. The charge of glass and silica surfaces. *The Journal of Chemical Physics*, 115(14):6716–6721, 2001.

[239] J Sotres and AM Baró. Afm imaging and analysis of electrostatic double layer forces on single dna molecules. *Biophysical Journal*, 98(9):1995–2004, 2010.

[240] PK Das, S Bhattacharjee, and W Moussa. Electrostatic double layer force between two spherical particles in a straight cylindrical capillary: Finite element analysis. *Langmuir*, 19(10):4162–4172, 2003.

[241] A Asadinezhad, M Lehockỳ, P Sáha, and M Mozetič. Recent progress in surface modification of polyvinyl chloride. *Materials*, 5(12):2937–2959, 2012.

[242] Y Gu and D Li. The ζ-potential of glass surface in contact with aqueous solutions. *Journal of Colloid and Interface Science*, 226(2):328–339, 2000.

[243] H Cai, Y Wang, K Wu, and W Guo. Enhanced hydrophilic and electrophilic properties of polyvinyl chloride (pvc) biofilm carrier. *Polymers*, 12(6):1240, 2020.

[244] ED Palik. *Handbook of optical constants of solids*, volume 3. Academic press, 1998.

Appendix A

Large Plasmonic Resonance Shifts from Metal Loss in Slits

2022, Plasmonics, volume 17(1), pp 315-320

Reprinted with permission from Plasmonics Journal, Springer

ZOHREH SHARIFI[1], and REUVEN GORDON[1,*]

1Department of Electrical and Computer Engineering, University of Victoria, Victoria, BC, v8P5C2
*Corresponding author: rgordon@uvic.ca

Received: 19 March 2021 / Accepted: 26 July 2021

Abstract

The impact of loss on the plasmonic resonances in metal-insulator-metal slits is analyzed, particularly the significant effect of loss on the reflection phase. The reflection is calculated analytically using single mode matching theory with the unconjugated form of the orthogonality relation. This theoretical calculation agrees well with comprehensive simulations, but differs substantially from the conjugated orthogonality result, as was used in past analytical works. This reflection phase has a large impact on the plasmonic resonance wavelengths, which are calculated using a Fabry-Pérot theory and compared with past experiment and finite-difference time-domain simula-

tions.

Introduction

Subwavelength slits in metal allow for confining light to the nanometer scale [144, 150, 151, 152], which is a million times smaller than the wavelength for millimeter waves [153, 154]. While the non-resonant case already supports 10^4 field enhancement [155], the resonant case gives even larger enhancement by constructive interference with multiple reflections from the end faces of the slit [156, 157, 158, 159]. Metal-insulator-metal (MIM) plasmonic slits also enhance optical absorption [160, 161]. There has also been great interest in analyzing the dispersion properties of MIM structures[162, 163, 164]. The easy fabrication of the MIM structures makes this geometry well-suited for nanophotonic applications [30, 165, 166, 167, 168].

The theory of the transmission of light through single slit in a perfect electric conductor has been studied extensively in the past [142, 169]. It was shown that the maxima in the transmission spectrum are different from the normal Fabry-Pérot resonances, with zero phase shift upon reflection, as confirmed by experiment [170]. In MIM structures, the plasmon wavevector and the phase of reflection from the end faces determines the resonant length of the cavity. The resonance length is not equal to the simple multiple of the half-wavelength in general because of large reflection phase [171, 172]. Therefore, to predict MIM cavity resonances, calculation of the reflection phase is necessary.

SPP reflection has been investigated for single slit with different dielectric and metallic materials [173, 174, 175]. For MIM cavities, analytical calculations of the reflection phase have been done for lossless and dispersion-free metals by our group [142]. Another group advanced this theory for a real metal while still using the conjugated form of the orthogonality relation [143].

In this paper, we calculate analytically the reflection coefficient and phase acquired by SPPs upon reflection from the slit end-face using a simple mode matching model for real metals exhibiting both dispersion and loss. The approach is similar to past works [142, 143] except that we employ the unconjugated form of the orthogonality relation. Our method shows good agreement with comprehensive finite difference time domain (FDTD) simulations, even for thin slits at the nanometer scale. By comparison, we show that the conjugated form of the orthogonality, as used in past works, differs considerably from the simulation results at shorter wavelengths, espe-

cially for narrower slits. We use the reflection phase to calculate plasmon resonances and plot the dispersion. The resulting dispersion shows good agreement with past experimental results [144]. The unconjugated approach is more accurate than the conjugated form because the conjugated form is not a proper orthogonality relation (i.e., it gives non-zero values for different modes) when there is loss or gain [176] The unconjugated form is a proper orthogonality relation for the loss/gain cases and it isolates each mode given a value of zero for different modes — for the case of single mode matching approximation, the unconjugated form is therefore more accurate. It is possible to calculate the phase for non-resonant cases. We attempted this approach to calculate the phase [177], however we found that it is numerically challenging and does not give a clear physical interpretation. Our theory shows a clear physical peak that makes the analysis more transparent.

Unconjugated Orthogonality reflection theory

Figure A.1 shows a schematic of the MIM waveguide resonator. Two infinitely thick metal layers are separated by a thin dielectric. The thickness of the dielectric is denoted by w and the SPPs propagate in the z direction. The metal permittivity and the insulator (dielectric) permittivity are ϵ_m and ϵ_d.

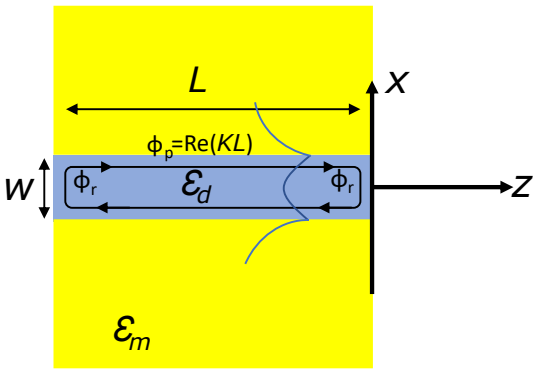

Figure A.1: Schematic representation of the slit with complex permittivity ϵ_d in a real metal with complex permittivity ϵ_m. The electric field profile of the symmetric SPP mode is shown.

Loss affects the cavity resonance by changing the phase of reflection, in addition to the quality factor. In general, MIM waveguides support SPP modes with both symmetric and antisymmetric electric field profiles. If the dielectric is sufficiently thin, only the mode with a symmetric field profile is propagating; such cavities are

considered here. We calculate the propagation constant and the reflection coefficient at the interface to free space for the fundamental TM mode within a slit.

The spatial dependence of the x component of the electric field for the lowest order TM mode within the slit can be formulated as:

$$E_x^s(x,z) = \begin{cases} \cosh\left(\sqrt{\varepsilon_d k_0^2 - k_z^2}x\right)\exp\left(ik_z z\right) & \text{if} |x| \leqslant w/2 \\ \frac{1}{\varepsilon_m}\cosh\left(\sqrt{\varepsilon_d k_0^2 - k_z^2}\frac{w}{2}\right) f\left(k_z, x\right)\exp\left(ik_z z\right) & \text{if} |x| > w/2 \end{cases} \tag{A.1}$$

,

$$f\left(k_z, x\right) = \exp\left[-\sqrt{k_z^2 - \varepsilon_m k_0^2}(|x| - w/2)\right]$$

where the superscript s denotes the MIM surface plasmon electric field, k_z is the propagation constant in the z direction, k_0 is the free-space wave vector. The corresponding y component of the magnetic field can be found using the Maxwell-Ampère relation.

The propagation constant is given by:

$$\tanh\left(\sqrt{k_z^2 - \epsilon_d k_0^2}w/2\right) = \frac{-\epsilon_d\sqrt{k_z^2 - \epsilon_m k_0^2}}{\epsilon_m\sqrt{k_z^2 - \epsilon_d k_0^2}}. \tag{A.2}$$

We solve this equation for complex k_z by an iterative approach.

The reflection coefficient is calculated using single mode matching theory with the unconjugated orthogonality. Continuity of the tangential electric and magnetic fields at the boundary, z=0, gives:

$$(1+r)E_x^s = \int_{-\infty}^{\infty} t\left(k_x\right)\exp\left(ik_x x\right)dk_x \tag{A.3}$$

$$(1-r)H_y^s = \int_{-\infty}^{\infty} \frac{t\left(k_x\right)\omega\varepsilon_0}{\sqrt{k_0^2 - k_x^2}}\exp\left(ik_x x\right)dk_x \tag{A.4}$$

where the electric field in the free space region is written as an infinite sum of plane wave modes and t and r are transmission and reflection coefficients.

Using the unconjugated form of the orthogonality relation we multiply both side of Equation A.3 and A.4 by H_y^{fs} and E_x^s, where H_y^{fs} which is the free space magnetic field equals

$$H_y^{fs} = \int_{-\infty}^{\infty}\exp\left(ik_x' x\right)dx \tag{A.5}$$

where k'_x is the free space plane wave propagation constant. Then Equations A.3 and A.4 convert to

$$\int_{-\infty}^{\infty}(1+r)e^{ik'_x x}E_x^s dx = \int_{-\infty}^{\infty} t\left(k_x\right)\exp\left(\left(ik_x + ik'_x\right)x\right)dk_x \tag{A.6}$$

$$\int_{-\infty}^{\infty}(1-r)\frac{\omega\varepsilon}{\beta}\left(E_x^s\right)^2 dx = \omega\varepsilon_0\int_{-\infty}^{\infty}\frac{t\left(k_x\right)}{\sqrt{k_0^2-k_x^2}}\left[\int_{-\infty}^{\infty}E_x^s\exp\left(ik_x x\right)\right]dk_x \tag{A.7}$$

solving Equations A.6 and A.7 for r, the reflection coefficient can be found:

$$r = \frac{1-G}{1+G} \quad , \quad G = \frac{1}{2\pi}\frac{\int_{-\infty}^{\infty}\frac{k_0}{Z_0\sqrt{k_0^2-k_x^2}}\left[\int_{-\infty}^{\infty}E_x^s\exp\left(ik_x x\right)\right]^2 dk_x}{\int_{-\infty}^{\infty}E_x^s(x,0)H_y^s(x,0)dx} \tag{A.8}$$

where H_y^s is the surface plasmon magnetic field in the cavity, Z_0 is the characteristic impedance of free space. We calculate k_z from Equation A.2 for lossy and lossless cases (with and without considering the imaginary part of the relative permitivity of the metal) and use the values to calculate the elctric and magnetic field using Equation A.1 and then calculate the reflection coefficient in Eqution A.8. Comparing Equation A.8 with past work [143], the unconjugated orthogonality is different here and appears in the denominator of G. This has a significant impact on the reflection coefficient when loss is considered.

Figure A.2 shows the impact of loss for an Au-air-Au structure. As it is clear for shorter wavelengths and shorter width, the metal loss affects phase of reflection. In a lossy MIM structure, the mode index does not get as large as in the lossless case at short wavelengths. Consequently, the smaller index and the decreased confinement lead to the difference for lossy and lossless case. At longer wavelengths, because the SPP mode is pushed out of the metal, losses are negligible and the reflection characteristics are similar to the lossless case. A huge difference can also be seen when considering the unconjugated form of the orthogonality relation. To make a comparison with past work [143], the phase of reflection has been calculated for three different metals (Au, Al, Ag). Figure A.3 compares phase of reflection for slit width of 50 nm considering loss of the metal using both conjugated and unconjugated forms. Comparing the results for Ag with the results past works [143], the difference of reflection phase in the two methods is obvious. This shows the importance of

considering both the metal loss and conjugated form of the orthogonality relation in the calculation of the reflection phase.

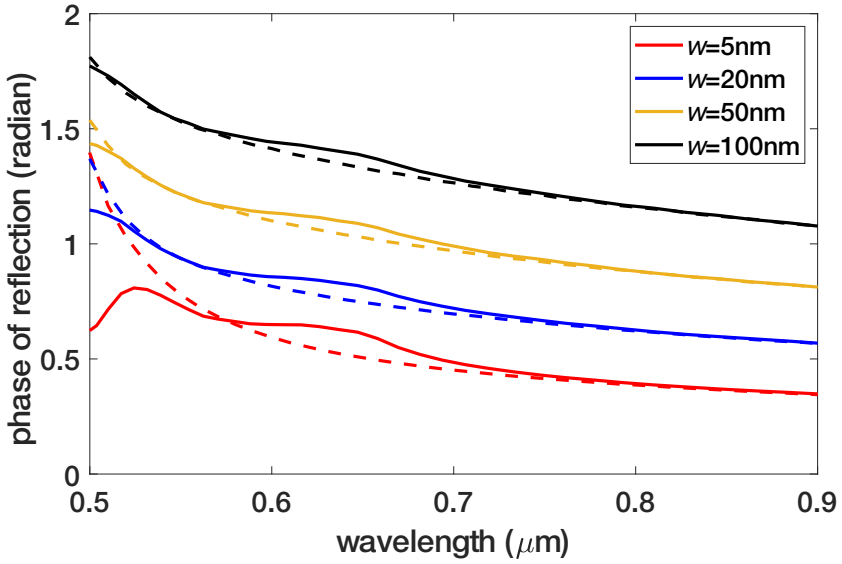

Figure A.2: Reflection phase for an Au-air-Au structure as a function of wavelength for different slit width. Solid lines show the results for the lossy cases and dashed lines show the results for the lossless cases.

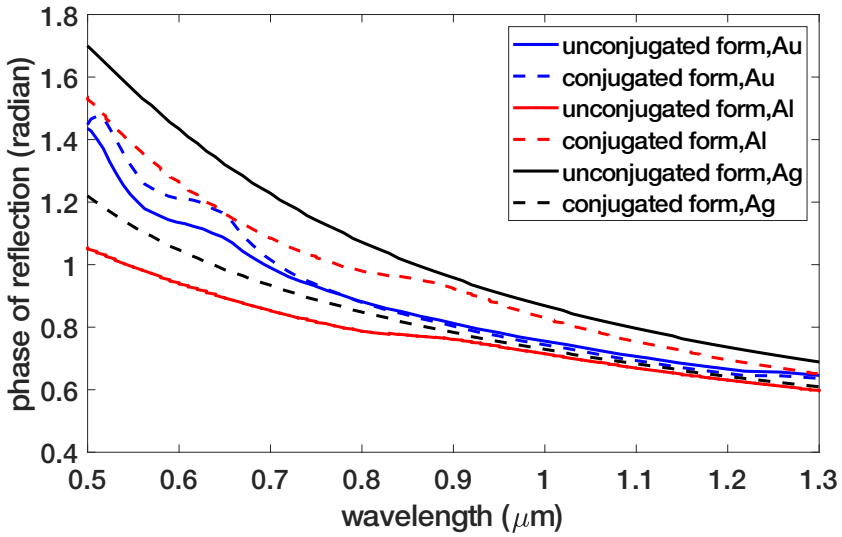

Figure A.3: Reflection phase as a function of wavelength for a MIM structure for different metals and using the conjugated and unconjugated form of the orthogonality relation for slit width of 50 nm.

Figure A.4 compares reflection coefficient phase for an Au-air-AU structure for different slit width using both the conjugated [143] and unconjugated forms of the

orthogonality. The unconjugated form results are plotted with solid lines and the conjugated results are plotted with dashed lines. A clear and significant difference is seen between the two approaches, which is most profound for narrower slits and shorter wavelengths. The reflection phase decreases with increasing wavelength and is larger for a thicker slit. The phase is clearly affected by the introduction of losses in the metal, which is different from what was suggested in past works [143].

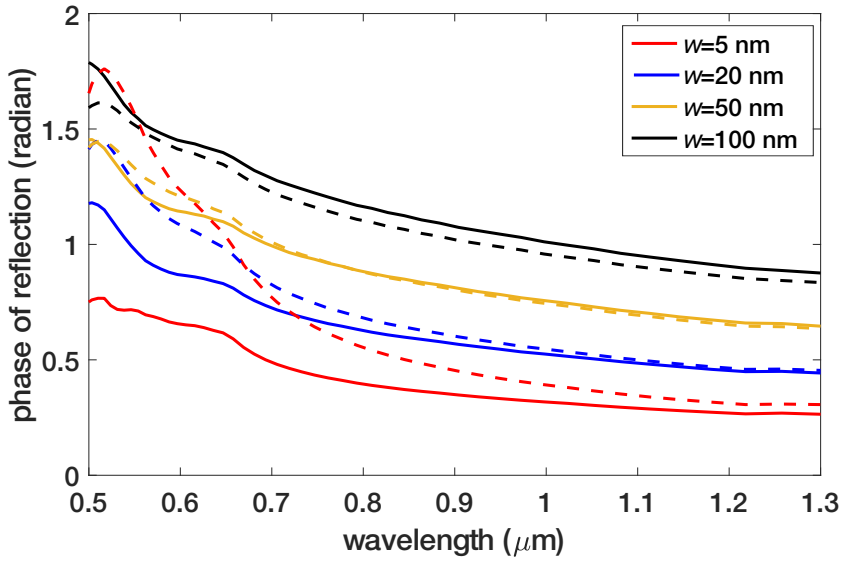

Figure A.4: Reflection phase for an Au-air-Au structure as a function of wavelength for different slit width. Solid lines show the results using unconjugated form of the orthogonality and dashed lines show the results using the conjugated form of the orthogonality.

Comparison with FDTD simulations

To determine the validity of this theory, we used commercial FDTD simulations (Lumerical FDTD ver. 2020 R2.3). Perfectly matched layer boundary conditions were used to prevent reflection of the outgoing waves. The simulation cross-section area was chosen to surround the whole structure. The mesh sizes along the x and z directions were reduced in size to ensure convergence (which was achieved at 0.01 nm for the smallest slit). A normally incident plane wave source was used to excite the structure. The simulation domain was 1.6 $\times$ 1.5 μm. A frequency domain power monitor was placed at the exit side of the slit to record the transmission. In addition to convergence tests, the simulations were compared with past simulations for the

same conditions. Figure A.5 shows the power distribution inside the slit for the slit width of 20 nm and L=250 nm. A TM-polarized plane wave of λ=1.08 μm is incident from the left. The white dashed lines are the borders of the slit.

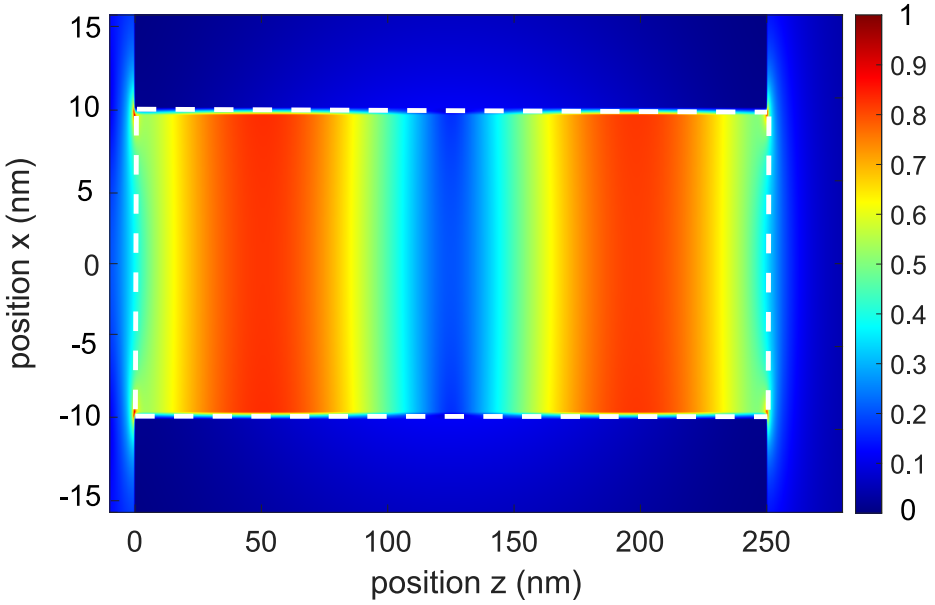

Figure A.5: Power distribution inside the slit for the slit width of 20 nm and L=250 nm. A TM-polarized plane wave of λ=1.08 μm is incident from the left. The white dashed lines are the borders of the slit.

Figure A.6 a and b shows the electric and magnetic fields inside the structure along the z and x directions. The figure compares well with past simulations [167]. Energy confinement is clearly visualized in the Figures. Furthermore, the field distribution shows a standing wave inside the MIM region. Note that the electric field is maximized near the entrance and the exit surfaces. The strong energy confinement of MIM cavities can give strong light-matter interaction, even with losses considered.

Figure A.7 shows the numerically simulated transmission through slit width of 20 nm for different values of L. Resonant transmission peaks are observed with a wavelength that increases as the slit length increases. The propagation constant, k_z, at the resonance wavelength was calculated in FDTD using the mode-source feature. The phase of reflection, Φ_r, was calculated using

$$\Phi_r = m\pi - k_z L \tag{A.9}$$

where L is the length of the slit, m is integer order of resonance.

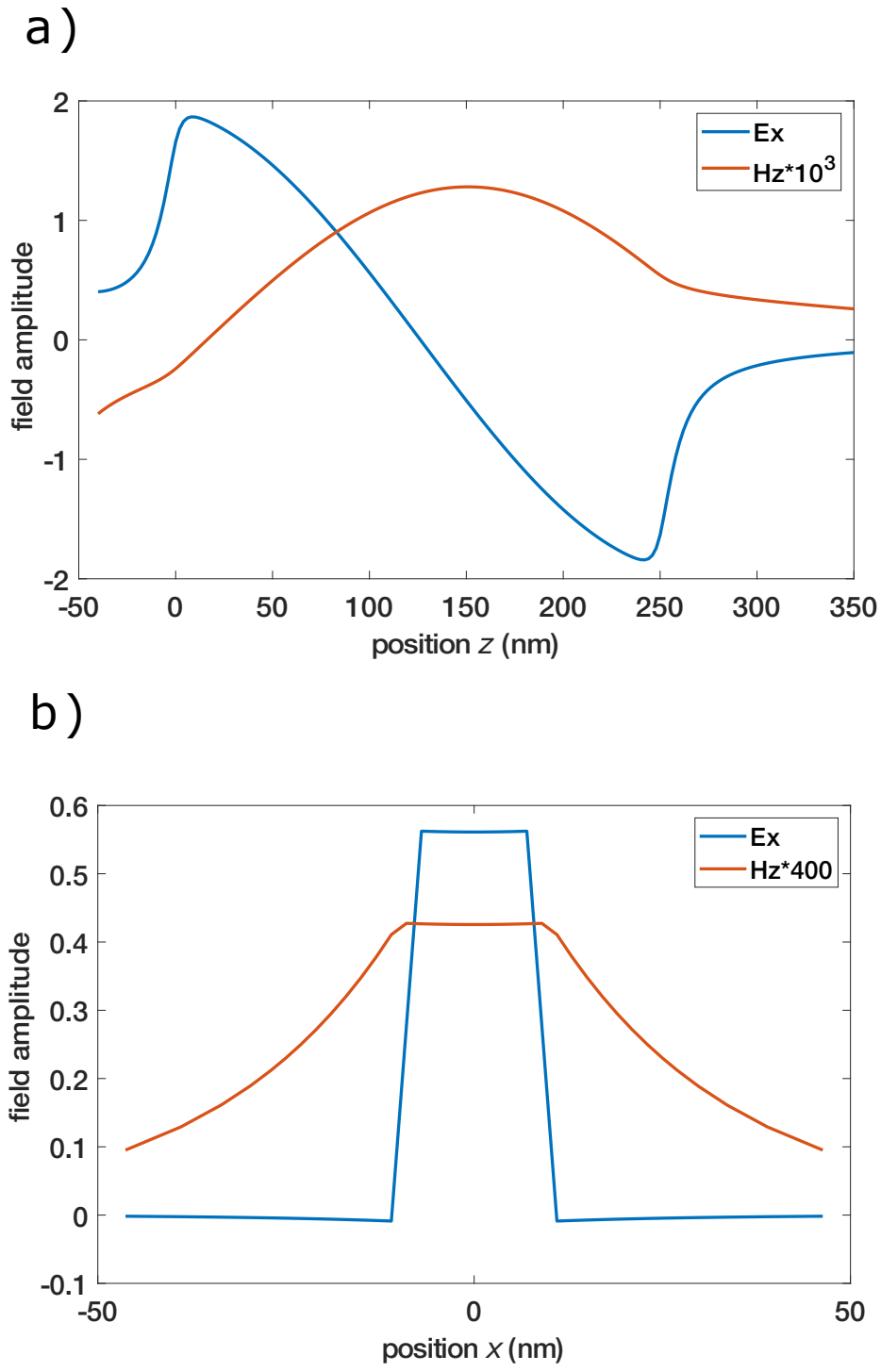

Figure A.6: Electric and magnetic fields inside the structure a) in the z direction (for $x = 0$. b) in the x direction (for $z = 150$ nm.

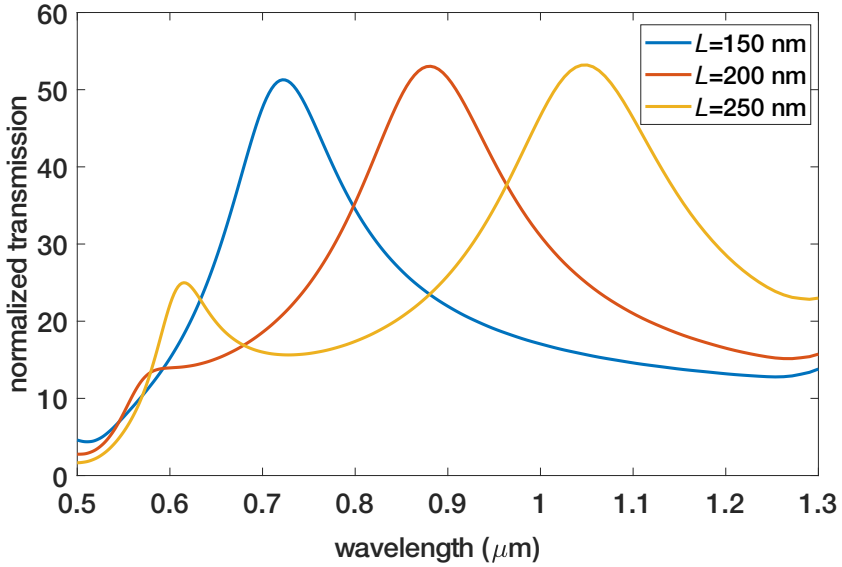

Figure A.7: Transmission through a 20 nm wide slit in an Au-air-Au structure as a function of wavelength. The transmission peak wavelength increases by increasing the slit length.

Figure A.8 compares the phase of reflection calculated using the formulation above and the FDTD simulations with the theory presented in the last section. Equation A.9 is the usual formula for the FP case. Here the difference is that Φ_r is modified for the lossy case following the theory outlined above. Good agreement is seen between the analytic theory and the comprehensive FDTD results, thus supporting the use of the unconjugated orthogonality formulation. Although a slight difference can be seen for shorter wavelengths and especially for the shortest slit width, comparing this Figure with Figure A.4 shows that the unconjugated method results are close to the simulation results. The difference between our results and the simulation results comes from simulation accuracy and the approximation in the single mode matching theory.

Comparison with Experimental data

We compare the theory with a past experiment of narrow slits using a silica spacer layer [144]. A dielectric constant of $\epsilon_d = 2.1$ was used in Eq. A.2 to match the experimental conditions.

Figure A.9 shows the experimental data of the MIM waveguides for different slit widths and lengths, digitized from [144]. The theoretical dispersion curves are

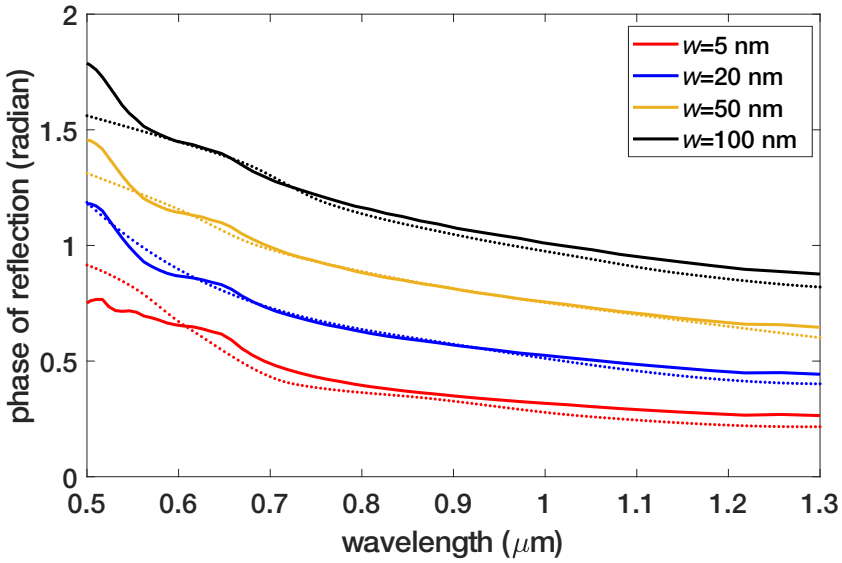

Figure A.8: Reflection phase using unconjugated method in comparison with FDTD simulations in an Au-air-Au structure. Solid lines show the results using unconjugated form of the orthogonality and dotted lines are from the simulations.

shown for three different cases: the dashed line ignores the phase of reflection, the thick solid line is from the theory presented above and the dotted line is our FDTD simulation. Clearly, the phase of reflection plays an important role in determining the plasmonic resonances seen in experiment, and the simple theory presented above accurately accounts for this phase.

Conclusion

In conclusion, we have provided a theory for the phase of reflection from a plasmonic slit that incorporates the real loss of the metal using the unconjugated form of the orthogonality relation. The impact of the real loss on the reflection phase is significant. Thereby, the imaginary part of the permittivity impacts not only the quality factor, but also the plasmonic resonance wavelength. The results for the unconjugated form differ significantly from the conjugated form that was presented in past works. The theory presented here agrees well with full-field FDTD simulations and past experiments, showing promise for simple theoretical investigation of future plasmonic MIM structures.

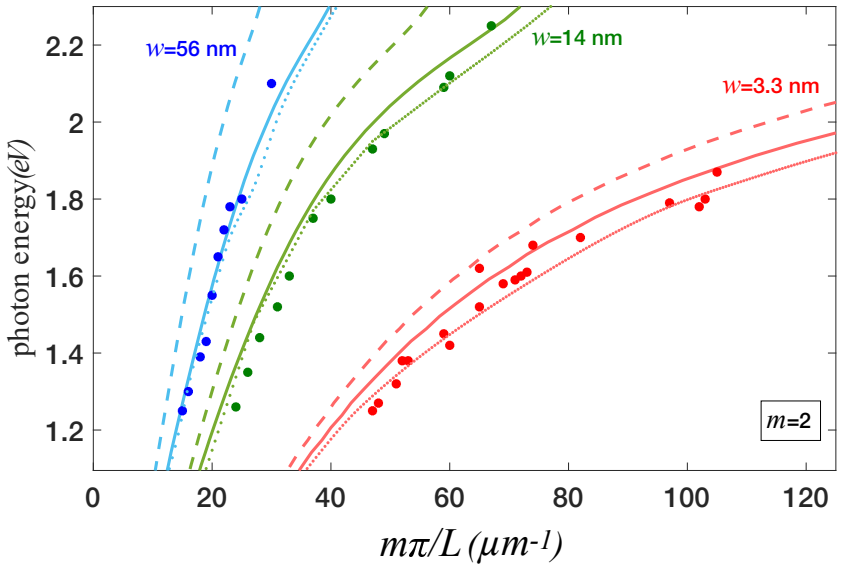

Figure A.9: Dispersion relation for an Au-Silica-Au structure. Solid lines: calculation of dispersion considering the effect of the reflection phase calculated using unconjugated form of the orthogonality relation. Dashed lines: calculation of dispersion ignoring the effect of the reflection phase as was done in the past analysis. Dotted lines: FDTD simulation. Discrete points: experimental results using the experimentally measured plasmonic resonances [144]. The theory presented above shows good agreement with both FDTD and experiment.

Appendix B

Isolating and Enhancing Single Photon Emitters for 1550 nm Quantum Light Sources using Double Nanohole Optical Tweezers

2021, The Journal of Chemical Physics, volume 154(18), pp 184204

ZOHREH SHARIFI[1,2], MICHAEL DOBINSON[1,2], GHAZAL HAJISALEM[1,2], MIRALI SEYED SHARIATDOUST[1,2], ADRIAAN L. FRENCKEN[2,3], FRANK C. J. M. VAN VEGGEL[2,3], and REUVEN GORDON[1,2,a]

1Department of Electrical and Computer Engineering, University of Victoria, Victoria, British Columbia V8P 5C2, Canada
2Centre for Advanced Materials and Related Technologies (CAMTEC), University of Victoria, Victoria, British Columbia V8W 2Y2, Canada
3Department of Chemistry, University of Victoria, Victoria, British Columbia V8W 2Y2, Canada
Note: This paper is part of the JCP Special Topic on Quantum Light.
a)Author to whom correspondence should be addressed: rgordon@uvic.ca

Cite as: J. Chem. Phys. 154, 184204 (2021); doi: 10.1063/5.0048728 Submitted: 25

February 2021 • Accepted: 29 April 2021 • Published Online: 14 May 2021

Abstract

Single-photons sources are required for quantum technologies and can be created from individual atoms and atom-like defects. Erbium ions produce single photons at low-loss fiber optic wavelengths, but they have low emission rates, making them challenging to isolate reliably. Here, we tune the size of gold double nanoholes (DNH) to enhance the emission of single erbium emitters, achieving 50× enhancement over rectangular apertures previously demonstrated. This produces enough enhancement to show emission from single nanocrystals at wavelengths not seen in our previous work i.e., 400 nm and 1550 nm. We observe discrete levels of emission for nanocrystals with low numbers of emitters and demonstrate isolating single emitters. We describe how the trapping time is proportional to the enhancement factor for a given DNH structure, giving us an independent way to measure the enhancement. This shows a promising path to achieving single emitter sources at 1550 nm.

Introduction

Single-photon sources are a key component for many quantum technologies and many efforts have explored using single atoms and atom-like defects as single emitters. Rare-earth ions have been found to be good candidates for single emitters as they produce stable emission and their quantum state can be controlled. [93, 95, 101, 178] The need for a stable single-photon source that has high transmission efficiency in optical fibers is only increasing as quantum communication becomes more advanced. [179, 180, 181] This motivates the search for a source of single photons at low-loss telecom wavelengths for long-distance fiber propagation. Erbium is of particular interest as it emits in the C-band, the lowest-loss band for fiber transmission, a characteristic which is already widely used in erbium-doped fiber amplifiers for long-distance telecommunications. [182] Single erbium emitters have also been demonstrated, but a remaining challenge is finding a reliable method to isolate single emitters. [85]

Methods of producing single emitters typically yield random distributions and most rely on either searching among them or using low concentrations to find the single emitters. [101, 183] Isolating single rare-earth emitters is particularly challenging as they have low emission rates due to long excited state lifetimes. [178] Some

approaches have been explored to isolate rare-earth emitters by precisely implanting ions in crystals, making the process nearly deterministic but suffering from low yield. [102] Our group has previously demonstrated a scalable method of isolating single erbium emitters by measuring their discrete emission levels in an optical tweezer setup. [103]

Plasmonics can be used to enhance the emission rate of single emitters and make isolating them more practical. Nanoscale structures can create plasmonic enhancement which concentrates the incident electric field, enhancing emission from luminescent particles by increasing the radiative emission and non-radiative decay rates. [2, 84, 184, 185] As applied to an Er-doped nanocrystal, this can allow a well-designed structure to increase its viability as a single photon source, [85, 86] and has other applications such as photocatalysis [186] and enabling subwavelength luminescence imaging with IR excitation. [186] Structures can also be designed with multiple plasmonic resonances, which has been shown before with aperture arrays in metal. [10, 148, 187]

Plasmonic resonance not only enhances the emission, it also helps to isolate smaller particles, using the enhanced local field as optical tweezers. [145, 188] Optical tweezers are well-established and have been widely used to trap and manipulate nanoparticles, [110] but trapping particles in the subwavelength scale typically requires high intensities when using conventional single beam traps. Rayleigh scattering also makes it challenging to trap and characterize small particles. [110, 114] Apertures in metal films can be used to enhance the local field through plasmonic resonance, and when applied to optical tweezers this makes it easier to trap subwavelength particles well below 100 nm with lower beam intensity. [7, 114, 149, 125, 127, 189, 190] Several aperture designs have been evaluated in past works including double nanohole (DNH),[191, 192] bowtie,[8, 122] and rectangular [145] apertures.

Our group has previously shown that using a rectangular aperture to trap Yb–Er-doped $NaYF_4$ nanocrystals enhances emission by a factor of 400 when tuned for both the excitation and emission wavelengths. [10] Rectangular apertures have also been used by our group to trap $NaYF_4$ nanocrystals with trace doping of Er, finding discrete levels of emission. The discrete levels indicate how many emitters are present in the trapped nanocrystal, allowing nanocrystals with single emitters to be reliably isolated. [103] DNH structures have been found to produce greater local field enhancement compared to rectangular apertures, which can make isolating single emitters easier. [188] These properties make DNHs useful for other applications as

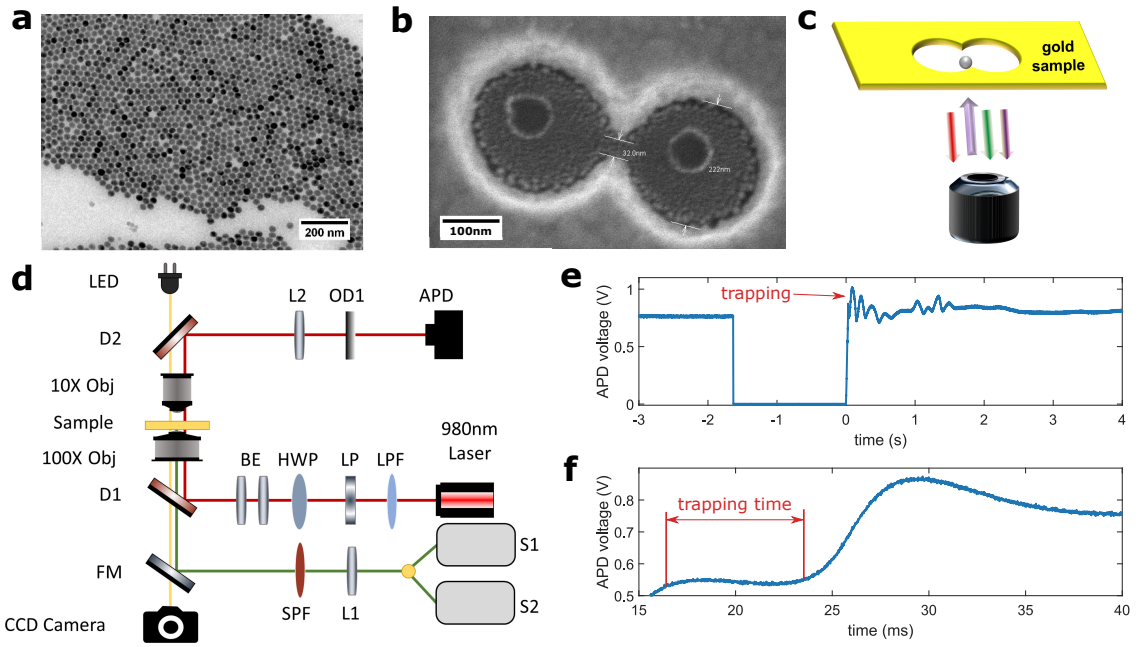

Figure B.1: Optical trapping of Yb–Er-doped $NaYF_4$ nanocrystals with DNH. (a) Image of $NaYF_4$ nanocrystals with nominal diameter of 26.2 nm. (b) Image of a fabricated DNH structure with 32 nm cusp separation and 222 nm aperture diameter, taken with scanning electron microscope. (c) Schematic of a trapped nanocrystal in a DNH aperture on a gold sample. (d) Schematic of optical tweezer setup. (e) Optical transmission through a 32 nm DNH aperture in a metal film trapping a 26.2 nm nanocrystal, as measured by the APD voltage. Laser is turned on at 0 s. (f) Magnified region showing the APD voltage change shortly after the laser is turned on and trapping time measurement.

well, such as biosensing. [146]

Here, we optically trap two different sizes of nanocrystals, made of $NaYF_4$ doped with 18% Yb and 2% Er, with plasmonic DNH aperture optical tweezers and characterize their emission spectra and trapping rate for different cusp separations. The DNH apertures exhibit multiple resonances within a single structure and further enhances the emission from individual nanocrystals by ˜50× compared to previous findings with rectangular apertures. [10] We also, for the first time, observe new resonances from nanocrystals trapped in a DNH at 400 nm and 1550 nm.

Using the DNH apertures with the best geometry, we optically trap nanocrystals made of $NaYF_4$ with low concentrations of Er^{3+}. We observe discrete emission levels corresponding the different numbers of active emitters and isolate nanocrystals with single emitters. Furthermore, we explore the relation between the trapping dynamics and emission enhancement.

We note that recent works have used thermophoretic forces [193, 194] and nanopore flow [195, 196, 197] to bring the particles closer to the surface. Since the trapping already happens in less than a second, we do not presently see any benefit for these approaches, but we do see potential of these approaches for water-based experiments where the trapping is slower (likely due to repulsive surface charges).

Tuning DNH Aperture to Maximize Enhancement

A range of DNH apertures with average cusp separations from 23 to 95 nm were fabricated to evaluate the emission enhancement. Cusp separation was the focus because the cusp is where DNH apertures produce the highest field intensity. [128, 198] Samples with DNH apertures are fabricated in a 70 nm thick gold film on a glass substrate using a colloidal lithography method previously reported on by our group. [14] Scanning electron microscopy was used to measure the average cusp separation of the DNH structures in each sample. Two different sizes of nanocrystals – nominally 16.9 nm and 26.2 nm in diameter, with standard deviations of 1.3 nm and 2.7 nm – were made of $NaYF_4$ doped with 18% Yb and 2% Er, dispersed in a hexane solution. Figure B.1(a) shows an image of the 26.2 nm nanocrystals. Figure B.1(b) shows an example of a DNH that was fabricated with a cusp separation of 32 nm and an aperture diameter of 222 nm.We believe that the smaller circles are created by the nanospheres contacting the surface during deposition. Figure B.1(c) shows a schematic of a nanocrystal trapped in a DNH aperture.

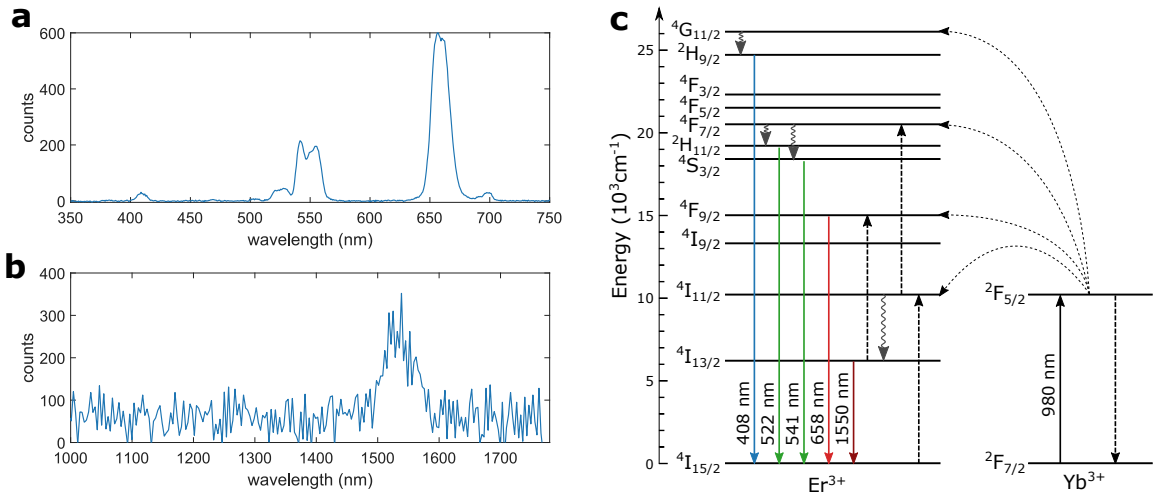

Figure B.2: Measuring the emission spectra from single nanocrystals. (a) Upconversion emission spectra from a 26.2 nm nanocrystal observed for a sample with 32 nm average cusp separation. The counts can be compared for 400, 550 and 650 nm emission peaks. Collected by a spectrometer with a 10 ms acquisition time. (b) Downconversion emission spectra from a 16.9 nm nanocrystal observed for a sample with 32 nm average cusp separation. Collected by a spectrometer with 1 s acquisition time. (c) Schematic energy level diagram of Yb^{3+} sensitizer and Er^{3+} activator in nanocrystals. Radiative energy transfer (solid lines), non-radiative energy transfer (dotted lines), cross-relaxation (dashed lines), and multiphonon relaxation (curly lines). (Adapted from Suyver et al.) [5]

B.1(d) shows a schematic of the optical tweezer setup used to trap the nanocrystals and measure the emission spectra and trapping characteristics. A single 980 nm continuous-wave laser is used for both trapping and excitation of the nanocrystals. Trapping is confirmed by the abrupt jump in the avalanche photodiode (APD) voltage which corresponds to the transmission of light through the aperture.

Figure B.1(e) shows the transmission of light through the DNH aperture and a representative trapping event. The laser is briefly turned off and then turned back on at 0 s. The abrupt jump in the APD voltage, compared to before the laser was turned off, confirms the trapping event.

Figure B.1(f) shows how the trapping time is measured for the trapping event. After turning on the laser, there is a brief period (on the order of milliseconds) before a particle is trapped, this is the trapping time, t_t.

We have observed the oscillation seen in Figure B.1(e) consistently for trapping in hexane [10], but not for trapping in water where a single step is observed [188]. We believe that it is the result of hydrodynamic interactions at the surface, in conjunction with the trapping potential; however, the detailed analysis of this effect is beyond our expertise. The oscillations are not coming from the circuit electronics.

Figures B.2(a) and B.2b show the emission of a single Yb–Er-doped $NaYF_4$ nanocrystal trapped in a DNH aperture with 32 nm average cusp separation. Emission peaks are apparent in Figure B.2(a) near wavelengths of 400 nm, 550 nm, and 650 nm. Figure B.2(b) shows the emission at 1550 nm of a single Yb–Er-doped $NaYF_4$ nanocrystal trapped in a DNH aperture, which we could not observe in our previous measurements [10]. The linewidth in Figure B.2(b) is limited by the emission band of ${}^4I_{13/2} \rightarrow {}^4 I_{15/2}$ levels. Plasmonic resonances found in simulation are much broader. Because the 1550 nm peak is entirely the result of Er, it is not expected to vary significantly in linewidth due to the shifting plasmonic resonances with different nanoholes because the nanoholes show much broader resonances in this region of the spectrum.

We have not previously observed emissions at 400 nm and 1550 nm from single Yb–Er-doped $NaYF_4$ nanocrystals. The 400 nm upconversion emission is from the ${}^2H_{9/2} \rightarrow {}^4 I_{15/2}$ transition in erbium. [5] The 1550 nm downconversion emission is from the ${}^4I_{13/2} \rightarrow {}^4 I_{15/2}$ transition. [182] These transitions can be seen in the energy diagram shown in Figure B.2(c). Observing these two transitions from single nanocrystals for the first time in our group is possible due to the higher enhancement achieved using the double nanoholes.

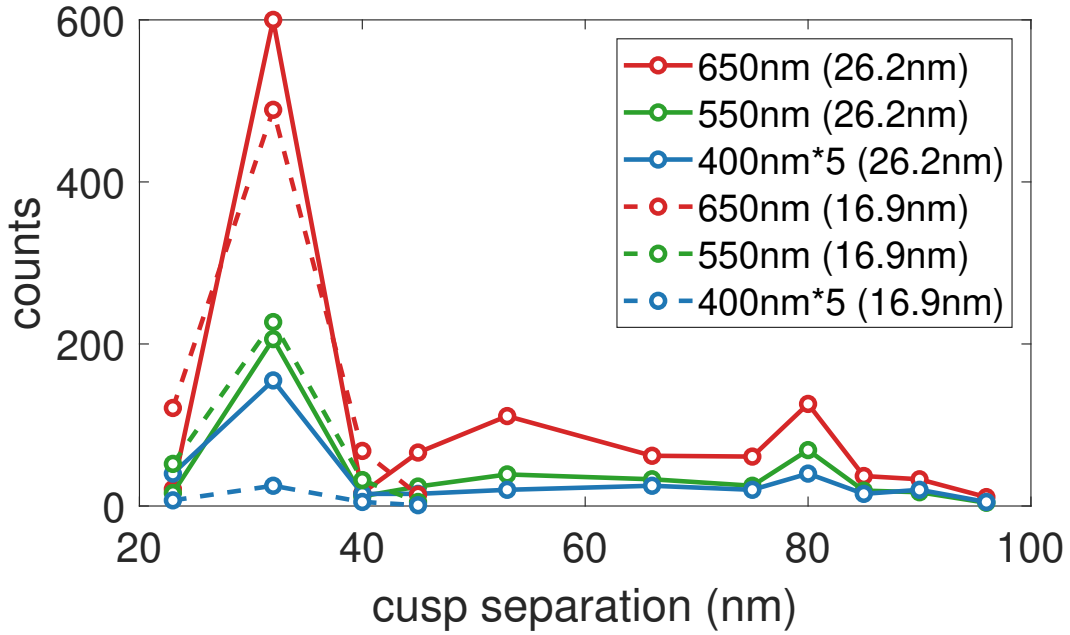

Figure B.3: Investigating the influence of the DNH cusp separation on emission enhancement. Emission from 17 nm and 26 nm nanocrystals at 400 nm, 550 nm, 650 nm for varying DNH cusp separations. Emission counts at 400 nm are multiplied by 5 for visibility.

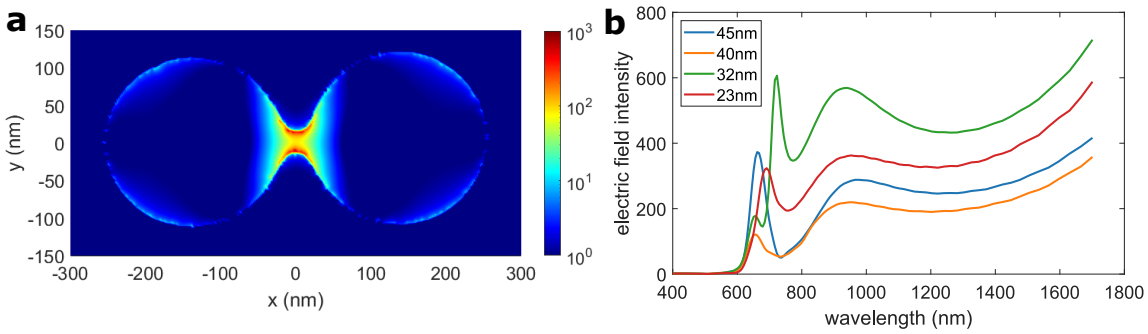

Figure B.4: Simulated electric field intensity. (a) Visualization of the electric field intensity inside of a DNH with 32 nm cusp separation. (b) Electric field intensity for DNHs with 22.7 nm, 32 nm, 40 nm, and 45 nm cusp separations. Normalized to the incident intensity.

Figure B.3 shows the emission of the two sizes of Yb–Er-doped $NaYF_4$ nanocrystals using DNH apertures with varying average cusp separations. It illustrates how the size and shape of the aperture can impact the overall emission. Several measurements on different DNHs within each sample were taken to confirm that the measured emission is from a single trapped nanoparticle. The average of these single trapping events is taken to form the final count. The normalized standard deviation over different measurements of a single 26.2 nm nanocrystal was 2.4%, 4.3% and 6.5% and for a single 16.9 nm nanocrystal it was 3.3%, 5.6%, and 4.8%, for the 400, 550 and 650 nm emission. The laser power is maintained at ˜9 mW (as measured before the 100× objective) to simultaneously excite the structure and trap the particle.

The emission and trapping characteristics of 26.2 nm Yb–Er-doped $NaYF_4$ nanocrystals are measured in ten different samples of DNH apertures with average cusp separations from 32 to 95 nm. We observe that the sample with 32 nm cusp separation has the largest emission and exhibits plasmonic resonance at additional wavelengths, 400 nm and 1550 nm, that are significantly larger than in apertures with other cusp separations. The emission was compared to previous results from our group which used the same experimental setup with rectangular apertures. [10] This aperture size showed additional enhancement factor of approximately 50, over the best rectangular aperture. With the 26.2 nm nanocrystals, enhancement at 400 nm can only be clearly seen in two samples–32 nm and 80 nm average cusp separation.

The 16.9 nm nanocrystals are used to probe the effect of smaller apertures as the 26.2 nm nanocrystals are too large to trap in DNHs with cusp separations under 32 nm. The 16.9 nm nanocrystals are too small to trap in DNHs larger than 45 nm, so the measurements for these were performed for four different samples of DNH apertures with cusp separations from 23 to 45 nm. It was seen that the 32 nm cusp size remained the peak, showing that it has optimal plasmonic resonance to enhance emission at 650 nm. There was one isolated case where a nominally 26.2 nm nanocrystal was trapped in a nominally 23 nm gap, which is possible given the size tolerances.

These results show that the resonance wavelengths shifts as the cusp separation changes. The colloidal lithography method used to prepare these samples adjusts the cusp separation by changing the plasma etching time, this also affects the diameter of the apertures. Changing both the cusp separation and aperture diameter like this can impact both the enhancement factor and resonant wavelengths.

To probe this further we look at FDTD simulations (Lumerical FDTD ver. 2020

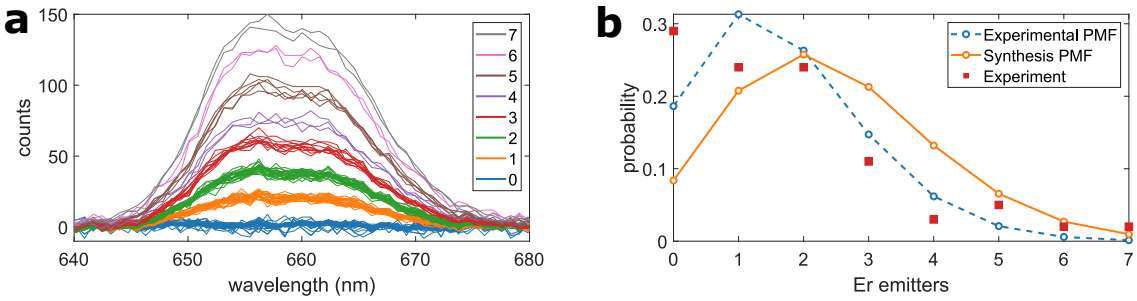

Figure B.5: Measuring discrete emission levels from low counts of erbium emitters. (a) Emission counts from nanocrystals showing discrete levels corresponding to different amounts of active erbium emitters. Collected by a spectrometer with a 1 s acquisition time. (b) Poisson probability mass functions (PMFs) for the experimental ($\lambda = 1.68$) and synthesis ($\lambda = 2.48$) and experimental probabilities for the number of Er emitters.

R2.3). The simulations calculated the electric field inside the cusp of the DNH structure where the particle would be trapped as shown in Figure B.1(c). The structures were modeled from SEM images similar to Figure B.1(b). A total of four different DNHs were modeled around the peak of interest at 32 nm cusp separation. Figure B.4(a) shows the simulated electric field intensity inside the cusp of a 32 nm DNH structure.

Figure B.4(b) shows the simulation result of the relationship between the near-field electric field intensity (normalized to the incident intensity) and wavelength inside the cusp of DNH structure with different cusp separations. It can be seen that the 32 nm cusp separation has the greatest overall electric field intensity. There are two main resonant peaks for each of the simulated DNH structures. The structure with 32 nm cusp separation has peaks at 720 nm and 940 nm. The simulations were performed based on single SEM images and as the resonance frequencies are sensitive to the curvature of the cusps and the exact separation it is expected that the peaks differ slightly from the experimental results. The simulations show that multiple resonances can be used to enhance both excitation and emission wavelengths. There is minimal field enhancement seen in the simulations at 400 nm, but experimental results show increased overall emission at that wavelength. This suggests that the main effect is seen at the excitation wavelength, increasing the energy transfer, with additional resonances for other wavelengths.

Observing Discrete Emission Levels

After finding that a DNH cusp separation of 32 nm shows the best enhancement with Yb-Er-doped nanocrystals, we applied this finding to search for and isolate nanocrystals with single erbium emitters. Dilute Er-doped $NaYF_4$ (with no Yb) nanocrystals were produced with a nominal diameter of 22.7 nm (standard deviation of 2.4 nm) and a nominal number of Er ions per nanocrystal of 2.48. It is expected that the Er^{3+} ions are statistically distributed within the $NaYF_4$ crystals following a Poisson distribution with $\lambda = 2.48$. As the nanocrystals have varying numbers of Er^{3+} ions, we expect to see emission counts with levels corresponding to the different number of ions that follows a similar distribution. Trapping was performed for 100 events using a DNH with 32 nm cusp separation, measuring the emission spectrum for each event.

Figure B.5(a) shows the upconversion emission from 640 nm to 680 nm of single

nanocrystals as measured with a 1 s integration time. It can be seen that the emission is separated into discrete levels. We attribute these levels to the discrete numbers of erbium emitters in the nanocrystals, from zero to seven individual active emitters. The integrated emission counts give a clear way to distinguish between the distinct numbers of active erbium emitters. The experiment demonstrated a mean of 1.68 ± 0.17 active erbium emitters per nanocrystal. Compared to the expected mean from the synthesis, this gives a yield of 0.67 ± 0.07 which is consistent with previous findings from our group. [103]

Figure B.5(b) shows the probability distributions of Er emitters per nanocrystal as expected from the synthesis and experimental means. This distribution makes the assumption that all Er^{3+} ions can emit photons. However, it is expected that surface quenching significantly reduces the emission from Er^{3+} ions near the surface of the nanocrystal. [199] A quenched layer of 1 nm leads to quenching of 24% of the Er^{3+} ions in the volume. This seems to be a plausible explanation considering the statistical uncertainty in the experimental results.

The different DNHs were nominally the same and therefore showed the same emission intensity. The final Poisson distribution analysis used data from several different DNHs, each following the same discrete level response.

The emission measurements were collected with a spectrometer with a 1 s acquisition time. This is an improvement by over a factor of 40 compared to previous results from our group which required a 30 s acquisition time and produced even fewer counts. [103] This is consistent with the finding in Section 2 and makes it clear that DNHs can be used to improve the process of isolating single emitters. We believe that this level of enhancement will allow for detecting and isolating single emitters at 1550 nm; however, improvements in the optical setup for that wavelength are required.

Time-to-Trap Analysis

We also measure the trapping time from the APD voltage for the different DNH cusp separations. The analysis of the trapping time has been done previously; [191, 200] here we show that the inverse of the trapping time has a similar dependence as the enhancement which we attribute to the larger trapping region with higher local field intensity.

Figure B.6 shows the trapping rate (inverse of trapping time, Γ) as a function of

cusp separation size. The trapping time was measured from the APD voltage (Figure B.1(f)) and the effect of DNH cusp separation on this factor was evaluated. With both the 16.9 nm and 26.2 nm nanocrystals, the trapping rate for the DNHs with 32 nm average cusp separation was also found to be much greater than other cusp separations. The uncertainty for the trapping time measurements was ± 2 ms. The trapping rate shown in this figure aligns closely with the emission enhancement seen in Figure B.3, with both the fastest trapping and greatest emission enhancement occurring for the 32 nm cusp separation. The 16.9 nm nanocrystals were also trapped faster on average than the 26.2 nm nanocrystals due to their smaller size and correspondingly lower Stokes' drag. In these experiments, the nanoparticle diffuses into the trapping region and the concentration of nanoparticle is maintained constant. Considering the Stokes-Einstein diffusion of 10 nm radius particles spaced by 1 micron in solution (which corresponds to the average side length of the concentration used), the expected time to reach the trap by random diffusion is 10 ms, which is the order of magnitude seen in the experiments. The concentration of the crystals was maintained the same, but the diffusion time and trapping potential size differ for different sized particles, hence 26.2 nm and 16.9 nm particles showed different times to diffuse into the trapping region.

Considering possible differences in the diffusion of nanoparticles for each aperture, multiple experiments for each sample and aperture were performed. The measurements were performed for a minimum of four DNHs in each sample and the measurements were repeated three times for each DNH.

These results demonstrate that samples with more emission enhancement also experience faster trapping, and the intensity of the emission can show how fast a particle can be pulled into trapping. While the emission enhancement and trapping dynamics are separate physical processes, they can be related to one another. It should be noted that for the enhancement seen in this experiment, it is the square of the trapping rate that is related to the emission enhancement as the emission (at 650 nm) is a two-photon process.

In the case of trapping nanocrystals, greater emission enhancement corresponds to greater intensity on the sample to excite it. Having more intensity makes the trapping region larger so the particle needs to travel less distance to get into the trap, resulting in a faster trapping time. Thermophoretic forces may also be contributing to this effect as higher local field enhancement can cause additional heating at the structure which can attract thermophilic nanoparticles to the trap. [193]

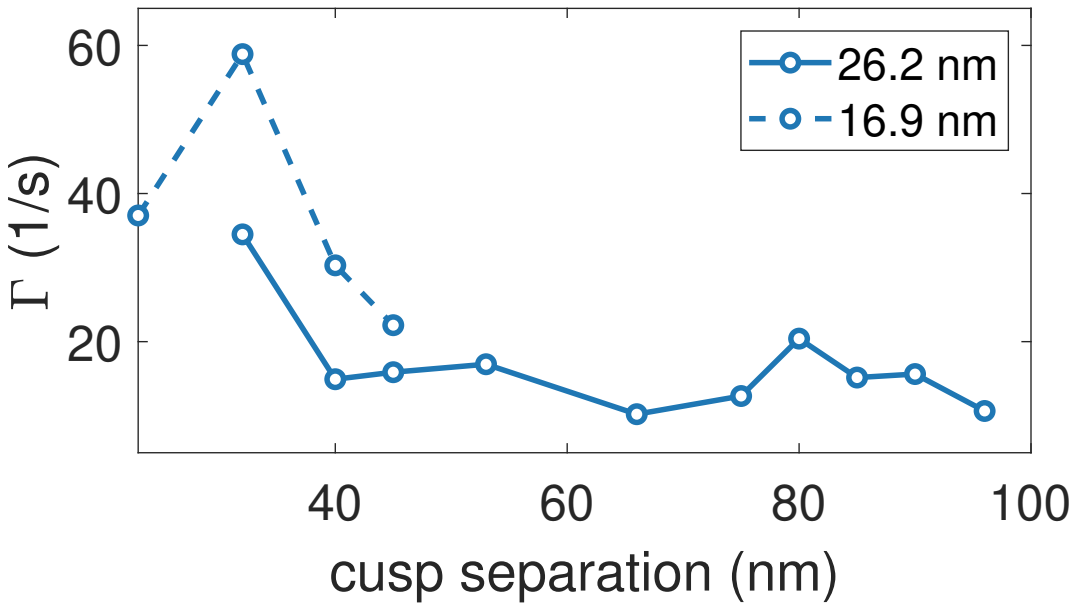

Figure B.6: Investigating the influence of the DNH cusp separation on trapping rate for 16.9 nm and 26.2 nm nanocrystals.

Conclusion

In conclusion, we demonstrated that the plasmonic resonances of a DNH aperture in gold film can be tuned to further enhance the emission of erbium emitters compared to rectangular apertures. The greatest enhancement for Yb–Er-doped nanocrystals was found when using DNHs with 32 nm cusp separation. The emission of single nanocrystals at 400 nm and 1550 nm was also observed for the first time. Using this finding we demonstrated isolating $NaYF_4$ nanocrystals with single active Er^{3+} emitters as determined by the discrete levels of emission. The trapping rate for varying cusp separations was measured and was found to be fastest at the same separations that produced the greatest enhancement. The increased enhancement corresponding to the higher local field intensities increases the effective size of the trap, increasing the trapping rate and giving us an independent method to measure enhancement. These results show that DNHs can be tuned to significantly enhance emission, improving the method to reliably isolate single erbium emitters. This result can be applied to isolate and measure the characteristics of single erbium emitters at 1550 nm. It is a step towards deterministically isolating single photon emitters for future single photon sources at low-loss fiber optic wavelengths. This approach can also be used for looking at other properties of lanthanide based nanoparticles such as photon avalanche at the single particle level. [201]

Methods

Nanocrystal Synthesis and Characterization.

Chemicals. Yttrium(III) chloride hexahydrate (99.99%), erbium(III) chloride hexahydrate (99.995%), ytterbium (III) chloride hexahydrate (99.998%), ammonium fluoride (99.99%), tech grade oleic acid (90%), tech grade 1-octadecene (ODE, 90%), and hexanes were purchased from Sigma-Aldrich. Anhydrous ethanol from Commercial Alcohols, methanol from Caledon, and sodium hydroxide from Bio Basic Canada inc. were used. All chemicals were used as received.

Characterization. Transmission electron microscopy images were obtained using a JEOL JEM-1400 microscope operating at 80 kV. Hexane dispersions of the NPs were drop-cast on a Formvar carbon-coated grid (300 mesh Cu) and air-dried before imaging. Size analysis of NCs from the images was performed digitally by measuring the surface area of at least 1000 particles with the program ImageJ (v. 1.52p) and

calculating the corresponding diameter. X-ray diffractograms with a resolution of 0.0263 °2θ were collected using a PANalytical Empyrean X-ray System with a Cu source (Kα radiation, $\lambda = 1.54060$ Å) operating at 45 kV and 40 mA.

Synthesis (26.2 nm, $NaYF_4$: 18% Yb, 2% Er (102AF18)). To a 100 mL 3-neck roundbottom flask, 240.3 mg $YCl_3\bullet(H_2O)_6$, 77.8 mg $YbCl_3\bullet(H_2O)_6$ and 8.7 mg $ErCl_3\bullet(H_2O)_6$ were added together with 15 mL ODE and 5 mL oleic acid. The mixture was heated to 160 °C under vacuum and kept at that temperature for 30 minutes before cooling to room temperature. Once cooled, a solution of 107 mg NaOH and 152 mg NH_4F in 10 mL MeOH was added dropwise while stirring. The mixture was heated to 65 °C 120 minutes to evaporate the MeOH. The temperature was then raised to 298 ∘C over 20 minutes (11.75 °C/min.) Temperature was kept at 305-307 °C for 90 minutes. The mixture was then cooled, washed with 30 mL EtOH, centrifuged at 1800 g for 10 min, and washed with 30 mL EtOH again before redispersion in 20 mL hexanes. TEM and XRD were performed.

Synthesis (16.9 nm $NaYF_4$: 18% Yb, 2% Er (340AF20)). To a 100 mL 3-neck roundbottom flask, 240 mg $YCl_3\bullet(H_2O)_6$, 80 mg $YbCl_3\bullet(H_2O)_6$ and 8 mg $ErCl_3\bullet(H_2O)_6$ were added together with 16 mL ODE and 5 mL oleic acid. The mixture was heated to 140 °C under vacuum and kept at that temperature for 60 minutes before cooling to room temperature. Once cooled, a solution of 102 mg NaOH and 150 mg NH_4F in 10 mL MeOH was added dropwise while stirring. The mixture was heated to 70 °C 120 minutes to evaporate the MeOH. The temperature was then raised to 280 °C. Temperature was kept at 280 °C for 135 minutes. The mixture was then cooled, washed with 30 mL EtOH, centrifuged at 1800 g for 10 min, and washed with 30 mL EtOH again before redispersion in 20 mL hexanes. The sample was then centrifuged again at 8694 g for 60 minutes and the sediment was redispersed in 10 mL hexanes. TEM and XRD were performed.

Synthesis ($NaYF_4$: 2.48 Er/NP (347AF20)). An $Er(OA)_3$ stock solution was prepared by adding 381 mg $ErCl_3\bullet(H_2O)_6$, 10 mL oleic acid and 10 mL ODE in a 100 mL 3-neck roundbottom flask. The mixture was heated to 140°C under vacuum. After cooling, the mixture was diluted to 0.1×10^{-3} M $Er(OA)_3$. To a 100 mL 3-neck roundbottom flask, 300 mg $YCl_3\bullet(H_2O)_6$ and 0.3 mL 0.1×10^{-3} M $Er(OA)_3$ were added together with 16 mL ODE and 5 mL oleic acid. The mixture was heated to 140 °C under vacuum and kept at that temperature for 60 minutes before cooling to room temperature. Once cooled, a solution of 102 mg NaOH and 150 mg NH_4F in 10 mL MeOH was added dropwise while stirring. The mixture was heated to 70 °C

120 minutes to evaporate the MeOH. The temperature was then raised to 298 °C. Temperature was kept at 298 °C for 135 minutes. The mixture was then cooled, washed with 30 mL EtOH, centrifuged at 1800 g for 10 min, and washed with 30 mL EtOH again before redispersion in 20 mL hexanes. TEM and XRD were performed.

DNH Apertures Fabrication.

Colloidal lithography was used to fabricate double nanohole apertures. Microscope slides were cleaned using plasma for 15 minutes and sonicated for 10 minutes in an ethanol bath. 30 µL of 300 nm 0.01% w/v polystyrene spheres in ethanol drop-coated on the microscope slides uniformly. While the solution dries out through evaporation, the polystyrene spheres attach to the slides. The prepared slides were plasma etched with 5 to 15 seconds difference in etching time to get different cusp separation on each sample. Using 5 nm of titanium as an adhesive layer followed by 70 nm of gold, the samples were sputtered (MANTIS Sputtering System). The sputtered samples were sonicated for 1 minute in a toluene bath to remove polystyrene beads. SEM was performed.

Optical Trapping.

The optical tweezer setup (Figure B.1(d)) consists of a single 980 nm continuous-wave laser (JDS Uniphase SDLO-27-7552-160-LD) which is collimated, filtered, polarized, and expanded, before being focused on the sample with a 100× oil immersion microscope objective (1.25 numerical aperture). This single beam is used for both trapping, and to excite the nanocrystals. A 10× microscope objective is used to collect the light transmitted through the sample which is measured by an avalanche photodetector (Thorlabs APD120A). The polarization of the beam is set by the half-wave plate (HWP) and the linear polarizer (LP). A three-axis sample stage with piezoelectric adjustment aligns the apertures to the beam with 20 nm precision. A 750 nm short-pass filter (Thorlabs FES0750) reduces the trapping beam intensity and a bifurcated fiber splits the signal between two spectrometers, one for visible wavelengths (Ocean Optics QE65000) and one for NIR wavelengths (BaySpec NIRS-0900-1700). The gold DNH aperture samples were attached to #0 coverslips with an adhesive spacer containing 17.6 µL of nanocrystals in hexane with concentrations of 1.3×10^{12} nanoparticles/cm^3, 5×10^{12} nanoparticles/cm^3, and 4×10^{12} nanoparticles/cm^3 for the 16.9 nm, 22.7 nm, and 26.2 nm nanocrystals.

Abbreviations used in Figure B.1(d): APD, avalanche photodetector; BE, beam expander; CCD, charge-coupled device; D, dichroic mirrror; FM, flip mirror; HWP, half-wave plate; LP, linear polarizer; LPF, long-pass filter; Obj, objective lens; OD,

optical density filter; S, spectrometer; SPF, short-pass filter.

Appendix C

Improving Sensitivity of Existing Surface Plasmon Resonance Systems with Grating Coupled Short Range Surface Plasmons

2019, JOSA B, volume 36(8), pp F144-F148

ELHAM BABAEI[1], ZOHREH SHARIFI[1], and REUVEN GORDON[1,*]
1Department of Electrical and Computer Engineering, University of Victoria, Victoria, BC, v8P5C2
*Corresponding author: rgordon@uvic.ca

Received 18 March 2019; revised 11 July 2019; accepted 14 July 2019; posted 17 July 2019 (Doc. ID 362634); published 31 July 2019

Abstract

Here we show that surface plasmon resonance sensors that typically use 760 nm wavelength Kretschmann-Raether coupling to a 50 nm thick gold film can have 3.3 times higher surface sensitivity by using local resonances from periodically arranged short-range modes in the same configuration. Considering shot noise, the resolution

was found to improve by four-fold. This was calculated by matching the design wavelength and minima angle as calculated by rigorous coupled wave analysis, giving a grating period of 250 nm in a 10 nm thick gold film and gap length of 40 nm. Finite difference time domain simulations were used to confirm that the short-range modes correspond to a localized surface plasmon resonances. The present short-range plasmon approach can be used to improve the sensitivity in monitoring biomolecule interactions.

Introduction

Conducting surfaces permit guided waves called surface plasmon polaritons (SPPs), the mathematical solutions of which have been known for over a century [202]. A prism can be used to couple light into these surface waves, matching the wave-vector in the high-index prism to the wave-vector of the surface plasmon [52, 203]. Since the metal is lossy, light is absorbed at the coupling condition and this leads to a dip in the reflection [203].

The SPP is exponentially bound to the surface, which gives good sensitivity to changes in refractive index near the surface. This is the premise behind the commercialized surface plasmon resonance (SPR) biosensors [204]. These commercial systems have been engineered with consideration of many factors: the light source wavelength, the light source type (LED vs. laser), the metal type, the metal thickness, the detector type (single channel vs. detector array), the data acquisition (dynamic range, analogue to digital conversion and acquisition time) and cost. With all of this engineering already in place and many such machines in laboratories around the world, it is interesting to consider leveraging the existing commercial SPR platform while using a more sensitive sensor chip.

One potential direction to obtain even greater surface sensitivity is to use short-range surface plasmon (SRSP) modes [205, 206]. In particular, insulator-metal-insualtor (IMI) structures permit SRSP modes that become more tightly confined to the surface as the thickness of the metal is reduced. This leads to greater surface sensitivity. Here we consider the use of these SRSP modes in sensing applications while retaining the popular prism coupling configuration.

The SRSP modes have a larger propagation constant than the usual surface plasmon polaritons. Therefore, to couple into these modes while retaining the same Kretschmann geometry as the usual 50 nm thick gold film, we employ a periodic

structure with localized surface plasmon (LSP) resonances. Another feature of these modes is that they are more lossy; therefore, it is expected that their reflection dip will broaden upon coupling.

In this paper, we find a design for SRSP sensing using a rectangular stripe grating and a 10 nm gold film. The 10 nm gold is thick enough to allow for continuous films with standard deposition techniques. Using rigorous coupled wave analysis, we find that the surface sensitivity of these films to an adlayer is 3.3 times higher in terms of angle units and the resolution is improved by four-fold, while operating in the same range as commercial SPR systems. Therefore, we believe these chips may be used for more sensitive SPR sensing in the near future.

Design

Standard SPR Sensing

Figure C.1 shows the schematics of typical surface coupling for a conventional SPR and the proposed IMI-grating structure. A metal film is confined between two dielectric layers. Incident light couples to the SPP in case of SPR. Surface resonance only happens when incident angle toward the structure is greater than the critical angle. The parallel component of incident light should match the surface plasmon wave-vector of the metal. Minimum reflection occurs when the energy of the incident photon is transferred to surface plasmon wave.

Figure C.1(a) shows the standard configuration for uniform 50 nm gold film. Uniform films are suitable for SPPs of a single surface. Figure C.1(b) shows the proposed scheme with periodic gold structure on glass. This structure allows decreasing gold thickness to 10 nm which increases the confined coupled field significantly.

For conventional SPP copuling, the light is angled in the prism to match the SPP wave-vector. The SPP wave-vector is given by:

$$k_{\mathrm{SP}} = k_0 \sqrt{\frac{\epsilon_m \epsilon_d}{\epsilon_m + \epsilon_d}} \tag{C.1}$$

where $k_0 = 2\pi/\lambda$ ($\lambda = 760$ nm), ϵ_m is the relative permittivity of the metal, ϵ_d is the relative permittivity of the adjacent dielectric (in this case water). The wave-vector in the prism is given by:

$$k_{\text{prism}} = k_0 n_{\text{prism}} \sin\theta \tag{C.2}$$

where θ is the angle of incidence in the prism and n_{prism} is the prism's refractive index. In this case the SPP coupling occurs where $k_{\text{SP}} = k_{\text{prism}}$.

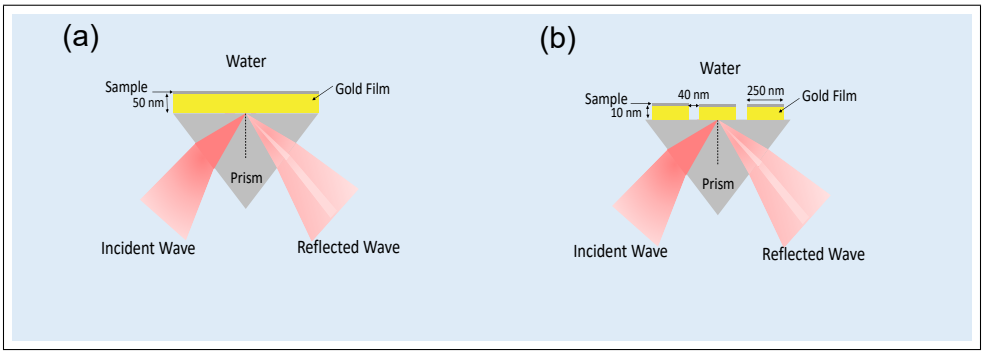

Figure C.1: (a) Prism coupled SPR structure for 50 nm gold film (b) Modified structure for 10 nm gold film using a grating.

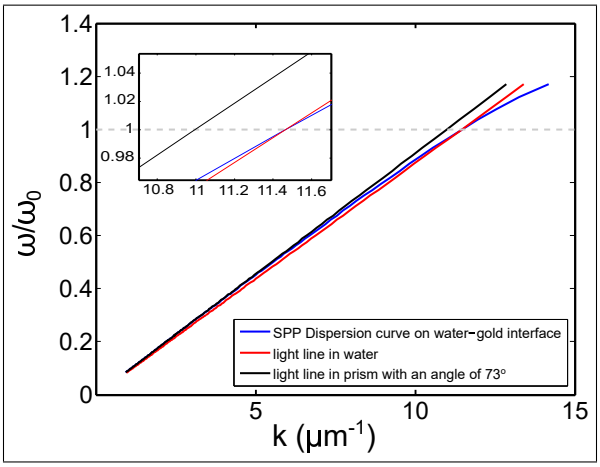

Figure C.2: Dispersion for coupling to surface plasmon at water-gold interface when incident from glass-gold side of the prism. The intersection point is at 73°, which gives a dip due to losses in the SPP.

Figure C.3 shows the reflection of a 50 nm gold film when incident through a prism as a function of incident angle. The refractive index of the prism is 1.5 and the top layer is considered to be water with refractive index 1.33. It is clear from this figure that the reflection dip of optimal SPP coupling occurs at around 73°, as expected from the coupling analysis above. (Of course, rigorous coupled wave analysis, or RCWA, is not required for this analysis, since standard transfer matrix

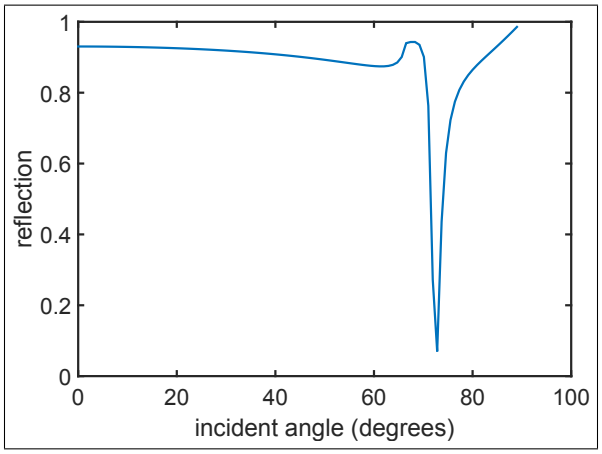

Figure C.3: Reflection from a 50 nm thick gold film on glass with a water top layer for different incident angles.

theory is applicable to this uniform layer). It is noted that surface plasmon dispersion is for a semi-infinite surface, and so the treatment of using wave coupling through the film is approximate, whereas the RCWA is not [207].

SRSP Grating-Assisted Coupling

The propagation constant of a surface plasmon wave on a thin metal film with thickness of h which is bounded by two dielectric media, with subscripts 1 and 3, is determined by following equations [208]:

$$\tanh p_m h(1 + s_1 s_3) = -(s_1 + s_3) \tag{C.3}$$

$$s_1 = \frac{p_1}{p_m}\frac{\epsilon_m}{\epsilon_1} \tag{C.4}$$

$$s_3 = \frac{p_3}{p_m}\frac{\epsilon_m}{\epsilon_3} \tag{C.5}$$

$$p_1^2 = \beta^2 - k_0^2\epsilon_1 \tag{C.6}$$

$$p_m^2 = \beta^2 - k_0^2\epsilon_m \tag{C.7}$$

$$p_3^2 = \beta^2 - k_0^2\epsilon_3 \tag{C.8}$$

where β is the wavevector of the SRSP and k_0 is the free-space wavevector.

Using these equations, we find that the effective index of the SRSP is 2.58. From this, one can couple to the SRSP by using a periodic structure period of 636 nm to match the wavevector of light in the prism to that of the SRSP using the equation:

$$k_{\text{prism}} + K_G = \beta \tag{C.9}$$

where:

$$K_G = \frac{2\pi}{\Lambda} \tag{C.10}$$

with Λ being the grating period and β is the propagation constant of the SRSP.

We attempted this configuration, and found that coupling was weak (a dip in the reflection of around 30 %). As a result, we considered the possibility of using stronger resonances found in LSPs in an array format.

LSP Coupling

LSPs are supported by finite metal nanostructures. We first employed RCWA to study periodic LSP structures for prism coupling. RCWA is typically used to study the interaction of an electromagnetic wave with a surface plasmons on a metallic relief grating. RCWA is also reliable approach to determine dips in reflection as a function of wavelength and angle [209, 210].

Figure C.4 shows reflection spectrum for different structures using RCWA method. p is the period of the grating and g is the size of the gap. As shown in the figure for grating period of 250 nm and gap length of 40 nm, the dip occurred for 760 nm incident light, which is the operating wavelength desired at this angle of incidence.

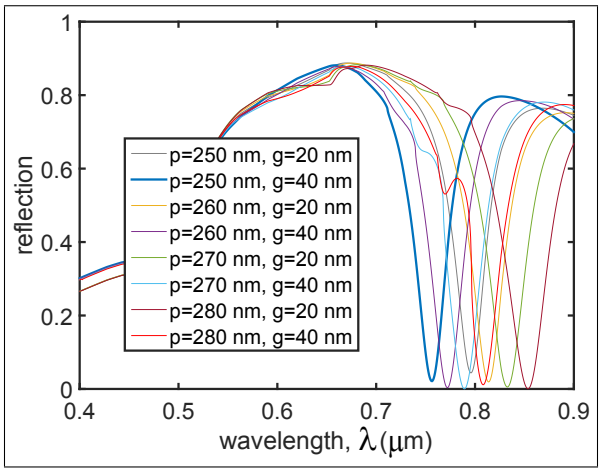

Figure C.4: Reflection spectra periodic structure supporting SRSP mode with an incidence angle of 73°. The period, p, and gap g were varied in each curve to find the case which is most closely matched to the operating wavelength of 760 nm.

To verify that the origin of this dip is from the LSP resonance, we performed finite-difference time-domain (FDTD) simulations of an isolated structure using the commercial package by Lumerical. We use a grid size of 0.2 nm in the direction perpendicular to the layers and 1 nm in the direction of SRSP propagation. The total domain simulated was 280 nm by 5.75 μm, and bounded by perfectly matched layers. The glass and gold layers were taken from the Palik database. The gold thickness was 10 nm, and its length was 250 nm. A dipole source was placed at one end of the rectangular gold structure and the field intensity was monitored at the peak at the other end of the structure.

Figure C.5 shows the electric field intensity at the end of the gold nanostructure, with a clear peak at the desired operation wavelength of 760 nm. Figure C.6 shows

the field intensity at the opposite end of the rectangular structure, with clear edge enhancement, but also strongly confined light at the metal surface.

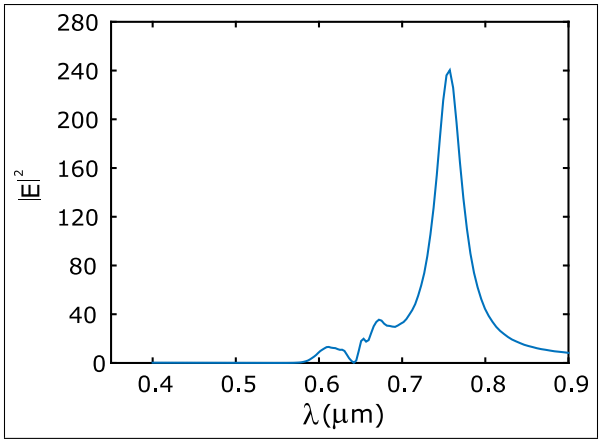

Figure C.5: Electric field intensity monitored near a 10 nm thick and 250 nm long rectangular gold structure on glass with a water surrounding. The peak in the LSP resonance is at 760 nm as desired for the SPR sensor configuration.

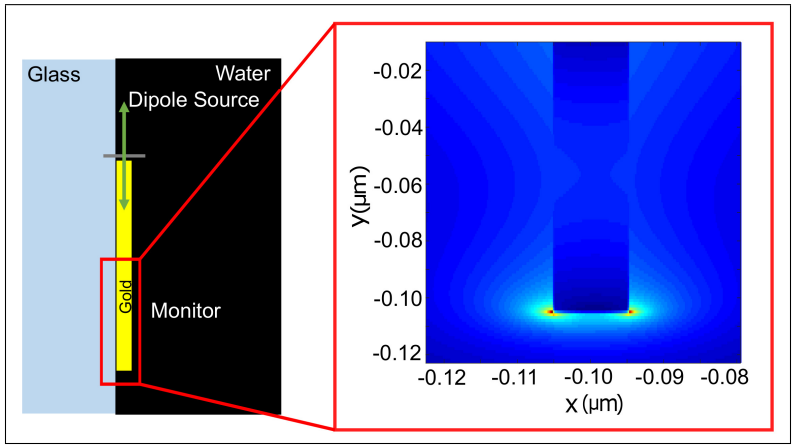

Figure C.6: The field intensity distribution at the LSP resonance.

Sensing Performance

Sensitivity Calculations

To investigate the improved sensitivity of the resonant periodic structure supporting the SRSP, a 1 nm adlayer is applied on the top of the gold with refractive index 1.5. Figure C.7 shows the reflection for different angles of incidence, both for a

50 nm thick gold film and for the 10 nm thick periodic structure. In each figure, the reflection is plotted for the bare structure and the structure with an adlayer. As demonstrated in the inset figures, the 10 nm gold periodic structure has 3.3 times higher sensitivity than for 50 nm continuous gold. (Note, that restricting the adlayer to the top surface is done for analytic simplicity, and may be achieved in practice by masking the side-walls).

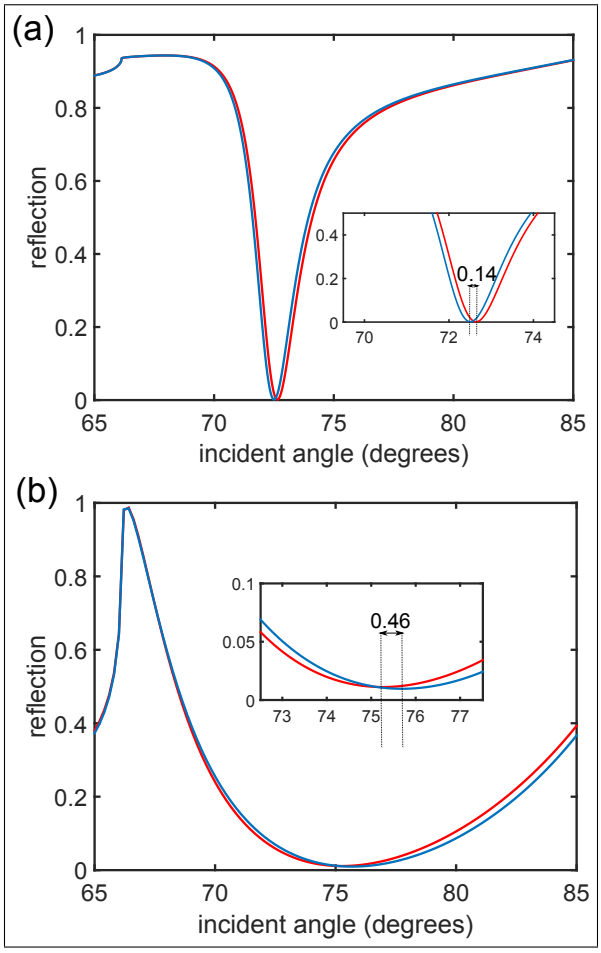

Figure C.7: Sensitivity calculations for (a) a 50 nm thick gold film with a 1 nm adlayer, and (b) a 10 nm thick gold film with 290 nm period and 250 nm length of each gold segment and a 1 nm adlayer. The insets are shown to clearly depict the angle shifts with the adlayer in each case.

Resolution Calculations

To compare the resolution of the gold film with the thickness of 50 nm and structured film with 10 nm thickness, we added shot noise to the digitized reflection. The digiti-

zation used 1024 bins for angle of incidence and 4096 bins for reflection intensity. We fit the noisy response to various adlayer index values (thickness 1 nm), and repeated the procedure to ensure a suitably averaged response. In this way, the resolution was determined to be 8×10^{-5} RIU/nm for 50 nm gold and 2×10^{-5} RIU/nm for 10 nm gold SRSP structure.

Discussion

It is clear from the analysis presented that the 10 nm thick gold film with a stripe grating structure has 3.3 times higher sensitivity and 4 times improved resolution.

Many have suggested that having a narrower peak will improve the performance of SPR detection systems because it allows for more precisely determining the position of the reflection dip. For this reason, a figure-of-merit of wavelength shift divided by peak width is often used [211]. There are arguments to suggest that this is not always true. Consider the extreme case where the peak is much narrower than even one pixel spacing of the detector array, then there is no change in the signal detected for a sub-pixel sized shift with an adlayer. Therefore, having a very narrow peak can give no signal at all, even though the usual figure-of-merit is huge. Here, we have done the resolution calculations and found that the broader peak actually allows for improved resolution because the signal is supported by a greater number of bins (therefore, the noise in each bin can be averaged to reduce the overall noise). This noise analysis focuses on shot noise, where the noise is proportional to the square root of the detected counts. A well-engineered system will be shot noise limited [212]. Low cost fabrication of these grating structures is also an important consideration. We believe that these structures can be readily manufactured at low cost using existing template stripping approaches [213].

It is possible to push the sensitivity even higher by looking at ultra-thin gold films. While 10 nm continous gold films are commercially available, special methods can be used to create continuous films down to 5.4 nm that are stable under ambient conditions [214].

We are also aware of extremely high sensitivity demonstrations using nanorods (and similar works) [215]. While it is interesting to consider such approaches further, there are potential advantage of our design. We have already mentioned that our design is compatible with existing SPR machines, and may be readily mass produced using template stripping or other similar approaches. In addition, our design uses a

mainly flat surface and so fouling that can occur with highly structured surfaces is not as big a concern.

Conclusions

In this work, we consider a perioidic SRSP sensor design that is compatible with existing commercial SPR sensors. The SRSP works by coupling to the LSP resonance of a rectangular structure. The design shows a 3.3 times higher surface sensitivity, which is promising for high-performance detection applications (such as low index contrast materials or sub-monolayer absorption). A noise analysis shows that the resolution also improves in the SRSP design.

Appendix D

Accessible High-Performance Double Nanohole Tweezers

2022, Optics Express, volume 30(3), pp 3760-3769

Reprinted with permission from Optics Express, The Optical Society of America.

GHAZAL HAJISALEM[1,2,4], ELHAM BABAEI[1,2,4], MICHAEL DOBINSON[1,2], SHOHEI IWAMOTO[1,2], ZOHREH SHARIFI[1,2], JON EBY[1,2,4], MARIE SYNAKEWICZ[3], LAURA S. ITZHAKI[3], AND REUVEN GORDON[1,2,*],

1Department of Electrical and Computer Engineering, University of Victoria, Victoria, British Columbia, V8P 5C2, Canada
2Centre for Advanced Materials and Related Technology (CAMTEC), University of Victoria, 3800 Finnerty Rd, Victoria, BC, V8P 5C2, Canada
3Department of Pharmacology, University of Cambridge, Tennis Court Road, Cambridge, CB2 1PD, United Kingdom
4Co-first authors with equal contribution
*rgordon@uvic.ca

Received 26 Oct 2021; revised 9 Jan 2022; accepted 11 Jan 2022; published 20 Jan 2022

Abstract

Nanohole optical tweezers have been used by several groups to trap and analyze proteins. In this work, we demonstrate that it is possible to create high-performance double nanohole (DNH) substrates for trapping proteins without the need for any top-down approaches (such as electron microscopy or focused-ion beam milling). Using polarization analysis, we identify DNHs as well as determine their orientation and then use them for trapping. We are also able to identify other hole configurations, such as single, trimers and other clusters. We explore changing the substrate from glass to polyvinyl chloride to enhance trapping ability, showing 7 times lower minimum trapping power, which we believe is due to reduced surface repulsion. Finally, we present tape exfoliation as a means to expose DNHs without damaging sonication or chemical methods. Overall, these approaches make high quality optical trapping using DNH structures accessible to a broad scientific community.

Introduction

Nanohole optical tweezers have been broadly used to investigate nanoparticles, starting with early works on circular and rectangular apertures [7, 114, 141, 216, 217]. Double nanohole (DNH), coaxial and bowtie aperture and similar shaped aperture optical tweezers have been used in the analysis of particles smaller than 20 nm [7, 123, 124, 218, 219, 220, 221, 222, 223, 224], including optical emitters and quantum emitters [11, 103, 122, 225, 226], magnetic particles [192], DNA [227], proteins [111, 196, 228, 229, 230, 231, 232]. These apertures have also been used in protein-DNA interactions [9], protein-small molecule interactions [195, 228, 233], protein-antibody interactions [234, 235], protein-protein interactions [188], and to study protein vibrations [236].

The benefit of using a DNH aperture is to have a high field enhancement localized in the gaps as small as 10 nm [188]. Most of these past works have used top-down methods, such as focused ion beam, to fabricate the apertures [9, 193]. Recently, we explored the use of colloidal lithography to create DNH apertures and used scanning electron microscope (SEM) to find them [14]. This still limits the use of the technique to those with SEM facilities, and introduces an extra registration step, where the SEM has to be compared with the microscope image using some fiduciary markers.

To make DNH aperture trapping more accessible, here we introduce a polarization

and transmission dependence technique to localize DNHs on a substrate, as well as determine their orientation. We also characterize other aperture clusters and singles with this approach. We explore the use of low-repulsion substrates for improved trapping efficiency and tape-fabrication for gentle exposure of high-quality apertures.

Polarization Dependent DNH Localization and Orientation

Figure D.1(a) shows a schematic of an optical tweezer setup, where a continuous wave (CW) diode laser beam was collimated, expanded, and focused through a 100× microscope objective (1.25 NA) into a nanoaperture. The transmitted signal was collected by a 10× microscope objective (0.25 NA) and measured by an avalanche photodiode (APD – Thorlabs, APD120A). The reflected laser beam and the transmitted LED light were directed to a charge-coupled device (CCD) camera. Figure D.1(b) shows a CCD image of the aperture sample while the LED was on and the laser was off, and Figure D.1(c) shows a CCD image of the sample while both the LED and laser were on and the laser beam was aligned and focused into an aperture.

Nanoapertures in gold on glass substrate were fabricated by using the colloidal lithography method [14]. Briefly, a 10 μL solution of 300 nm polystyrene nanospheres in ethanol was drop-coated on a glass microscope slide. Then, 5 nm titanium adhesion layer followed by a 70 nm gold film was deposited on the sample using a sputtering system (Mantis). The Au-Ti coated sample was sonicated for 5 minutes in ethanol to remove the polystyrene nanospheres and to reveal the nanoapertures on the film. Variations in the size of polystyrene spheres and the etching time results in varying of gap sizes and apertures diameters. Plasmonic nanoapertures on plastic substrate were fabricated following the the same process as described above but using polyvinyl chloride (PVC) slides instead of glass microscope slides (for SEM images see the Supplementary Material). Further, the omission of the sonication step in lieu of the tape-removal is discussed below.

The colloidal lithography method resulted in formation of varying of nanohole configurations, i.e. single, double, and variable clusters nanoholes. In this method, dominant nanoapertures structures, average density of nanoapertures, diameter size of apertures and their separation gap size of DNHs on a sample were controlled through the fabrication process [14]. However, location and number of nanoapertures on a

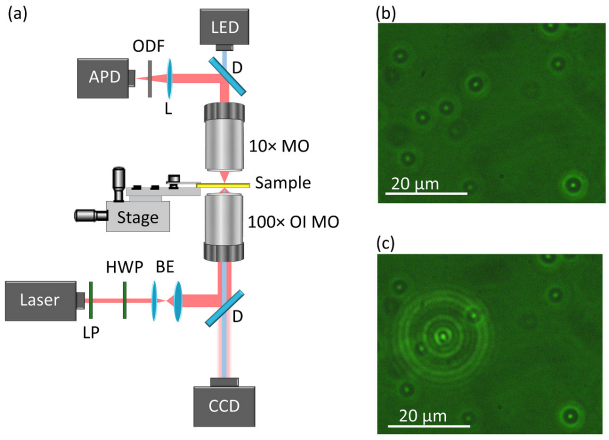

Figure D.1: Experimental optical trapping setup. (a) Schematic of an optical tweezer setup: linear polarizer (LP), half-wave plate (HWP), beam expander (BE), shortpass dichroic mirror (D), 100 × oil immersion microscope objective (100 × OI MO), piezo stage (stage), 10 ×microscope objective (10 ×MO), lens (L), optical density filter (ODF), and avalanche photodetector (APD). (b) A CCD image of a sample with nanoapertures when the LED light was on and the laser was off. (c) a CCD image of the sample when both the LED light and laser were on and the laser beam was focused into an nanoaperture. Transmitted LED light from nanoapertures varied for different shapes and resulted in varying of brightness of nanoapertures in the CCD image.

sample could not be controlled through the fabrication process (see the Supplementary Material) and this resulted in formation of varying of nanoaperture structures over the sample.

To find a DNH aperture, here we used a combination of CCD camera images and polarization dependent transmission of the laser beam, not only to align the laser beam with a nanoaperture, but also to distinguish between different nanoaperture structures on a sample. In addition, the transmitted LED light from nanoapertures varied for different nanoaperture structures, resulting in varying their brightness in the CCD image (see Figures D.1(b) and (c)).

Figures D.2(a-d) show CCD images for varying of nanohole configurations and their transmitted signals (Figures D.2(e-h)) measured in the APD. We can rapidly identify DNH candidates by the white light transmission imaged on the CCD. For example, Figure D.2(a) shows a dimmer spot that was a single nanohole (determined later by SEM that is shown in the inset of the Figure D.2(a)), whereas Figure D.2(b) shows a brighter spot that was a DNH. By ignoring all the dimmest apertures, we can

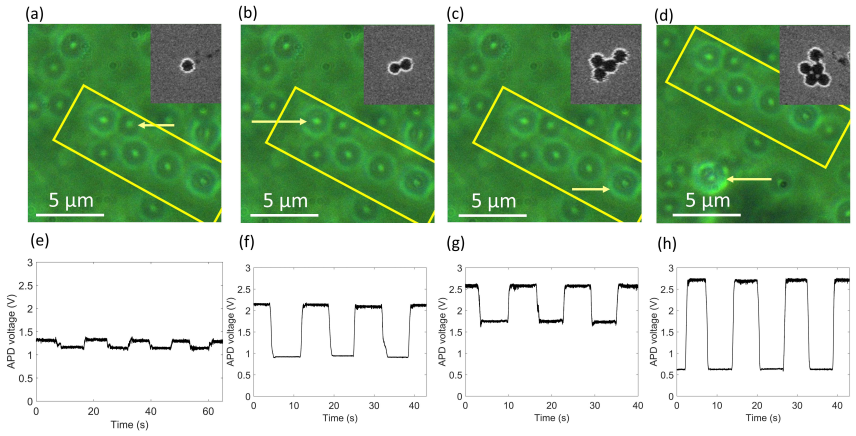

Figure D.2: Identifying DNHs and other nanohole configurations on a sample. (a-d) CCD images of white light transmission of single, double and varying of cluster apertures. In these images, the same area was artificially marked with yellow contours and an aperture of interest was shown with a yellow array. Brightness of apertures were varying depended on nanoholes configuration: (a) single nanoholes (SNHs) were the dimmest structures, (b) DNHs were brighter than SNHs but dimmer than clusters, (c and d) clusters were the brightest apertures among varying of configurations. Inset of figures (a-d) show SEM images of the marked nanoaperture (full SEM image is shown in the Supplementary Material. (e-h) Maximum and minimum polarization dependence of the laser transmission of an aperture of interest, marked in (a) to (d) and measured with the APD: (e) polarization dependence of the SNH shown in (a) using 4.1 mW. (f) Polarization dependence of the DNH shown in (b) using 4.1 mW incident laser. (g and h) Polarization dependence of the clusters shown in (c) and (d), using 4.1 mW and 6.8 mW. The HWP was switched between maximum and minimum transmission values in the plots (e-h)

rule out single apertures. The beam diameter is $\sim$1 μm, and so we can safely irradiate only one structure at a time as long as it is separated by more than a few microns. Figure D.12 of the Supplementary Material shows more details of identifying DNH by using CCD images and changing the distance of the focusing microscope objective to the substrate. Next we use polarization dependence of the laser transmission. DNH and clusters show a polarization dependence (generally) as shown in Figures D.2(f-h). The small polarization dependence of the single nanohole is a combination of slight anisotropy and some polarization dependence in the optics setup. Among Figures D.2(f-h), the DNH could be reliably found by the polarization dependence and intensity. It should be noted that the HWP was switched between maximum and minimum transmission values in these plots.

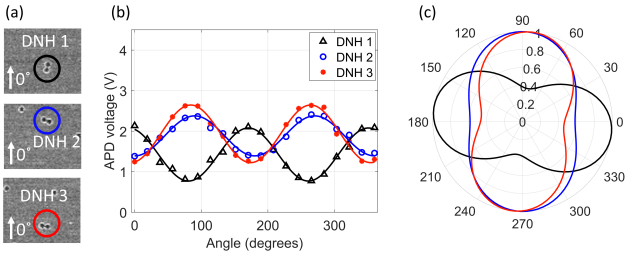

Figure D.3: Polarization dependence of the laser transmission of DNHs. (a) SEM images of DNHs with their axes normal or parallel in respect to each other. Full SEM image is shown in the Supplementary Material. (b) Parallel DNHs show similar polarization dependence of the laser transmission, and DNHs with normal axes in respect to each other show opposite transmission response of the laser beam. The laser polarization direction was rotated by using a HWP in front of the lasrt output, starting from the zero-order line of the HWP. (c) Polar plots of normalized transmissions for DNHs shown in (a and b).

Figure D.3 shows that the orientation of the DNHs could be determined by the detailed polarization analysis. Maximum transmission through a DNH occurs when the laser polarization is along the short axis of the DNH [237]. In these measurements, the polarization direction of the laser beam was rotated in steps by a HWP in front of the laser, starting from the zero-order line of the HWP. The transmitted signal through an aperture was measured by the APD. Figure D.3(a) shows SEM images of three DNHs with parallel or normal orientations in respect to each other (the full SEM image is shown in the Supplementary Material). We observed that DNHs with parallel axes had similar polarization responses, while DNHs oriented normal in respect to each others showed orthogonal polarization response (Figure D.3(b)). Figure D.3(c) shows polar plots of normalized polarization dependence of the DNHs in (a) and (b). Normalized transmission in the polar plots was obtained by dividing transmission values by the maximum transmission value.

Figures D.4 and D.5 show that this applies to triangular (three holes) and diamond (4 holes) clusters as well. These apertures could also be located and oriented.

Figure D.4 shows the polarization dependence of the transmission laser beam through two triangular clusters with different orientations. Figure D.4(a) shows SEM images of the triangular apertures and Figsure D.4(b) and (c) show the transmitted signals and the normalized polar plots of the transmitted signals through the triangular apertures shown in (a). We also trapped 20 nm polystyrene nanospheres by using triangular apertures showing similar behavior as DNHs (see the Supplementary

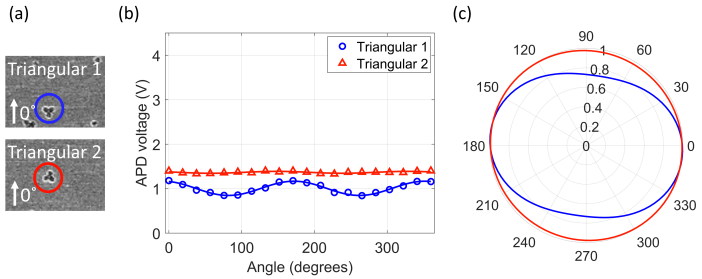

Figure D.4: Polarization dependence of triangular clusters with different orientation. (a) SEM images of two triangular clusters (labeled as Triangular 1 and Triangular 2) on a sample. (b) Polarization dependence of transmission through the aperture was obtained by rotating the HWP in front of the laser and measured the transmission signal in the APD. (c) Polar plot of the normalized transmission signals shown in (b).

Material).

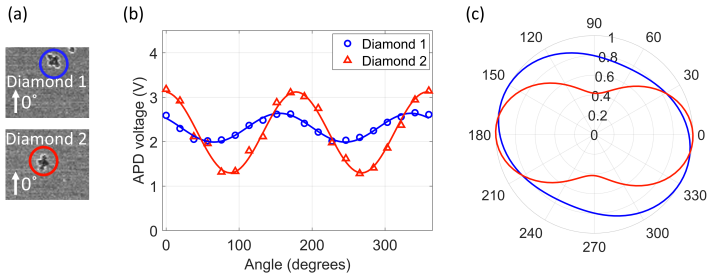

Figure D.5: Polarization dependent response of two clusters with diamond configuration on a sample. (a) SEM images diamond apertures (also see the Supplementary Material), marked with yellow contours. (b) Polarization dependence of the transmission laser beam of the diamond apertures shown on (a). (c) Polar plots of normalized transmission of (b).

Figure D.5(a) shows SEM images of two diamond configurations clusters with different orientations in respect to each other. Figures D.5(b) and (c) show the polarization dependence and normalized polarization dependence of the transmission signals through the apertures. These show that diamond clusters had polarization dependence while they had higher transmission that DNHs.

We performed finite-difference time-domain simulations of the triangular structure to confirm that the transmission shows negligible polarization dependence, as shown in Figure D.14 of the Supplementary Material. The polarization of the DNH has been established by past studies [237], and the diamond structure shows more transmission and a stronger polarization at this wavelength and so it can be safely distinguished

from the DNH.

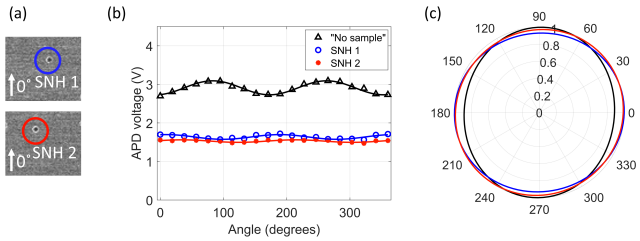

Figure D.6: Polarization dependent response of SNHs and polarization rotation of the laser beam without any sample (labeled as "No sample". SNHs showed the same polarization responses and also the same response as the laser beam without any sample. We believe this mainly comes from the polarization dependence of the setup.

Figure D.6 shows that a SNH show a slight polarization dependence but these are all the same and also the same as not having any sample there (labeled as "No sample"). Therefore, we believe this is mainly coming from the polarization dependence of the setup. The measurements were calibrated by using the "No sample" data to correct the polarization effects from the setup without a sample. The degree of polarization was 0.074 ± 0.03 for single holes, 0.41 ± 0.06 for doubles, 0.070 ± 0.03 for triangular shaped, and 0.23 ± 0.1 for diamond shaped, where the number of samples probed was typically 3. These values are not overlapping. This shows clearly that the different apertures can be identified based on degree of polarization and on maximum transmission. Also, the maximum amplitude of the signal, normalized to the incident laser power, was 0.16 ± 0.03 V/mW for single holes, 0.24 ± 0.04 V/mW for doubles, 0.14 ± 0.02 V/mW for triangular shaped, and 0.32 ± 0.04 V/mW for diamond shaped.

Improved Trapping by Substrate Modification

Figure D.7 shows trapping events of 20 nm polystyrene nanospheres with a DNH in gold on glass substrate (Figure D.7(a)) and with a DNH in gold on a PVC plastic substrate (Figure D.7(b)). We used DNHs with similar gap size of ∼50 nm and aperture diameter of ∼215 nm in 70 nm gold film on glass and plastic substrates (SEM images are shown in the Supplementary Material). As demonstrated in previous works by our lab, trapping was performed in an inverted configuration with the gold

sample in contact with the solution by an adhesive microwell consisting of a spacer on a #0 microscope coverslip filled with the solution [111, 188, 14].

Trapping a particle in a DNH aperture resulted in increasing the transmission, observed by a jump in the APD signal. We performed the trapping on 6 different nanoholes for plastic and glass substrates and found that the stiffness was 0.043 ± 0.007 fN/(nm·mW) for plastic and 0.012 ± 0.002 fN/(nm·mW) for glass, indicating that the stiffness is increased by a factor of 3.6 for plastic [191]. The stiffer trapping offered by the plastic substrate allows for lower laser powers to be used which reduces the heating of the trap. This is an important consideration for trapping biological materials which can be sensitive to the local heating [228]. Additionally, when particles were trapped the level of noise also increased. Trapping on glass substrate showed on average a 5% jump of the APD signal, whereas trapping on plastic substrate showed on average a 10% jump in transmission signal, suggesting that the particle was positioned closer to the maximum intensity of the beam, causing increased light transmission through the aperture. Furthermore, the level of noise for the plastic trapping was less than that of the glass trapping indicating that there was less movement of the particle, and that trapping with a plastic substrate was more stable than with glass. Also, we observed that the initial laser power required to trap polystyrene with glass substrate was ∼5.8 mW, while for the plastic the initial required power was ∼1.4 mW.

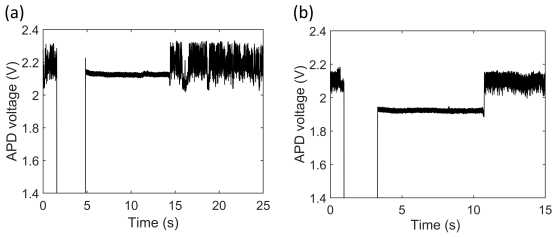

Figure D.7: Trapping event of 20 nm polystyrene indicated by the increase in transmission and signal variation (a) at 15 s with a DNH in gold on a glass substrate, and (b) at 12 s with a DNH in gold on a PVC plastic substrate.

Figure D.8 shows the mean APD voltage of trapping events for varying the incident laser power, along with the level of noise characterized by the standard deviation (STDev), for glass and plastic substrates. With the plastic substrate, it was possible to keep a 20 nm polystyrene in trapping for laser powers as low as ∼0.6 mW, whereas for the glass substrate the minimum laser power needed to keep

the particle in trapping was ∼4.2 mW. Figure D.18 of the Supplementary Material shows the transmission measurement data. This shows changing the substrate from glass to plastic reduced the minimum trapping power by 7 times and improved the trapping ability, which we believe is due to reduced surface repulsion because a glass substrate will charge strongly in water [238, 239, 240]. Since glass is much more hydrophilic than PVC plastic [241], glass ionizes easily in water[238], which increases the bulk concentration of ions surrounding the glass surface, contributing to a stronger repulsion force [242, 243].

While we primarily show data for trapping polystyrene nanospheres, one of the main applications of this technology is trapping biological materials [227, 111, 228, 229, 230, 196, 231, 232, 195, 9, 233, 234, 235, 188, 236]. As a proof of concept, proteins were also successfully trapped with the plastic and glass substrates (see the Supplementary Material).

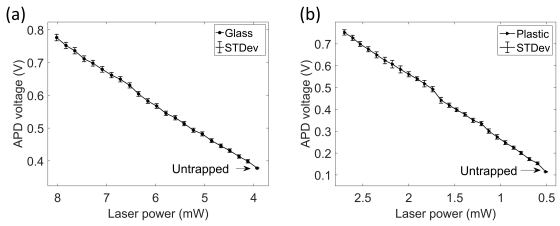

Figure D.8: The mean APD voltage of trapping 20 nm polystyrene for varying the incident laser powers. (a) Trapping with a DNH in gold on a glass substrate, and (b) trapping with a DNH in gold on a plastic substrate, with the STDev indicating the width of the trapping signal. Each measurement was conducted by decreasing the incident laser power while the particle was still trapped. The incident laser power was decreased until it was too low to keep the particle in trapping site and particle was released.

Tape Exfoliation

Figure D.9 shows the fabrication process of DNH apertures using the colloidal lithography [14] by using the tape-removal of nanoparticles instead of the sonication step. The original colloidal lithography method used sonication to remove the polystyrene nanospheres, but it was common for the metal film to begin to detach from the surface before all the nanospheres are removed. Here we used Scotch tape to fully exfoliate the polystyrene nanospheres without damaging the gold surface. In this

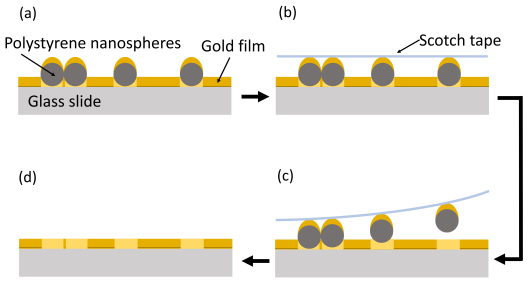

Figure D.9: An illustration of fabrication process using tape exfoliation to remove nanospheres and reveal apertures: (a) a titanium adhesion layer following by a gold film was deposited on top of polystyrene nanospheres on a glass substrate, (b) a tape was applied to a small area on the surface, (c) the tape was gently removed from the sample resulted in pulling away the polystyrene nanospheres, and (d) revealing the nanoapertures on the gold film.

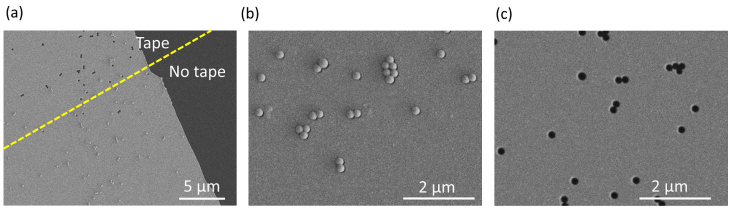

Figure D.10: Nanopaertures fabricated by tape-removal method. (a) An SEM image of an area on the surface where a tape exfoliation was applied and an area without applying the tape. (b) An SEM image of the surface before the tap-removal, and (c) an SEM image of the surface where the tape exfoliation was applied.

method, tape was applied to a small area on the surface and then gently removed to pull away the polystyrene spheres, this step was repeated until the desired area has been exfoliated, taking care not to cover the same area multiple times. This was then followed by washing in ethanol. Care was taken to apply the tape to a sufficiently small area to reduce the chance of adhering to the gold. Figure D.10 shows SEM images of the apertures fabricated by using the tape exfoliation process. Here we used tape to fully exfoliate the 200 nm polystyrene nanospheres without damaging the gold surface. The tape gave more uniform removal of spheres than sonication and the nanoparticles were reliably removed, revealing high quality apertures without damage that can come from sonication or using chemicals. The tape exfoliation may become more challenging for smaller spheres which is a possible limitation of this approach; however, we did not investigate this fully in this work.

Conclusion

We have demonstrated a way to identify the location and orientation of DNHs in-situ, without the need for SEM or other complicated processes. This makes the approach much more accessible without ready access to such facilities, requiring only the use of an evaporator, as well as eliminating time-consuming characterization and registration steps.

We have also improved the trapping by switching the substrate from glass to PVC, which reduces repulsion in aqueous environments and reduces the minimum trapping power by 7 times. A further improvement in the aperture quality is obtained by using tape exfoliation instead of sonication in ethanol.

We believe that this low-cost and high-quality approach to DNH trapping will enable greater adoption of the technique by the biophysics and quantum emitter communities. In biophysics, the emphasis can be shifted to protein characterization and interactions studies rather than fabrication and characterization of apertures.

Suplementary Materials

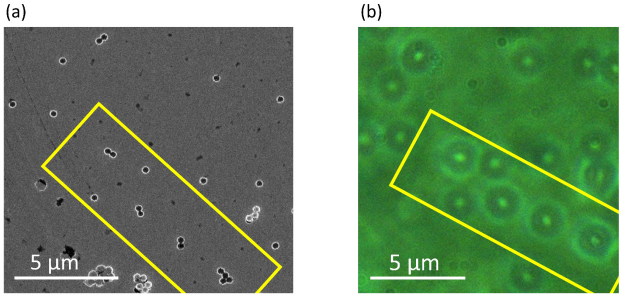

Figure D.11: (a) An SEM image, and (b) a CCD image of the sample shown in the Figure 2 of the main text.

Scanning electron microscopy (SEM) was used to characterize the structures analyzed in this work and provide a reference for constellation mapping of the sample when observed in the CCD camera. Figure D.11 shows an SEM image and a CCD image of the sample shown in the Figure D.2 of the main text. The same area in both images were artificially marked with yellow contours.

Figure D.12 shows an SEM image of a sample and three CCD images of the same sample with three distances of the 100× microscope objective from the surface of

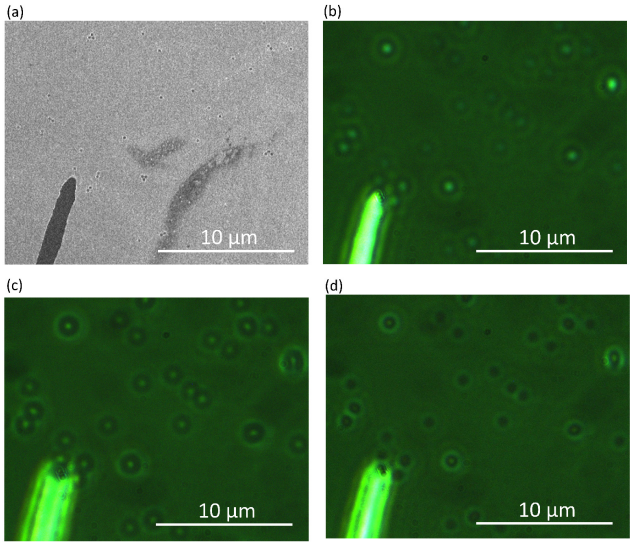

Figure D.12: Distinguishing between varying of apertures by varying the distance of the 100× focusing microscope objective from the surface of a sample. (a) An SEM image of the sample with an scratch marker on it. (b-d) CCD images of the same sample with the microscope objective adjusted (b) focused on the cover glass, (c) focused on top of apertures, (d) focused at bottom of apertures. Changing the distance between the sample and the microscope objective were used to show variation of the brightness different apertures.

the sample, which revealed varying of brightness of apertures for varying nanohole configurations. The bright area in the CCD image is a scratch in the gold layer that serves as a fiducial marking for finding the corresponding location in the trapping setup.

Figure D.13 shows several of the structures analyzed in the main text. The structure of each aperture was confirmed using the SEM images.

Figure D.14 shows the transmission simulation for varying the polarization angle of the incident beam for a triangular structure, obtained by finite-difference time-domain (FDTD) method (Ansys Lumerical 2020 R2.3) at 973 nm wavelength, confirming that the transmission shows negligible polarization dependence. A triangular aperture with 70 nm gap size and 280 nm aperture diameter in a 70 nm gold film was simulated with the same dimensions as Triangular 1 in the Figure 4 of the main text. The refractive index of gold was chosen as Au (Gold) – Palik [244]. A layer of water (H_2O (Water) – Palik) with 200 nm thickness was placed above the gold layer. Also the triangular aperture material was selected as water similar to experiments. A glass

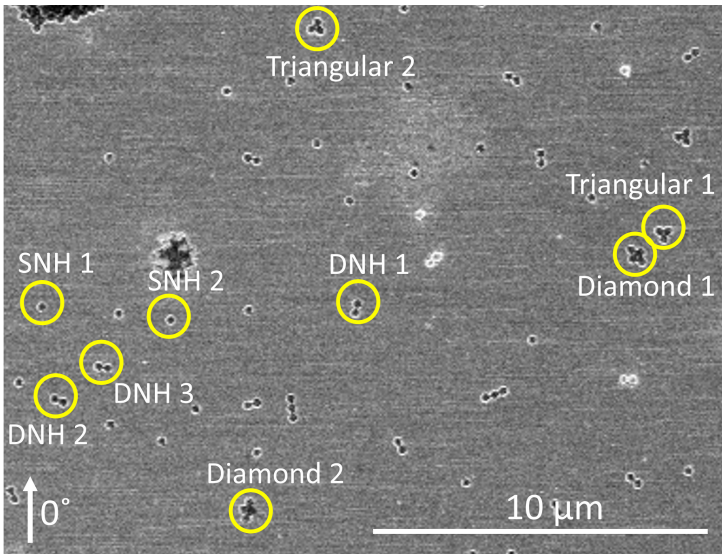

Figure D.13: SEM image of the sample used in the measurements shown in Figures 3-6 of the main text. Labels are the same as used on the main text.

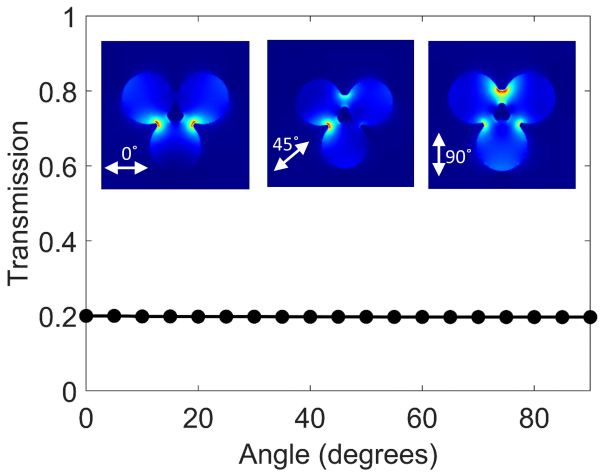

Figure D.14: The transmission for varying the polarization angle of the incident beam for a triangular structure, obtained by FDTD simulations. The triangular structure showed negligible polarization dependence. Insets show the electric field distribution of the triangular structure for 0, 45, and 90 directions of the incident electric field. Triangle nanostructure was simulated with the same dimensions as Triangular 1 in the Figure D.4 of the main text.

(SiO_2 (Glass) – Palik) substrate was created with the thickness of 2 μm and lateral dimensions of 2.8 μm $\times$ 2.8 μm, the same lateral dimensions as the gold and glass layers. For the FDTD simulations, we used the following parameters: the simulation

volume had dimensions of 1.3 μm $\times$ 1.3 μm $\times$ 170 nm in the x, y and z directions. A uniform mesh of 5 nm was used. Perfectly matched layers were used on all boundaries. A total-field scattered-field (TFSF) source with 800 to 1200 nm wavelength range was used. The TFSF region dimensions in x, y and z directions were 800 nm $\times$ 800 nm $\times$ 110 nm and the source was placed 30 nm above the gold film. To obtain the polarization dependence of the transmission, a frequency-domain field and power monitor was placed 10 nm above the gold film. Transmission at 973 nm was recorded for varying of the polarization angles of the source from 0 to 90. Insets show the electric field distribution of the triangular structure for 0, 45, and 90 polarization angles of source, measured with a frequency-domain field and power monitor which was placed in the middle of the gold film.

Trapping is typically performed on DNH structures, but other structures are capable of trapping. Figure D.15 shows a trapping event of a 20 nm polystyrene sphere using a triangular-shaped aperture.

Figure D.16 shows close-up SEM images of DNHs created using the colloidal lithography method on glass and plastic substrates.

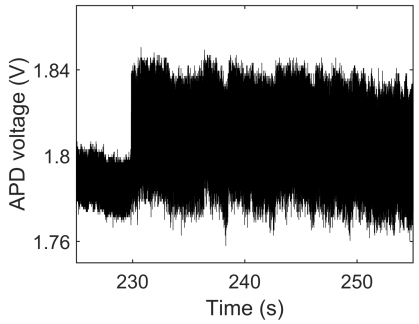

Figure D.15: Trapping event of a 20 nm polystyrene with the Triangular 1 (the SEM is shown in Figure D.13 with the incident laser power of 10 mW.

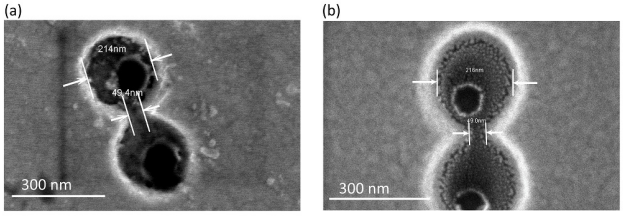

Figure D.16: An SEM image of a DNH in gold on a glass substrate, and (b) an SEM image of a DNH in gold on a plastic substrate. DNHs on both had aperture size of ∼215 nm and gap size of ∼50 nm, and they were fabricated by colloidal lithography method in a 70 nm gold film on top of a glass or plastic substrate, respectively.

As a proof of concept for the common application of protein trapping, the DNH structures found using the characterization approach presented in the main text were used to trap the PR65 protein. Figure D.17 shows a trapping event of a PR65 protein with a glass and with a plastic substrate.

Figure D.18 shows the transmitted laser signal for the data provided in the Figure D.8 of the main text. The APD voltage was measured for varying of the incident laser power while a polystyrene nanosphere was trapped with a DNH on the glass substrate (Figure D.18(a)) and a DNH on the plastic substrate (Figure D.18(b)).

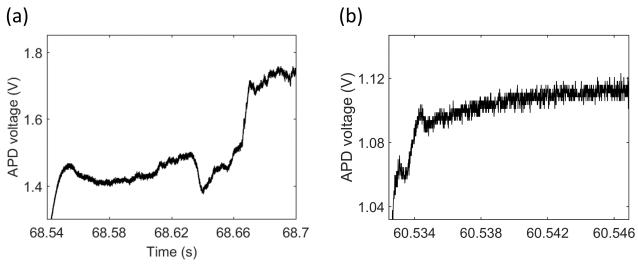

Figure D.17: Trapping a PR65 protein with glass and plastic substrates. (a) Trapping with a DNH on a glass substrate, and (b) trapping with a DNH on a plastic substrate.

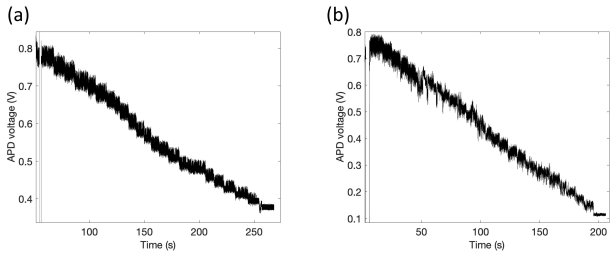

Figure D.18: The transmitted voltage measured in the APD for trapping events of polystyrene nanospheres with plasmonic DNHs on a glass and a plastic substrates for varying the incident laser power, while the polystyrene nanosphere was still trapped.

Appendix E

Scripts Written for : Large Plasmonic Resonance Shifts from Metal Loss in Slits

Matlab Script to Calculate the Propagation Constant

```
clc
    clear all
    eps0 = 8.854e-12;
    u0 = 4*pi*1e-7;
    c0 = 1 / sqrt(eps0 * u0);
    lambda = 600e-9;
    syms x
    epsm=[-2 -3 -4 -5 -10 -20 -30];
    for k=1:8
    for j=2:9
    w(j-1) = 0.05*j * lambda;
    k0 = 2*pi/lambda;
    Fun = tanh(sqrt(x-k0^2)*w(j-1)/2)*epsm(k)*sqrt(x-k0^2)+sqrt(x-epsm(k)*
k0^2);
    xx=solve(Fun);
    neff(j-1) = sqrt(xx)/k0;
```

```
    end
    plot(w/lambda,neff)
    end
```

Matlab Script to Calculate Reflection Coefficient

```
clc
    clear all
    eps0 = 8.854e-12;
    u0 = 4*pi*1e-7;
    c0 = 1 / sqrt(eps0 * u0);
    epsm = -5;
    lambda = 1550e-9;
    syms kx
    w = 200e-9;
    k0 = 2*pi/lambda;
    kz = 2.5 * k0;
    A = kx;
    B = sqrt(kz^2 - epsm * k0^2);
    I = 1./2./(1i*kx-A).*exp((1i*kx-A)*w/2)-1/2/(1i*kx-A).*exp(-1*(1i*kx-A)*w/2)+1/2/(1i*kx+
1/2/(1i*kx+A).*exp(-1*(1i*kx+A)*w/2);
    M = cosh(A*w/2)/epsm./(B-1i*kx).*exp(1i*kx*w/2);
    N = cosh(A*w/2)/epsm./(B+1i*kx).*exp(-1i*kx*w/2);
    Fun = matlabFunction(k0./sqrt(k0^2 - kx.^2). * (I + M + N).^2);
    G = matlabFunction(I);
    Int = integral(Fun,-inf,inf);
    P=2*pi*(w/2+1/2/A*sinh(A*w)+1/B/epsm^2 * cosh(A * w/2)^2);
    R=Int/P;
    r=1-R/1+R
```

Lumerical Script to calculate the Reflection Phase

```
switchtolayout;
    ?d=[20]*1e-9;
```

```
?d=[50,200]*1e-9;
M=150*3;  lambda number
setglobalmonitor("frequency points",M);
wavelengthstart=0.3e-6;
wavelengthstop=1.3e-6;
LMatrix=[500e-9,600e-9,700e-9,800e-9, 900e-9];
LMatrix=[70e-9,100e-9,150e-9,200e-9,250e-9,300e-9];
LMatrix=[100e-9,150e-9,200e-9,250e-9];
LMatrix=[1200e-9];
N=length(LMatrix);
TransmittancePowerMatrix=matrix(M,N);
mode source
select("ModeSource");
set("enabled",0);
for(k=1:N) ?"k = " + num2str(k);
L=LMatrix(k);
switchtolayout;
select("Au_up");
set("y min",d/2);
set("y max",2e-6);
set("x min",-L);
set("x max",0);
select("Au_down");
set("y max",-d/2);
set("y min",-2e-6);
set("x min",-L);
set("x max",0);
select("mesh");
set("y",0);
set("y span",2.5*d);
set("x min",-(L+L));
set("x max",L);
set("override x mesh",1);
set("dx",2e-9);
set("override y mesh",1);
```

```
set("dy",5e-9);
select("source");
set("y",0);
set("y span",2*d);
set("injection axis","x");
set("x",-1*(L+30e-9));
select("monitor1");
set("y",0);
set("y span",4*wavelengthstart);
set("x",10e-9);
select("monitor2");
set("y",0);
set("y span",4*wavelengthstart);
set("x",-1*10e-9);
select("FDTD");
set("y",0);
set("y span",5*wavelengthstart);
set("x min",-1*(3*wavelengthstart+L));
select("source");
set("wavelength start",wavelengthstart);
set("wavelength stop",wavelengthstop);
run;
select("monitor1");
TransmittancePowerMatrix(:,k)=transmission("monitor1");
select("monitor1");
freqMatrix=getdata("monitor1","f");
wavelengthMatrix=c/freqMatrix;
TransmissionMatrix=sqrt(abs(TransmittancePowerMatrix));
plot(wavelengthMatrix/1e-6,(TransmissionMatrix),"wavelength (um)","Transmission");
leg=cell(length(LMatrix));
for (s=1:length(LMatrix)) legs="L="+num2str(LMatrix(s)/1e-9)+"(nm)";
?s;  legend(leg);
maxMatrixIndex=zeros(length(LMatrix));
maxMatrix=zeros(length(LMatrix));
for (s=1:length(LMatrix)) maxMatrixIndex(s)=findpeaks(TransmissionMatrix(:,s));
```

```
maxMatrix(s)=max(TransmissionMatrix(:,s));
maxFreqMatrix=freqMatrix(maxMatrixIndex);
maxFreqMatrixSort=sort(maxFreqMatrix);
indexOfSortedFereq = sortmap(maxFreqMatrix);
LmatrixSorted=LMatrix(indexOfSortedFereq);
neff
switchtolayout;
select("ModeSource");
set("enabled",1);
set("y",0);
set("y span",6*d);
set("injection axis","x");
set("x",-20e-9);
neffMatrix=zeros(1,length(LMatrix));
for (k=1:length(maxFreqMatrixSort)) set("frequency start",maxFreqMatrixSort(k));
set("frequency stop",maxFreqMatrixSort(k));
updatesourcemode(1);
mh=getresult("ModeSource","neff");
neffMatrix(1,k)=mh.neff;
set("enabled",0);
trialPhiNum=20;
phiMatrix=zeros(trialPhiNum,length(maxFreqMatrixSort));
for (m=1:trialPhiNum) phiMatrix(m,:)=(m-1)*pi-(2*pi*maxFreqMatrixSort/c)*LmatrixSorted;
phiMatrix(m,:)=(m-1)*pi-(2*pi*maxFreqMatrixSort/c)*LmatrixSorted*real(neffMatrix);

phiFinal=zeros(1,length(LMatrix));
for (k=1:length(LMatrix)) phiFinal(1,k)=min((phiMatrix(:,k))); phiFinal(1,k)=min(abs(phiMat
phiFinal(1,k)=max(phiMatrix(find(phiMatrix(:,k)¡0),k));
plot((c/maxFreqMatrixSort)/1e-6,phiFinal,"wavelength (um)","Phi","phi minus");
phiFinalNew=phiFinal+pi;
plot((c/maxFreqMatrixSort)/1e-6,phiFinalNew,"wavelength (um)","Phi","Phi plus");
plot nspp plot((c/maxFreqMatrixSort)/1e-6,real(neffMatrix),"wavelength (um)","neff");
plot(LMatrix,(c/maxFreqMatrixSort)/1e-6,"L (um)","lambda");
plot(LmatrixSorted,1/real(neffMatrix),"L (um)","neff1");
```